3D super-resolution cardiac parametric mapping

vorgelegt von
M. Sc.
Simone Hufnagel
ORCID: 0000-0003-3942-5113

an der Fakultät V - Verkehrs- und Maschinensysteme
der Technischen Universität Berlin
zur Erlangung des akademischen Grades

Doktorin der Ingenieurwissenschaften
-Dr.-Ing.-

genehmigte Dissertation

Promotionsausschuss:
Vorsitzender: Prof. Dr.-Ing. Marc Kraft
Gutachter: Prof. Dr. rer. nat. Tobias Schäffter
Gutachterin: Prof. Dr. Claudia Prieto Vasquez

Tag der wissenschaftlichen Aussprache: 15. Dezember 2023

Berlin 2024

Zusammenfassung

Die kardiovaskuläre Magnetresonanztomografie (MRT) hat sich zur Standardmethode für die Beurteilung von Herzfunktion, -volumen und -masse sowie für die Charakterisierung der Zusammensetzung des Herzmuskelgewebes entwickelt. Im Vergleich zu anderen bildgebenden Verfahren ist die kardiovaskuläre MRT einzigartig in ihrer Fähigkeit, die Zusammensetzung des Herzmuskelgewebes ohne ionisierende Strahlung zu charakterisieren.
Aktuelle kardiovaskuläre MRT-Techniken liefern in der Regel qualitative T_1-gewichtete Bilder, die in willkürlichen, von Studie zu Studie variierenden Einheiten dargestellt werden und für die es keine Referenzwerte gibt. Mithilfe von T_1-Mapping kann die quantitative T_1-Relaxationszeit jedes Voxels innerhalb des Sichtfeldes bestimmt werden, indem mehrere T_1-gewichtete Bilder aufgenommen werden. Auf diese Weise lassen sich veränderte Gewebemerkmale erkennen, die mit Krankheiten wie Ödemen, Fibrosen und infiltrativen Erkrankungen einhergehen. T_1-Mapping hat das Potenzial, sowohl fokale als auch diffuse Erkrankungen zu erkennen und frühe asymptomatische Gewebeumwandlungen zu beurteilen. Jedoch schränken die lange Untersuchungszeit, die geringe räumliche Auflösung entlang der Schichtcodierrichtung und die begrenzte räumliche Abdeckung die klinische Anwendung ein.
In dieser Arbeit wurden neue Methoden entwickelt, um diese Beschränkungen zu überwinden und eine hochaufgelöste, dreidimensionale kardiovaskuläre T_1-Karte des ganzen Herzens in einer kurzen Aufnahmezeit von drei Minuten zu rekonstruieren. Dazu wurden zweidimensionale Schichten mit einer schnellen, kontinuierlichen Golden-radial-Winkel-Sequenz mit einer hohen Auflösung in der Ebene, aber einer geringen Auflösung entlang der Schichtcodierrichtung aufgenommen. Anschließend wurden dreidimensionale hochaufgelöste Schichten aus den niedrig aufgelösten Daten mit einem Super-Resolution-Rekonstruktionsverfahren (SRR) rekonstruiert. Eine radiale SRR-Akquisitionsgeometrie der niedrig aufgelösten Datensätze ermöglichte eine Abdeckung des gesamten Herzens. Kleine Strukturen wie Teile der Vorhofwände oder der rechten Ventrikelwand konnten mithilfe einer k-raum basierten SRR aufgelöst werden. Die vorgestellten Techniken wurden in Simulations- und Phantomexperimenten evaluiert und die erfolgreiche Anwendung an gesunden Probanden gezeigt.
Die in dieser Arbeit vorgeschlagene Methode ist vielversprechend, um hochauflösende T_1 Karten von Herzgewebe in kurzer Aufnahmezeit zu erhalten. Dieser Ansatz ist vielseitig und könnte in zukünftigen Studien zur schnellen Erfassung mehrerer quantitativer Parameter-Karten gleichzeitig, wie beispielsweise der T_1- und T_2-Kartierung des gesamten Herzens verwendet werden.

Abstract

Cardiovascular magnetic resonance imaging (MRI) has become the standard method for assessing cardiac function, volumes, and mass and characterizing myocardial tissue composition. Compared to other imaging techniques, cardiac MRI is unique in its ability to accurately characterize the composition of myocardial tissue without any ionizing radiation.

Current cardiac MRI techniques typically obtain qualitative images, which commonly only allow for the detection of focal pathologies and are difficult to compare between different scans or institutions. To address this issue, T_1 mapping can be used, which yields quantitative T_1 relaxation times of each voxel within the field of view. This allows for the identification of altered tissue characteristics associated with oedema, fibrosis, and infiltrative diseases. T_1 mapping has the potential to detect both focal and diffuse diseases and to assess early asymptomatic tissue remodelling. However, the lengthy examination time, low spatial through-plane resolution, and limited spatial coverage limit its clinical application.

In this thesis, new methods were developed to address these limitations and obtain a whole-heart high-resolution (HR) three-dimensional cardiac T_1 map in a short acquisition time of three minutes. For that, two-dimensional slices were acquired using a fast, continuous Golden-radial angle sequence with a high in-plane but low through-plane resolution. A k-space-based super-resolution reconstruction (SRR) approach was then used to reconstruct three-dimensional HR slices from the acquired low-resolution (LR) data. A radial SRR acquisition geometry of the LR datasets allowed a whole-heart coverage. Small structures, such as the atrial or right ventricular walls, could be visualized. The presented techniques were evaluated in simulation and phantom experiments, and feasibility was shown in healthy volunteers.

The imaging approaches proposed in this thesis show promise for obtaining HR parameter maps of cardiac tissues in a short acquisition time. This approach is versatile and could be used to quickly acquire multiple quantitative parameter maps, such as simultaneous T_1 and T_2 mapping of the entire heart in future studies.

Acknowledgements

I sincerely thank my supervisors, Dr. Christoph Kolbitsch, Prof. Tobias Schäffter, and Prof. Jeanette Schulz-Menger, for their continuous support.
I also want to thank my valued colleagues for their professional and personal contributions, greatly enriching my working time.
Finally, I would like to take this opportunity to express my gratitude to my family and friends for their constant support.

Table of Contents

List of Figures

List of Tables

Abbreviations

M_0 initial magnetization 12

Δz slice thickness 26

α read out flip angle 14

2CH two chamber orientation 8

2D two-dimensional 16

3D three-dimensional 3

4CH four chamber orientation xiv

BH breath hold xiii

bSSFP balanced steady-state free precession 11

CT computed tomography 1

ECG electrocardiogram xiii

ECV extracellular volume 10

FFT fast Fourier transform 15

FOV field of view 3

FWHM full width at half maximum 37

HR high resolution v

IR inversion recovery 10

LR low resolution v

MOLLI modified Look-Locker inversion recovery xiii

MRI magnetic resonance imaging v

PE phase-encoding 17

RF radio frequency 1

RMSE root-mean-squared error 37

ROI region of interest 24

SAX short axis orientation xiii

SD standard deviation 26

SE slice-encoding 18

SNR signal-to-noise ratio ix

SR saturation recovery 10

SRR super-resolution reconstruction iii

TE echo time 25

TI inversion time 25

TR repetition time 25

TSE turbo-spin-echo dark blood 83

1

Introduction

Cardiovascular diseases are the major cause of death worldwide and also cause significant healthcare expenses [1, 2]. Advancements in noninvasive methods to diagnose cardiac and vascular structure and function have provided valuable insights into the early stages of cardiovascular diseases. This knowledge has helped to understand disease prevalence and development, and in some cases, has enabled pre-symptomatic screening, early diagnosis, and potentially life-saving interventions [2].

Cardiovascular imaging plays an important role in diagnosing and treating cardiovascular diseases, thereby contributing to an increase in overall health, reduced morbidity, and enhanced quality of life for the population [3]. Cardiovascular imaging allows physicians to observe the structure and function of the heart, enabling them to identify a range of different heart abnormalities, such as reduced blood circulation, regulation of volumetric output of blood, valve function, plaque buildup in arteries, and more.

Common methods for cardiovascular imaging include X-ray, computed tomography (CT), magnetic resonance imaging (MRI), ultrasound-based echocardiogram, PET/SPECT, and catheterisation [3]. Cardiovascular MRI has emerged as the gold standard for evaluating cardiac function, volumes, and mass. Among the imaging modalities used in cardiovascular diseases, its ability to characterise myocardial tissue composition is unique [4].

Cardiovascular MRI is increasingly used to evaluate myocardial structure and function noninvasively without exposing the patient to ionising radiation [5]. Cardiovascular MRI provides excellent contrast of soft tissues, enabling the assessment of myocardial function and the characterisation of myocardial structure [6, 7].

Qualitative images such as T_1 weighted images are typically obtained in cardiovascular MRI. These rely on the relative difference in the relaxation properties between different heart tissues [7]. The observed image contrast is determined by various scan-specific parameters, such as sequence parameters, RF coil proximity, receiver chain efficiency, or magnetic field inhomogeneities [8]. These factors vary across different studies, lacking reference values. However, the quantitative relaxation time T_1 is independent of these hardware and sequence parameters. Hence, T_1 mapping can be used to obtain an objective indicator of tissue condition, making it valuable in assessing tissue disorders. Healthy myocardium has a specific T_1 relaxation

time, but this can be altered in the presence of diseases such as oedema [9], fibrosis [10], or infiltrative diseases [11]. T_1 mapping can be used to detect both focal and diffuse diseases, as well as assess early, asymptomatic tissue remodelling that may not be evident with other noninvasive techniques [5].
Although there is a significant potential for cardiovascular T_1 mapping, its utilisation in clinical practice is still limited. The primary obstacles in implementing T_1 mapping include the lengthy duration of the examination, low spatial through-plane resolution, and limited spatial coverage. These three challenges need to be addressed for the successful integration of T_1 mapping into routine clinical procedures:

1. Cardiovascular T_1 mapping is time-consuming for medical staff and patients. Additionally, the long acquisition time can lead to motion artefacts, resulting in a decrease in image quality [12]. This often necessitates additional examinations and further reduces patient comfort and the economic efficiency of the procedure [13].

2. Commonly, T_1 mapping suffers from low through-plane resolution and is mainly used in the left ventricle. While this allows midventricular imaging, the imaging of the apex is challenging due to partial volume effects [14, 15]. Next to that, low-resolution (LR) T_1 mapping offers only limited value for thin-walled structures [14] such as the atria and the right ventricle [15, 16].

3. Pathological changes in the myocardium can be very localised, depending on the specific type of cardiovascular disease. When dealing with cardiovascular diseases involving focal heterogeneity, it is necessary to analyse the regional characteristics of the myocardial tissue to gain insight into the underlying causes of the pathology. The detection of focal diseases might be overseen by covering only parts of the myocardium with a few slices. So there is a clinical need for whole heart T_1 mapping techniques that can provide a comprehensive assessment of the complex regional distribution patterns of the disease [15].

Therefore, fast, high-resolution (HR) and whole-heart T_1 mapping techniques need to be developed to provide accurate and precise T_1 quantification. So far, whole-heart T_1 mapping with high isotropic resolution (below or equals 1.5 mm) is only possible with long acquisition times (more than nine minutes) [17–23].

1.1 Scope of the thesis

The work presented in this thesis aims to develop an approach for fast HR whole-heart cardiovascular T_1 mapping by using a motion-corrected k-space-based super-resolution reconstruction (SRR) approach. The individual components dedicated and required to acquire a HR whole-heart cardiovascular T_1 map in a short acquisition time are the following:

1. A SRR approach is investigated, combining multiple LR multi-slice stacks with reliable T_1 values to achieve a HR T_1 map and allowing an efficient use of scan time. The aim is to provide a HR volume with reproducible T_1 estimates and a short acquisition time.

2. Good visualisation of small structures such as the right ventricular wall in a 3D HR T_1 map is aimed at using a motion-corrected k-space-based SRR approach. This would allow the reconstruction of the HR T_1 map directly from the acquired k-space data.

3. Whole heart coverage needs to be achieved with appropriate scan plane orientations. For that, radially overlapping long-axis stacks are investigated. This could improve the overall image quality and the visualisation of small structures while providing precise T_1 values.

1.2 Outline

This thesis is divided into eight chapters:

Chapter 2: Basics of the cardiovascular anatomy are summarised, and common imaging methods are described. The principle of T_1 relaxation and techniques to quantify T_1 for cardiovascular applications are presented. Next to that, existing research on SRR is summarised.

Chapter 3: T_1 mapping of a single cardiovascular multi-slice stack is proposed. Due to limited breath hold (BH) length and overall acquisition time, the acquisition time for one single LR stack is minimised. Cardiac motion correction and a model-based T_1 reconstruction are used for that. Sequence parameters such as the inversion pulse and the gap between the slices are investigated to provide accurate T_1 estimates. The influence of the slice thickness and acquisition time for a single LR slice on the signal-to-noise ratio (SNR) is evaluated experimentally for quantitative T_1 maps.

Chapter 4: A model-based SRR optimisation scheme adapted for quantitative cardiovascular imaging is proposed and tested with simulated data. For that, differently shifted LR stacks in short-axis orientation (SAX) are acquired. The performance of the proposed SRR with respect to resolving small structures is evaluated. The influence of different parts of the acquisition model, such as motion and slice profile accuracy, are investigated with respect to the accuracy of the T_1 values provided by the SRR.

Chapter 5: The model-based SRR optimization scheme is tested *in vivo* and in phantom measurements. A motion correction approach is proposed to align LR stacks obtained in different BH positions. The performance of the resulting approach is evaluated in four healthy volunteers.

Chapter 6: The field of view (FOV) is evaluated for whole-heart applications by adapting the SRR geometry. Instead of differently shifted LR stacks, the LR stacks are rotated to one another, and cardiovascular long-axis images are acquired instead of SAX images. For that, the sequence parameters are adapted to provide accurate T_1 estimates for the long-axis images. The rotated SRR geometry is optimised for cardiovascular imaging to obtain accurate and precise cardiovascular T_1 estimates and whole-heart coverage. The influence of the adapted

SRR geometry with respect to resolving small structures is evaluated.

Chapter 7: A k-space-based SRR approach is proposed and compared to an image-space-based approach. By that, undersampling artefacts in the reconstructed LR dynamics might no longer propagate into the SRR result. Its effect on the visualisation of small structures is investigated. The resulting approach is tested in ten healthy volunteers. The performance of the proposed approach with respect to providing precise T_1 values of the whole heart with a high spatial resolution in a low acquisition time is evaluated.

Chapter 8: Main findings are summarised, and future research improvements are discussed.

2 Cardiac MRI

2.1 Cardiac anatomy

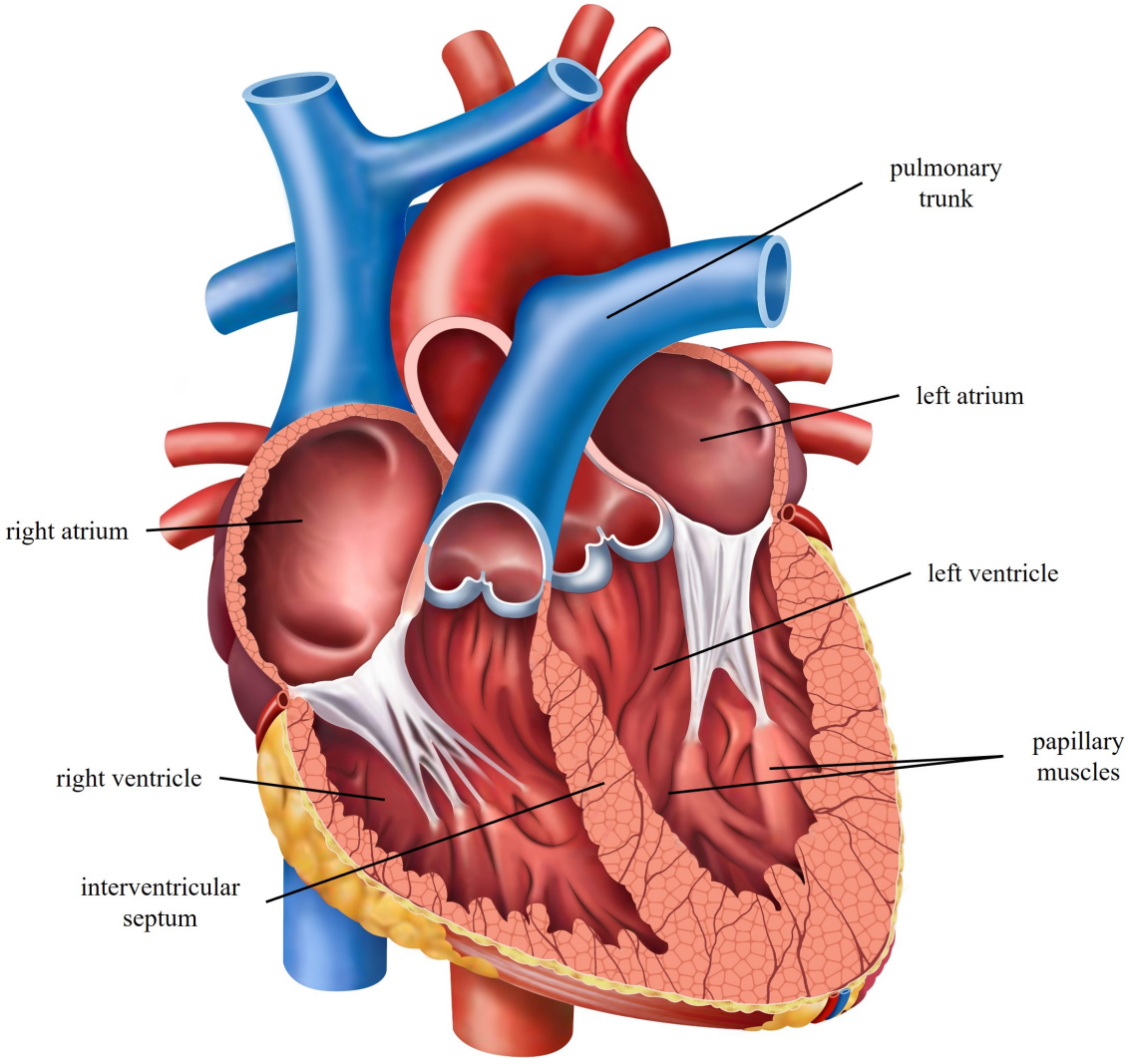

Figure 2.1: Frontal section of the heart (source: Shutterstock/ilusmedical)

The myocardium consists of four chambers: the right and left atrium and the right and left ventricle. The atria are divided by the interatrial septum, and the ventricles are separated by the interventricular septum (see Figure 2.1).
While the atria gather the blood, the ventricles press it into the body. The right atrium opens into the right ventricle, pumping blood into the pulmonary trunk. The oxygen-rich blood returns from the lungs and is received by the left atrium. The left atrium opens into the left ventricle, pumping the blood into the systemic circuit.
At the beginning of the cardiac cycle, both the atria and ventricles are relaxed (atrial and ventricular diastole), as shown in Figure 2.2, allowing blood to flow into the atria. During atrial systole, the muscles in the atria contract, forcing blood into the ventricles. Atrial systole lasts for around 100 ms and concludes before ventricular systole, as the atrial muscles return to their relaxed state. Following atrial systole, ventricular systole begins. This is characterised by the contraction of the ventricular muscles, pumping blood out of the heart. The entire ventricular systole phase lasts for approximately 270 ms. After contraction, the ventricles relax for about 430 ms (ventricular diastole) before the contraction in the next cardiac cycle [24].

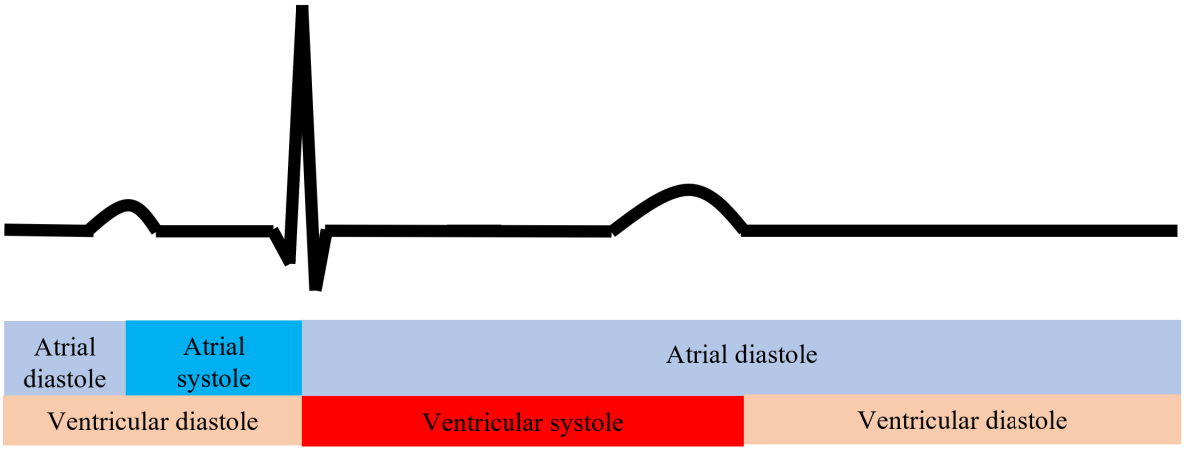

Figure 2.2: Relationship between the cardiac cycle and the electrocardiogram (based on [24])

The left and right ventricles contain two and three papillary muscles, respectively [25]. Papillary muscles are elongated muscles originating from the inner wall of the ventricles and attached to the edges of the atrioventricular valves. During contraction of the ventricles, these muscles prevent the atrioventricular valve leaflets from being inverted or leaking since the pressure in the ventricular cavity is rising during systole [26].
While the left ventricular wall is relatively thick with about 7 mm [27], the thickness of the right ventricle is below 5 mm [28]. The atrial walls are even thinner, with a wall thickness of approximately 2 mm in the left atria and approximately 3 mm in the right atria [29].

While the assessment of the left ventricular chamber is performed routinely in clinical cardiovascular MRI, imaging of the right ventricle or the atrial walls experiences challenges since the spatial resolution of the MRI scans often limits their visualisation, as in late gadolinium enhancement imaging [30] or parametric mapping techniques [15].
However, function, size and morphology of the right ventricle strongly influence morbidity and mortality in various cardiac diseases, for example, congenital heart disease, myocardial

infarction [31], or pulmonary hypertension [32]. Right ventricular fibrosis may be important in diseases such as arrhythmogenic right ventricular dysplasia [33]. However, characterising the right ventricle with cardiovascular MRI is challenging and often done using an invasive endomyocardial biopsy [32].
The use of MRI has recently become a promising tool for understanding the changes in the structure of the atrial wall [34]. However, due to the limited spatial resolution of MRI scans, there is a risk that the classification of the left atrial wall will be impaired due to partial volume effects. This effect occurs if a voxel covers different tissue types, and only an average of the tissue signal can be visualised. This is especially problematic when the atrial wall is in the order of the voxel size due to partial volume effects [35].

2.2 Cardiac acquisition geometries

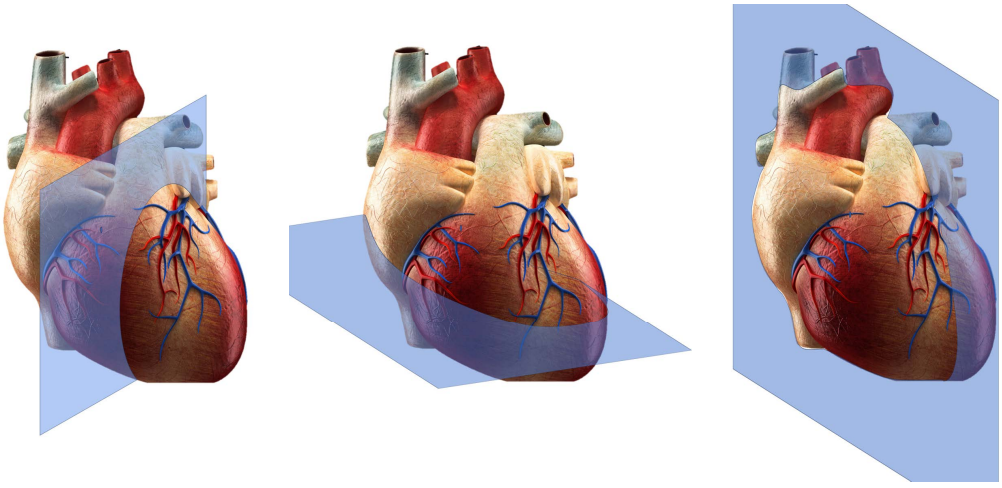

(a) SAX (b) 4CH (c) 2CH

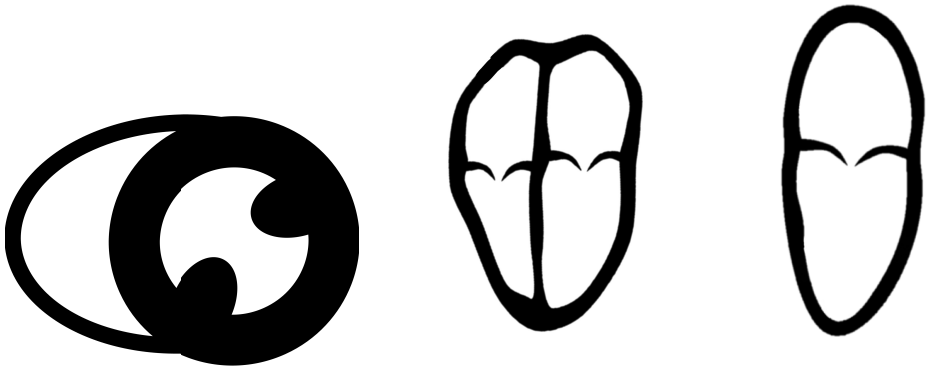

(d) SAX (e) 4CH (f) 2CH

Figure 2.3: Cardiac acquisition geometries. The upper row shows the positioning of the imaging plane in the heart anatomy while the second row shows a pictogram of the respective resulting slice (images based on: Shutterstock/decade3d - anatomy online (a-c) and Shutterstock/noonin (e-f))

The myocardium is mainly analysed by acquiring a stack of parallel SAX slices [36]. For global diseases, optionally, a single long-axis map is acquired, while for a patchy disease, the acquisition of at least one long-axis map is mandatory [15]. A long-axis map is usually

acquired in a four-chamber (4CH) or a two-chamber orientation (2CH). How these different orientations are placed in the heart is shown in Figure 2.3.

The segmentation of the left ventricle is easier in the SAX compared to the long-axis orientation due to its simpler shape [37]. Next to that, with the SAX, through-plane partial volume effects can be minimised [15].
However, the SAX is quite inefficient with respect to the heart coverage: Due to the geometry of the heart, a long-axis orientation covers more of the heart with its FOV compared to a SAX and therefore might be more time-efficient [38]. Next to that, due to the partial volume effect, SAX images of the apex only have limited value [15]. Long-axis views, however, provide well-defined basal and apical borders of the myocardium [39].

Another acquisition scheme consisting of radial long-axis views that are rotated around the central longitudinal axis of the left ventricle was proposed in [40] (see Figure 2.4). This allows for a rapid calculation of the left ventricular volume, as it is often challenging for volume quantification of the left ventricle to determine the most basal left ventricular SAX slice.

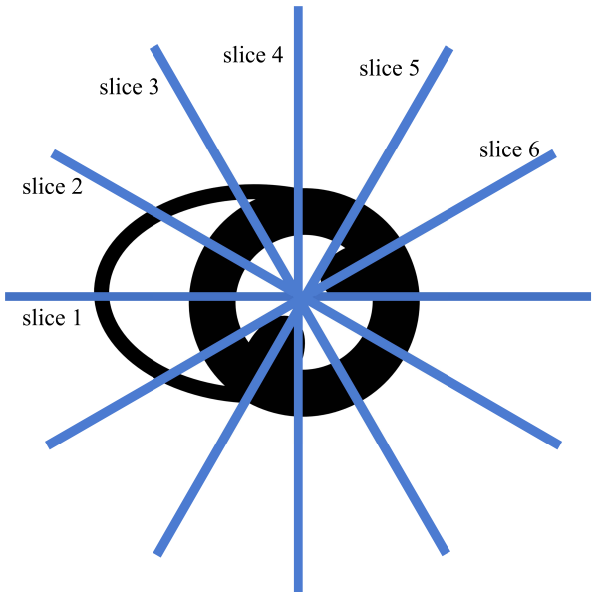

Figure 2.4: Rotated long-axis acquisition geometry as proposed in [40]

.

2.3 T_1 relaxation

MRI relies on the alignment of nuclear spins in an external magnetic field and their stimulation by radio frequency (RF) pulses. By measuring the reaction of the nuclear spins to this external stimulus, information about the underlying tissue can be obtained.
When the RF field is turned off, the spin system returns to its original equilibrium state. This process is known as T_1 or longitudinal relaxation. During this relaxation process, the nuclear spins exchange energy with the surrounding lattice. This process is also referred to as spin-lattice relaxation. The duration of this process varies based on, for example, the chemical properties of the molecules.

2.4 Cardiac T_1 mapping

Healthy myocardial tissue consists of three main parts: the intracellular, intravascular, and interstitial compartments. The largest component of the intracellular compartment is mainly composed of myocytes. The intravascular compartment contains the blood, while the interstitial compartment supports the myocytes and transmits mechanical forces. The interstitial compartment, together with the intravascular compartment, is known as extracellular volume (ECV). In various cardiovascular diseases, such as oedema or fibrosis, the ECV expands, primarily due to the enlargement of the interstitial component [5].
T_1 relaxation time is a characteristic tissue property and contributes to the image contrast between different soft tissues in MRI. Commonly, T_1 weighted images are obtained, whose image intensities depend on relaxation times as well as sequence and hardware parameters. In recent years, T_1 mapping has been translated into clinical application as an important quantitative approach to differentiate different cardiac tissue types [4, 6, 41–43]. T_1 mapping allows measuring the T_1 relaxation time in each tissue voxel.
The T_1 relaxation time of the myocardium is influenced by alterations in the relative sizes of the intracellular volume and ECV. In the case of oedema or fibrotic conditions, the extracellular space, where water is less restricted in motion, expands, leading to higher native T_1 values. Infiltrative diseases such as Anderson–Fabry and iron overload cause the accumulation of short T_1 lipids and iron in the extracellular space, resulting in lower native T_1 values [5].

Several sequences were proposed to measure the T_1 value based on inversion or saturation pulses. After applying an inversion or saturation pulse, spins in a MRI system are flipped by 180° or 90° respectively and then gradually return to their equilibrium state. To calculate the T_1 relaxation time in each voxel of an image, conventional T_1 mapping techniques acquire multiple images at different times after the inversion or saturation pulse, called inversion recovery (IR) times or saturation recovery (SR) times respectively, and calculate the underlying relaxation time by fitting a signal model to the obtained data.
In clinical routine, mostly IR (modified Look-Locker inversion recovery (MOLLI) [44], ShMOLLI [45]) or SR (SASHA [46]) preparation pulses or a combination of the two (SAPPHIRE [47]) are used [15].

(a) sequence diagram. "INV" describes the application of an inversion pulse, and "IMG" describes the time point of image acquisition

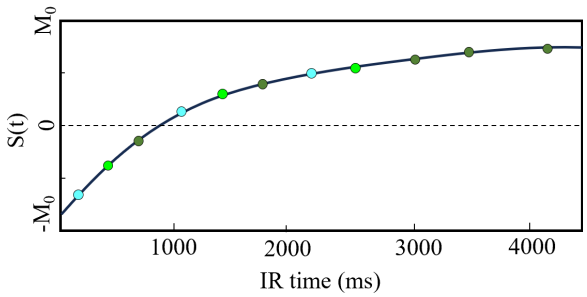

(b) magnetisation curve of the measured signal intensity $S(t)$ over the IR time

Figure 2.5: Cardiac T_1 mapping strategy: MOLLI

The MOLLI sequence was the first technique developed for mapping T_1 values in the heart. As shown in Figure 2.5, it involves acquiring several single-shot balanced steady-state free precession (bSSFP) [48] images after an inversion pulse during end diastole in consecutive cardiac cycles. The timing between these images is based on multiples of the R-R interval. Multiple sets of single-shot bSSFP images, known as Look-Locker sets, are acquired with their own inversion pulses to sample the relaxation curve at different time points. To allow for complete recovery of the longitudinal magnetisation before the next inversion pulse, periods without data acquisition are included between these sets of data.
The MOLLI sampling scheme is described using a specific nomenclature, such as, for example, 3(3)3(3)5 for the original publication, where the number without brackets indicates the number of images in one acquisition set. The number of cardiac cycles used for waiting time is indicated by the numbers in brackets. Each set samples different points of the relaxation curve, but all in the same cardiac motion state. A cardiac T_1 map resulting from a MOLLI acquisition is shown in Figure 2.6.

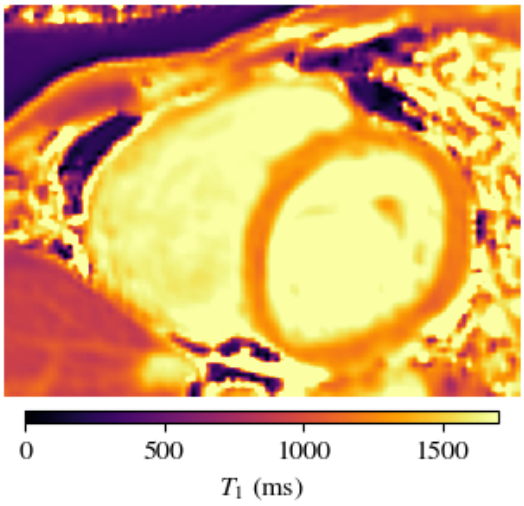

Figure 2.6: Cardiac T_1 map acquired using a MOLLI sequence

.

The read-outs lead the relaxation process to occur more rapidly and to stabilise at a steady state M_0^*, smaller than the equilibrium magnetisation M_0. This read-out effect leads to an apparent recovery time referred to as T_1^*, representing an apparent recovery time shorter than the actual longitudinal recovery time T_1 [14]. To account for this effect, a three-parameter exponential signal model was proposed, where the measured signal intensity values $S(t)$ at IR time point t can be used to estimate the parameters A, B, and T_1^*:

$$S(t) = A - B * exp(-t/T_1^*) \tag{2.1}$$

These parameters can then be used to approximate T_1 by calculating a correction factor, also known as the "Look-Locker" correction [49]:

$$T_1 = T_1^*(B/A - 1) \tag{2.2}$$

MOLLI is frequently used in cardiac T_1 mapping due to its high precision [15] and high SNR [5]. However, it is known that MOLLI tends to underestimate T_1 values [5] due to various factors such as T_2 relaxation time [50], magnetisation transfer [51], magnetic field heterogeneities [5], off-resonance effects [52], and the efficiency of inversion pulses [14]. Next to that, the traditional MOLLI technique involves holding the breath for 17 cardiac cycles, which can be difficult for some patients.

To address this challenge, a modified version called ShMOLLI was created. ShMOLLI requires only nine heartbeats and follows a 5(1)1(1)1 pattern. However, because there is only one heartbeat for recovery between sets, special data analysis is necessary: data from the last two sets are only used for very short T_1 times, such that a full recovery within only one heartbeat is possible.

The accuracy of the MOLLI technique can be strongly affected due to its high dependency on heart rate, as higher heart rates may prevent the longitudinal magnetisation from fully recovering to its initial state in the cardiac cycles used for waiting time. Modifications to the original MOLLI protocol have been proposed [52, 14] to provide accurate and precise T_1

estimates independent of the heart rate. For that, the waiting periods are based on seconds instead of R-R intervals. A 5(3s)5 acquisition scheme would indicate a three-second waiting period between the acquisition sets, while the recovery periods are approximated to the closest multiple of the R-R period to provide adequate electrocardiogram (ECG) triggering.

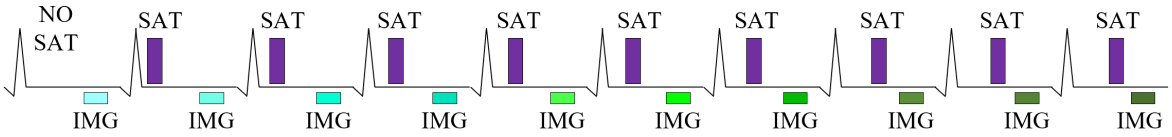

(a) sequence diagram. "SAT" describes the application of a saturation pulse, and "IMG" describes the time point of image acquisition

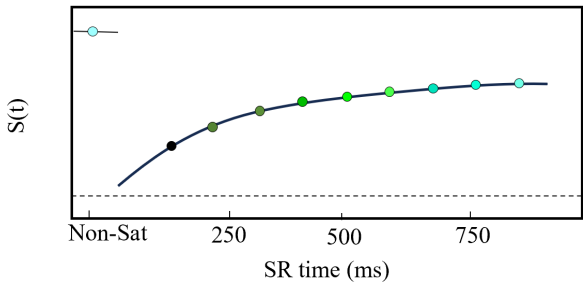

(b) magnetisation curve of the measured signal intensity $S(t)$ over the SR time

Figure 2.7: Cardiac T_1 mapping strategy: SASHA.

The SASHA sequence is composed of obtaining 10 ECG-gated single-shot bSSFP images in consecutive cardiac cycles, as shown in figure Figure 2.7. The first image does not involve any magnetisation preparation, while the subsequent nine images are collected after applying nine saturation pulses with varying SR times.
Different from MOLLI, saturation pulses have the advantage of making each measurement independent. When the recovery begins from a saturated state, any prior influence of inversion pulses is eliminated. Therefore, no recovery periods between consecutive measurements are needed [14]. The absence of a need for pause cycles in image acquisition results in greater scan efficiency compared to the MOLLI technique. Compared to MOLLI, SASHA is more accurate and less influenced by factors such as heart rate. However, compared to IR, SR has a reduced dynamic range since only signal intensities from 0 to M_0 are acquired compared to the range from $-M_0$ to M_0 as for IR. Consequently, SASHA generally has lower T_1 precision compared to IR sequences such as MOLLI [46].
An alternative technique called SAPPHIRE (SAturation Pulse Prepared Heart rate-independent Inversion REcovery) [47] has been suggested to merge the independent image properties of SR methods with the enhanced dynamic range of IR. For that, a saturation pulse is applied immediately after the ECG R-wave. This pulse nulls the entire magnetisation in the volume and removes the influence of the longitudinal magnetisation on signal recovery from previous R-R intervals. Subsequently, a conventional inversion pulse is applied after the saturation pulse. The T_1 values obtained using the SAPPHIRE method were comparable to those obtained using SASHA, with a level of precision between the MOLLI and the SASHA technique [5].

All these mapping sequences, however, are limited by acquiring data only in a small part of the cardiac cycle to minimise cardiac motion artefacts. This leads to long acquisition times: Assuming a heart frequency of 60 beats per minute, MOLLI takes 17 seconds, ShMOLLI 9 seconds, SASHA 10 seconds, and SAPPHIRE 9 seconds for a single slice. Next to that, all of the proposed sequences provide only low through-plane resolution, with a slice thickness of 8 mm for MOLLI, ShMOLLI and SASHA and even 10 mm for SAPPHIRE.

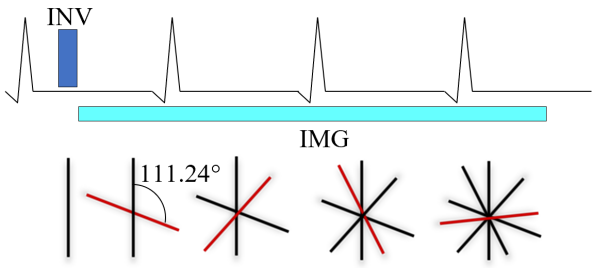

(a) Sequence diagram. "INV" describes the application of an inversion pulse, and "IMG" describes the time point of image acquisition

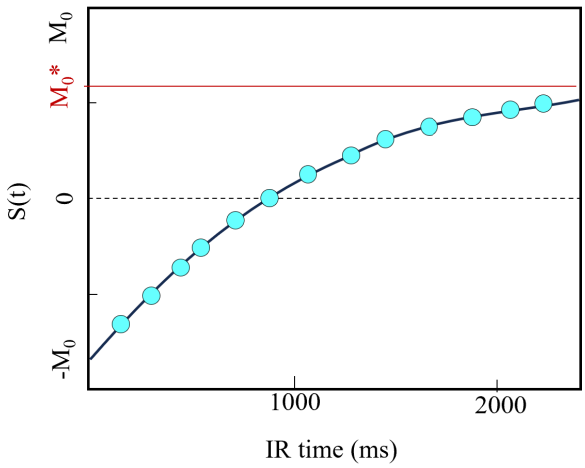

(b) magnetisation curve

Figure 2.8: Cardiac T_1 mapping strategy: Continuous Golden angle radial

Kerkering et al. [53–55] proposed a model-based T_1 mapping sequence (see Figure 2.8), which was able to provide a T_1 map within a 2.3 seconds scan with improved precision compared to cardiac-triggered data. For that, an inversion pulse was applied, and the T_1 relaxation curve was continuously sampled using a Golden angle radial trajectory. The application of read-out pulses leads to a constant loss of longitudinal magnetisation $M_z(t)$ at time point t after each application of the read-out pulses. Consequently, the signal intensities relax towards M_0^* instead of the equilibrium magnetisation M_0 and with an effective relaxation time of T_1^*, smaller than T_1. This effect was considered using a three-parameter (M_0, α, T_1) signal model to describe the signal behaviour of the continuous data acquisition after the inversion pulse, with α describing the flip angle of the read-out pulses. This was based on the evolution of $S(t)$ after the inversion, as described by the following equations [49]:

$$S(t) = M_0^* - (M_0 + M_0^*) * exp(-t/T_1^*) \tag{2.3}$$

$$M_0^* = M_0 \frac{T_1^*}{T_1} \tag{2.4}$$

$$T_1^* = [1/T_1 - (1/TR)ln(cos(\alpha))]^{-1} \tag{2.5}$$

TR thereby describes the repetition time.

For the reconstruction of the acquired k-space data, a model-based iterative scheme was introduced [54]. For that, a specific cardiac phase was chosen by retrospectively gating the k-space data based on the acquired ECG signal. After interpolation onto a cartesian grid, images were reconstructed using an inverse FFT. The magnitude images obtained at different inversion times were voxel-wise fitted to the magnitude of the model function described above. Based on the determined quantitative parameters, dynamics were calculated voxel-wise using the model function for each inversion time point. These images were then used to calculate k-space spokes. The model predictions were substituted with the acquired k-space data to ensure data consistency. The consistent k-spaces were then used as input for the next iteration. Next to that, cardiac motion correction was incorporated into the model-based reconstruction [53], allowing the use of all the acquired data during the cardiac cycle for the reconstruction, except for 30% of systole due to through-plane motion. The method is composed of three primary steps. The first step involves reconstructing dynamics with a high temporal resolution to capture cardiac motion. Additionally, a preliminary diastolic T_1 map is created using only images taken during a specified diastolic window to ensure consistency in the cardiac phase. In the second step, the preliminary diastolic T_1 map is used to calculate synthetic dynamics that exhibit the same contrast characteristics as the reconstructed dynamics but without any cardiac motion. Non-rigid motion estimation is then performed between the reconstructed and the synthetic dynamics to determine the extent of cardiac motion. Lastly, in the third and final step of the method, the calculated cardiac motion fields are applied in the motion-corrected model-based image reconstruction to obtain the final T_1 map. The determination of the systolic and diastolic times is based on the heart rate using a calculation method based on [56] in combination with a detection of the positions of the R-Peak in the ECG. An exemplary cardiac T_1 map resulting from the described technique acquisition is shown in Figure 2.9.
Nonetheless, the image resolution from the model-based T_1 mapping sequence was compromised by partial volume effects due to a slice thickness of 8 mm. This can impair the accurate detection of subtle fibrosis in the myocardium and restrict the ability to differentiate myocardial injury within the thin myocardial wall of young patients.

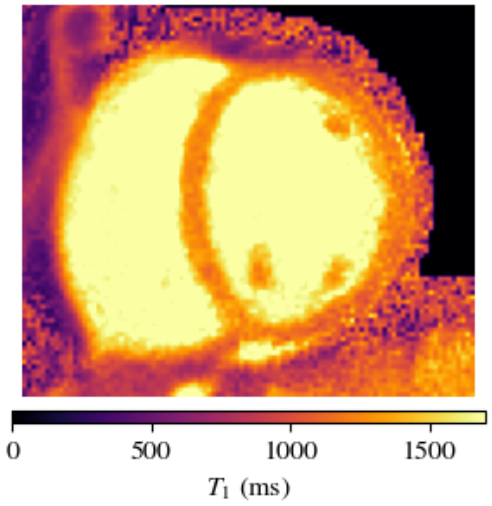

Figure 2.9: Cardiac T_1 map acquired using a continuous Golden angle radial acquisition scheme as presented in [53–55]

.

Instead of acquiring multiple 2D slices, a 3D volume can be acquired directly. However, the acquisition time for such a 3D volume is often too long for a single BH. An alternative is, therefore, to use a 3D navigated free-breathing sequence.
For motion navigated sequences, no BH is necessary, but the breathing state of the patient is tracked (using pneumatic bellows, navigator echoes, or novel methods such as the Pilot Tone [57]). This motion information can then be used either for a motion-corrected sequence, adapting the slice position accordingly, or for a gated sequence, acquiring data only in the desired motion state.
For example, [19] used a free-running 3D golden angle radial read-out interleaved with IR and T_2-preparation pulses for that. Together with translational respiratory motion and non-rigid cardiac motion correction, a 3D whole heart T_1 and T_2 map could be reconstructed with an isotropic resolution of 2 mm in approximately 3.3 min acquisition time. Similar results were achieved in [58, 17–23].
The acquisition time for 3D cardiac imaging, however, strongly depends on the performance of the navigator. Next to that, inaccuracies in the motion navigator might also deteriorate the overall 3D scan and introduce image artefacts.
So far, whole-heart T_1 mapping with high isotropic resolution is only possible for long acquisition times (isotropic resolution of 1.5 mm and reconstruction time of 9.5 minutes [22]). Others achieved a short acquisition time of up to 3.3 minutes, however, they achieved, at best, an isotropic resolution of 2 mm [58, 17–23].

2.5 Super-resolution reconstruction

The quality of MRI images is often restricted by various factors, including the movement of subjects during scanning and acquisition time constraints. SNR is another limiting factor due to the non-linear relationship between acquisition time and slice thickness, as described in the following equation [59, 60]:

$$SNR \propto \Delta z \sqrt{N} \tag{2.6}$$

with N denoting the number of phase-encoding (PE) lines or radial spokes for radial imaging and Δz the slice thickness .
Hence, the SNR can be increased by increasing the slice thickness or the number of PE lines. However, to double the SNR, for example, either the slice thickness can be doubled, or four times the number of PE lines need to be acquired, which is associated with a quadrupling of the acquisition time. This often leads to the acquisition of slices with a high slice thickness, so poor through-plane resolution.
Studies [59] have demonstrated the advantages of using SRR reconstruction methods over direct HR acquisition: They have shown that, for a given acquisition time, SRR reconstructed images have higher SNR compared to images obtained directly at the same high resolution.

SRR algorithms were first introduced in the early 1980s and were initially used in video processing to enhance the resolution of image sequences [61–63]. The basic concept behind SRR is to merge multiple LR observations of the same object to reconstruct a HR image. In video sequences, a HR frame can be generated by combining consecutive frames that capture the object with subpixel movement, such as a simple translation [64]. If the geometric transformation of the objects in the frames (translation, rotation, deformation) is known or accurately estimated with subpixel precision, it becomes possible to combine LR slices and obtain a HR volume. This ability to retrieve aliasing content gives SRR an advantage over standard interpolation techniques.

The MRI framework is particularly well suited for applying SRR techniques due to the control over the acquisition process. With the flexibility to choose any scanning plane orientation, acquiring multiple distinct LR observations of the subject is possible, even when no subject motion is involved.
In MRI imaging, there are two different types of SRR: in-plane SRR and through-plane SRR. [65, 66] have investigated improving the resolution in the in-plane direction. This was achieved by acquiring several scans with subpixel shifts in the FOV in the in-plane directions. SRR was then applied to generate a HR volume, which showed improved resolution in the in-plane dimension and a higher SNR. However, concerns were raised [67–69] about the theoretical basis of the in-plane resolution improvement: MRI data is acquired in the frequency domain called k-space. Subpixel FOV shifts in the in-plane dimension correspond to a linear phase modulation in the k-space, as long as the FOV and digital resolution remain constant across the scans. Under these conditions, the acquired k-space data is the same for all the scans, and no new frequency content is acquired. [67] suggested that similar results could be obtained by combining the same number of scans without introducing any shifts. [68] demonstrated that similar in-plane resolution improvement could be achieved using zero-padding interpolation. According to these researchers, the resolution improvement was only a result of noise reduction, leading to an improvement in SNR.
However, the anisotropy of the voxels in multislice MRI scans has prompted many authors to use SRR algorithms to improve the resolution in the through-plane direction. In 2D slice

stacks, each individual slice is Fourier encoded. However, in the direction perpendicular to the slices, there are no natural restrictions on the range of frequencies, allowing the possibility of recovering aliased frequencies. The extent of aliasing is influenced by the shape of the slice profile, which ideally should be a rectangular function for non-overlapping slices. However, the slice profile depends on the RF pulse and due to hardware limitations, a perfect rectangular shape is usually not achieved. Due to the aliasing that arises when the object is convolved with the slice profile, it becomes possible to perform slice profile recovery with shifts along or different orientations of the slice encoding (SE) direction [59].

SRR techniques can again be categorised into two main categories: multi-image SRR and single-image SRR.
In single-image SRR, only one LR image is given and based on that, a HR image is supposed to be calculated. For that, often example-based methods are used, using Deep learning to establish relationships between LR images and their HR counterparts. The learned relationship between them is then applied to a new LR image to generate its most likely HR version. This is, for example, used in [70], while the interested reader is forwarded to [71] for an overview of the Deep Learning methods that have been used for SRR.
In the multi-image approach, a HR volume is reconstructed by combining multiple LR images of the same scene. In this work, multi-image SRR is used.
The estimation of a HR volume from multiple LR slices using SRR can be described by the following inverse problem:

$$\gamma_s = \sum_{s=1}^{N_S} A_s * \Gamma + n \tag{2.7}$$

with the index s being the index of the LR multi-slice stack ($s = 1, ..., N_S$ and N_S being the number of stacks) and A describing the transformation of the HR volume Γ to the LR slice γ. The variable n denotes the noise in the LR slices, which can be assumed to be additive, white and Gaussian when the SNR > 3 [72].
Solving the inverse problem corresponds to recovering Γ given γ_s and A_s. The problem can be formulated as an ordinary least squares problem:

$$\min_{\Gamma} \sum_{s=1}^{N_S} ||\gamma_s - A_s * \Gamma||_2^2 \tag{2.8}$$

The acquisition model A is application-specific but generally decomposes into the geometric transform between the LR stacks and the downsampling operator between the LR slices and the HR volume.
The slice profile can describe the downsampling part of the acquisition model [64].

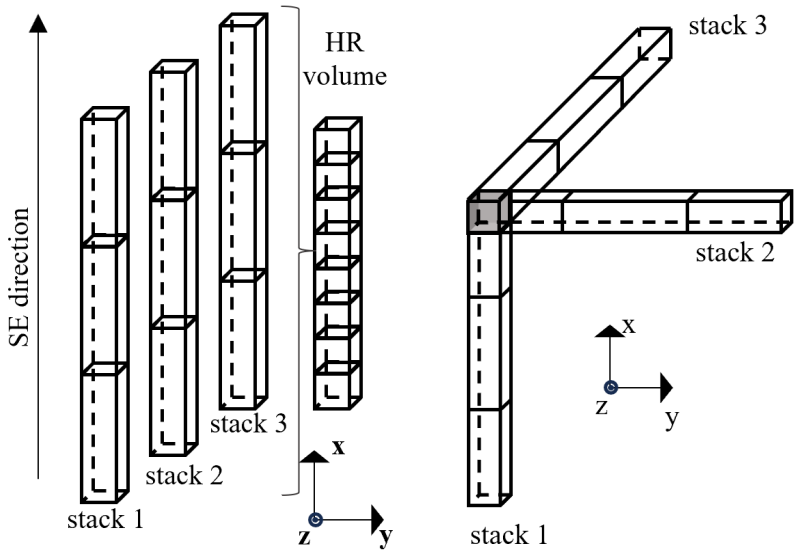

(a) parallel stacks (b) orthogonal stacks

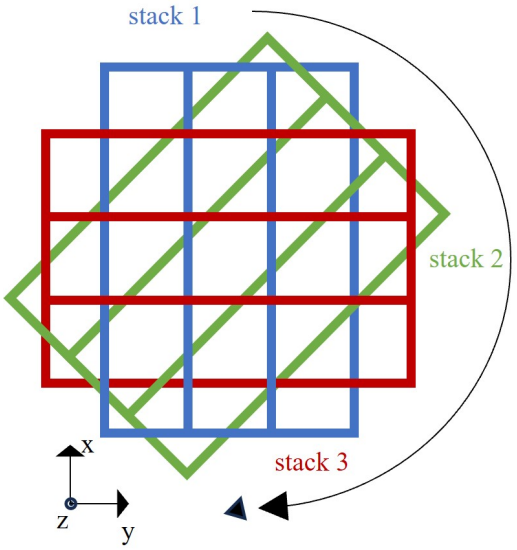

(c) rotated stacks

Figure 2.10: SRR geometries

The geometric transform describes the different points of view from the single LR stacks, for which three different sorts of geometries are most common: Parallel, orthogonal and rotated stacks acquisition (see Figure 2.10):

- **Parallel stacks:** Multiple parallel LR stacks are obtained and shifted along the SE direction by a known distance that is smaller than the slice thickness. To achieve isotropic resolution, a minimum of N LR stacks are required [64], where N is the ratio between the resolution in the through-plane dimension over the resolution in the in-plane dimension. This approach was used in [73, 68, 74].
- **Orthogonal stacks:** Three different stacks are acquired, each taken in orthogonal orientations, such as sagittal, transverse, and coronal. For each LR direction of one stack,

two other stacks compensate for it with their HR along that direction. This has been used in [75–83].

- **Rotated stacks:** This is an extended version of the orthogonal acquisition method, where several LR stacks are acquired, which are rotated around one common encoded axes. This approach was used in [84–88].

The geometric transform in stationary objects involves introducing artificial motion by shifting or rotating the scanning plane by a predetermined amount. In the case of a moving subject, however, part of this transformation comes from the motion generated by the subject itself, which cannot necessarily be controlled. Motion estimation, therefore, plays a crucial role in SRR and is a major factor influencing the quality of the reconstruction [64]. Especially in the context of SRR application on fetal imaging, motion correction plays an important role [89–91, 75, 77].
To account for motion in between the LR stacks, the motion can either be detected once before the SRR and the geometric transform updated accordingly or the motion detection and correction can be incorporated into the SRR problem. [92, 78] compensated for motion by adjusting the transformation parameters of the motion operator before estimating the HR T_1 maps. These adjusted parameters were then fixed and used in the subsequent SRR routine. However, fixing the motion parameters could introduce inaccuracies in the SRR result, as there was no feedback mechanism to correct any incorrect estimation of motion parameters. Alternatively, motion detection and correction can be incorporated into the SRR problems, as [83–85, 93] proposed a SRR with joint motion estimation.

For quantitative relaxometry MRI, there are two different approaches for reconstructing a HR quantitative map: In the first approach, SRR is used to reconstruct HR dynamics independently from a group of LR images with equal contrast weighting and the quantitative parameters are calculated by applying a parametric quantitative MRI signal model to these reconstructed HR dynamics voxel by voxel [77]. The second approach, however, incorporates the quantitative MRI signal model into the SRR [88, 94, 84, 85], called "model-based SRR". This allows for direct estimation of the HR parameter map volume from the LR dynamics without the need to first reconstruct individual HR dynamics. Furthermore, the signal model introduces prior knowledge into the optimisation problem and serves as a regularisation.

Commonly, SRR is image-space-based, so the acquired k-space data is reconstructed in a preprocessing step, and the resulting images then serve as input for the SRR. Errors happening during that preprocessing step, then, however, propagate into the SRR result. As an alternative, SRR can also be applied to the raw k-space data, as proposed with a k-space-based reconstruction in [94, 93]. This improved the visualisation of small structures compared to an image-space-based reconstruction.

The application of SRR on the heart [95–98, 93, 76, 78, 79] has so far only been shown for qualitative imaging. For T_1 mapping, SRR taking into account different motion states of the individual LR stacks has so far only been applied on the brain [88, 85, 84].

Table 2.1 gives an overview over the existing literature on multi-image SRR, marked which publication used motion correction, a k-space-based SRR, applied SRR on cardiac applications and performed quantitative parameter estimation with SRR.

	cardiac	**quantitative**	**motion correction**	**k-space based**
proposed approach	x	x	x	x
[93]	x		x	x
[92, 79, 76, 81, 78]	x		x	
[84, 85, 88]		x	x	
[94]		x		x
[96, 97]	x			
[77, 82]		x		
[99–103, 75, 89–91]			x	

Table 2.1: Existing literature on multi-image SRR. Crosses in the appropriate column indicate which topics were covered by the respective research paper.

3

T_1 mapping of a single cardiac multi-slice stack

3.1 Introduction

In cardiac T_1 mapping, a significant challenge is the limitation of spatial resolution caused by respiratory and cardiac motion, low SNR, and limited acquisition time. In clinical routine, T_1 maps are typically obtained using a 2D acquisition method with a high resolution within the image plane but a low through-plane resolution [54]. With the work proposed in [53–55], a single cardiac 2D LR T_1 map with a spatial resolution of 1.3 x 1.3 x 8.0 mm^3 with accurate T_1 estimates could be acquired in 2.3 seconds. However, the spatial resolution is still compromised by partial volume effects, which can hinder the accurate detection of subtle fibrosis in the myocardium and the differentiation of myocardial injury, for example, in young patients with thin myocardial walls.

SRR has been suggested as a potential solution to improve the trade-off between spatial resolution, acquisition time, and SNR [59]. SRR calculates a HR volume based on several LR multi-slice stacks, where the LR stacks are, for example, shifted to one another by a sub-voxel shift along the SE direction. The HR volume then profits from the high SNR of the LR slices. The acquisition time for the SRR result consists of the sum of the acquisition times of the single multi-slice LR stacks. So, for the HR volume to be acquired in a fast acquisition time, the acquisition time for a single multi-slice LR stack needs to be minimised while still providing accurate values.

With the method proposed in [53–55], a single cardiac 2D LR T_1 map with accurate T_1 estimates could be acquired, however, a non-selective inversion pulse was used. With the use of a non-selective inversion pulse in a multi-slice sequence, all slices of the stack would be inverted, and waiting times between the slices would be necessary to get an accurate T_1 estimate of all slices.

In this chapter, the use of a slice-selective inversion pulse will be investigated to avoid waiting times between the slices. The sequence parameters for a multi-slice acquisition, such as

the width of the inversion pulse and the gap between the slices, will be adapted to provide independence between the slices and an accurate inversion of the whole slice. Next to that, for the LR multi-slice stack to provide accurate T_1 estimates in a low acquisition time, high SNR of the slices needs to be ensured. Therefore, the relationship between slice thickness, number of spokes and SNR will be investigated for the proposed T_1 mapping sequence. The precision and accuracy of the acquisition of a LR multi-slice stack with the proposed parameters will be evaluated in phantom and *in vivo* experiments using a model-based T_1 reconstruction and cardiac motion correction.

3.2 Methods

An acquisition and reconstruction technique of a single multi-slice stack is investigated in the following. For each slice of the multi-slice stack, a slice-selective inversion pulse with experiment-specific width is applied, followed by a Golden-angle radial readout, as described in [54, 55]. The respective data is then reconstructed using a model-based T_1 reconstruction and cardiac motion correction [53].

3.2.1 Cardiac motion correction

Cardiac motion correction is performed as described in [53]. For that, dynamic cardiac motion-resolved images are reconstructed. Spatial and temporal total variation regularisation is applied to suppress undersampling artefacts [104]. A subject-specific rectangular region of interest ROI interest covering both ventricles is selected to accelerate the motion estimation. Iteratively, the non-rigid cardiac motion fields are estimated using the MIRTK Toolkit [105].

3.2.2 Model-based T_1 reconstruction

T_1 maps are reconstructed directly from the acquired k-space data using an iterative model-based T_1 reconstruction scheme [54, 55]. A Look-Locker model q is used in an iterative reconstruction scheme to estimate the parameter maps γ^m with the quantitative parameter $m = [p, \alpha, T_1]$ and the T_1-weighted images (dynamics) χ. p denotes the equilibrium magnetisation and α the readout flip angle. γ^m has the dimensions N_x x N_y, and χ the dimensions N_T x N_x x N_y (with N_x and N_y being the number of voxels in the image and N_T being the number of dynamics).
The primary focus in the following is on the T_1 parameter as it is clinically the most relevant, so γ^{T_1} will be referred to as γ in the following.

3.2.3 *In vivo* T_1 mapping

The proposed motion estimation and correction scheme can only correct for motion within the imaging plane. However, during the peak systole phase, when the heart muscle contracts, there can be significant motion in the through-plane direction. To avoid inaccuracies in the T_1 estimation, data acquired during peak systole, respective to 30% of the systole phase, are excluded for the cardiac motion estimation, as described in [53]. The regularisation parameters along time and space were set to 0.5.

3.3 Experiments

3.3.1 Data acquisition

Data was acquired using a Golden-angle radial sampling scheme. After a RF inversion pulse, data was continuously acquired with the following parameters: flip angle α=9°, in-plane resolution of 1.3×1.3 mm^2, experiment-specific slice thickness, in-plane FOV 320×320 mm^2, echo time (TE) / repetition time (TR): 2.19/4.9 ms. Data was acquired using a 3 Tesla MRI scanner (Verio, Siemens Healthineers, Erlangen, Germany).
For multi-slice acquisitions, the slices were acquired in an interleaved order to avoid interferences between them. For example, for the acquisition of six slices, an interleaved sequence acquires their positions in the following order: 1, 3, 5, 2, 4, 6. As a consequence, the spatial distance between the acquisition of two consecutive slices is maximised.
For cardiac motion correction, dynamic cardiac motion-resolved images were reconstructed with a temporal resolution of 51.3 ms (1 spoke = 5.7 ms). A sliding window approach with a 50% overlap was used. For the model-based T_1 reconstruction, a temporal resolution of 83.3 ms was used.

Simulation

Simulated data was generated using the XCAT phantom [106]. A dataset $ref_{XCAT,orig}$ with a voxel size of 1.3 x 1.3 x 1.5 mm^3 was generated. From this, one LR multi-slice stack with five slices in SAX was simulated with a slice thickness of 4 mm and a gap between the LR slices of 14 mm.
The default settings of the XCAT phantom were used to simulate the motion of the heart.
Multiple receiver coils were used to simulate the data acquisition, and zero-mean noise was added. This allowed the application of the model-based T_1 reconstruction and cardiac motion correction on the simulated k-space data.
In the simulations, a T_1 time of 1300 ms was assigned to the myocardium, 400 ms to fat, 800 ms to the liver and 900 ms to muscle. Blood was simulated with an apparent T_1 time of 350 ms to match the experimental results. The underestimation of blood can be attributed to the in-flow effect as a consequence of the slice-selective inversion pulse [107], as will be further explained in section 3.5.

Phantom

The proposed approach was assessed in phantom measurements, using the "T1MES-phantom" with nine tubes with different T_1 times developed for cardiac imaging [108]. Phantom data was acquired with a 16-channel head coil.
To evaluate the accuracy of the estimated T_1 values, an IR spin-echo reference scan ref_{IRSE} was acquired, in the orthogonal direction to the LR slices with seven TIs between 25 and 4800 ms (TE/TR: 12/8000 ms, FOV: 143 × 160 mm^2, spatial resolution: 0.8 × 0.8 × 5 mm^3).

In vivo

To evaluate the proposed approach in *in vivo* measurements, data was obtained from one healthy subject with a commercial 32-channel cardiac coil. The subject gave written informed

consent before participation in accordance with the institution's ethical committee. One LR stack consisting of five slices in SAX with a slice thickness $\Delta z = 4$ mm and a gap between the slices of 14 mm was acquired.

3.3.2 SNR in quantitative T_1 maps

As mentioned previously, high SNR needs to be made sure to provide accurate T_1 estimates. As set up in Equation 2.6, the SNR in qualitative MRI scales linearly to the voxel size and the square root of the number of radial spokes. However, this relationship neither considers the non-linear signal model nor the continuous readout of the proposed T_1 mapping sequence. The following chapter, therefore, evaluates the influence of N and Δz on the SNR experimentally for different Δz and N using the proposed T_1 mapping sequence.
The acquired k-space data was reconstructed using a non-uniform FFT [109, 110] to avoid regularisation effects of the model-based reconstruction.
The SNR is approximated by one over the standard deviation (SD) in a ROI of the fitted T_1 values in the phantom tubes:

$$SNR = \frac{1}{SD(T_1)} \tag{3.1}$$

The experimental results were compared to the theoretical SNR relationship between N and Δz based on Equation 2.6. For this, the values predicted by the model were normalised to the first experimentally determined SNR value, thus predicting the course of this SNR value corresponding to the model.

3.3.3 Inversion pulse

As mentioned previously, a slice-selective inversion pulse is used to avoid waiting times between the slices of the multi-slice stack. To achieve a rectangular slice profile, an infinitely long sinc-shaped RF would need to be used. As this is not possible in a limited acquisition time, the effective slice profile is usually an approximated rectangle and might not achieve accurate inversion along the entire slice profile. For accurate T_1 mapping, however, the width of the slice-selective inversion pulse needs to be broad enough to invert the whole slice. In addition, through-plane motion can also lead to a mismatch between the inverted and the imaged slice. To optimise the parameters for the inversion pulse, a phantom experiment was performed: A multi-slice stack consisting of six parallel slices with $\Delta z = 6$ mm and a gap in between the slices of 6 mm was acquired once using a non-selective inversion pulse and once using a slice-selective inversion pulse with $w = 3$. The respective T_1 accuracy was evaluated and compared.

In a further experiment, six LR stacks were acquired, each consisting of one slice with a different width w of the inversion pulse in the range of $w = [1, ...5]$ next to an acquisition with a non-selective inversion pulse. The factor w thereby denotes the width of the inversion pulse normalised by the slice thickness:

$$w = \frac{\text{thickness of slice selective inversion pulse}}{\Delta z} \tag{3.2}$$

This experiment was performed for two different Δz (4 mm and 8 mm). The mean error of the fitted T_1 values in a ROI in each phantom tube with respect to a non-selective inversion was then calculated. For each Δz, the experiment was performed for two scenarios: Once for a static case, and once motion was simulated, for example, in the case of a non-consistent BH. A moving phantom was used to mimic breathing motion, as described in [57], where the T1MES-phantom was placed onto a moving wagon. To mimic the natural movement of breathing, the wagon moved in a sinusoidal pattern along the head-feet direction of the scanner. With that, the phantom moved with a speed of 1 cm/s along the SE direction during the acquisition.
As mentioned above, the acquired k-space data was reconstructed using a non-uniform FFT [109, 110] to avoid the regularisation effects of the model-based reconstruction.

3.3.4 Gap in between LR slices

With a certain inversion pulse width, the slice-selective inversion pulses influence neighbouring slices. Gaps might reduce potential interferences between slices within one stack in between the LR slices. The necessity of gaps in between the LR slices was therefore investigated in phantom experiments to provide accurate T_1 values.
Different acquisitions with six slices per stack with a thickness of $\Delta z = 6$ mm and gaps in the range of [0, 6] mm between the slices were performed to evaluate that. The error of the fitted T_1 values in a ROI of the phantom tubes compared to ref_{IRSE} was calculated over all tubes and all slices.
As mentioned above, the acquired k-space data was reconstructed using a non-uniform FFT [109, 110] to avoid the regularisation effects of the model-based reconstruction.

3.4 Results

3.4.1 SNR in quantitative T_1 maps

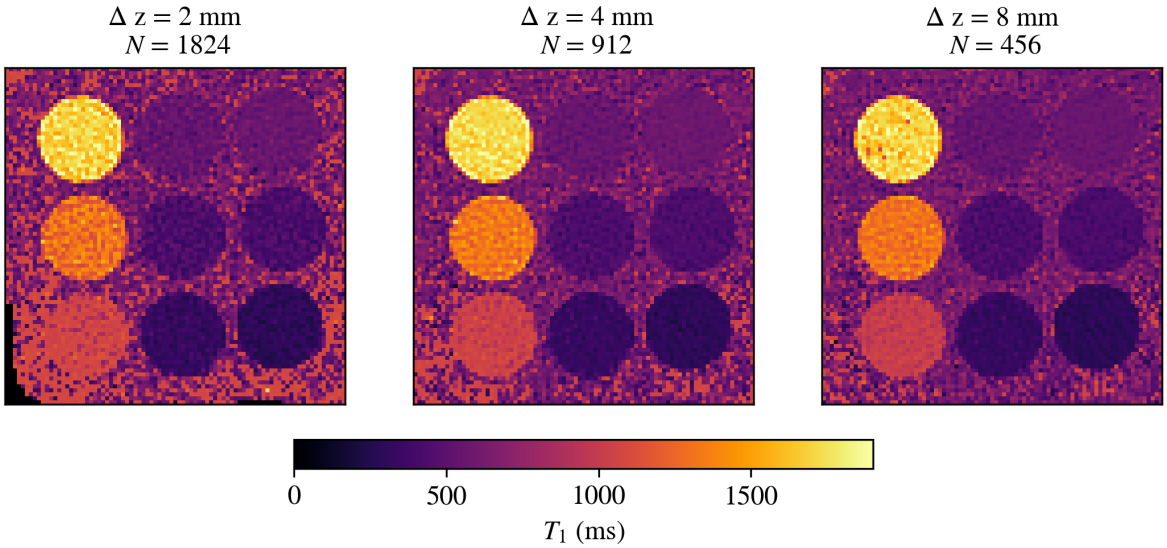

Figure 3.1: T_1 maps acquired in phantom scans with different slice thickness Δz and number of spokes N

Figure 3.1 shows the T_1 maps acquired in phantom scans for different Δz and different number of spokes (N). The T_1 maps resulting from $\Delta z = 2$ mm visually appear more noisy compared to $\Delta z = 8$ mm.

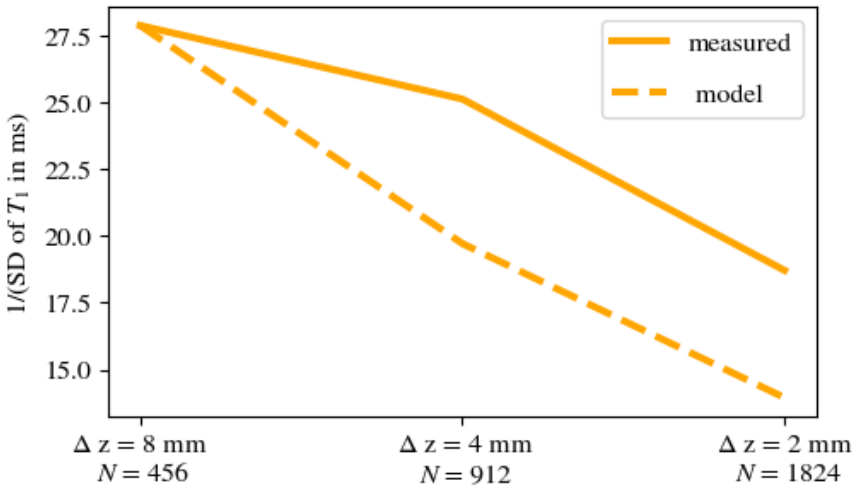

Figure 3.2: Influence of the slice thickness Δz and the number of radial spokes N on the SNR for the measured experiments and the simplified model

In Figure 3.2, the respective comparison between the calculated SNR of the fitted T_1 values in the phantom tubes and the one predicted by Equation 3.1 is plotted. The measured results for the SNR in the quantitative maps matched the non-linear relationship between N and Δz as predicted from the model. Doubling N and halving Δz led to a decrease in the SNR.

However, the measured SNR values decreased more slowly than predicted. While doubling N and halving Δz led to a predicted reduction of the SNR of a factor of $\sqrt{2}/2 \approx 0.71$, the measured SNR was only reduced by a factor of 0.82 ± 0.08 in that case.

3.4.2 Inversion pulse

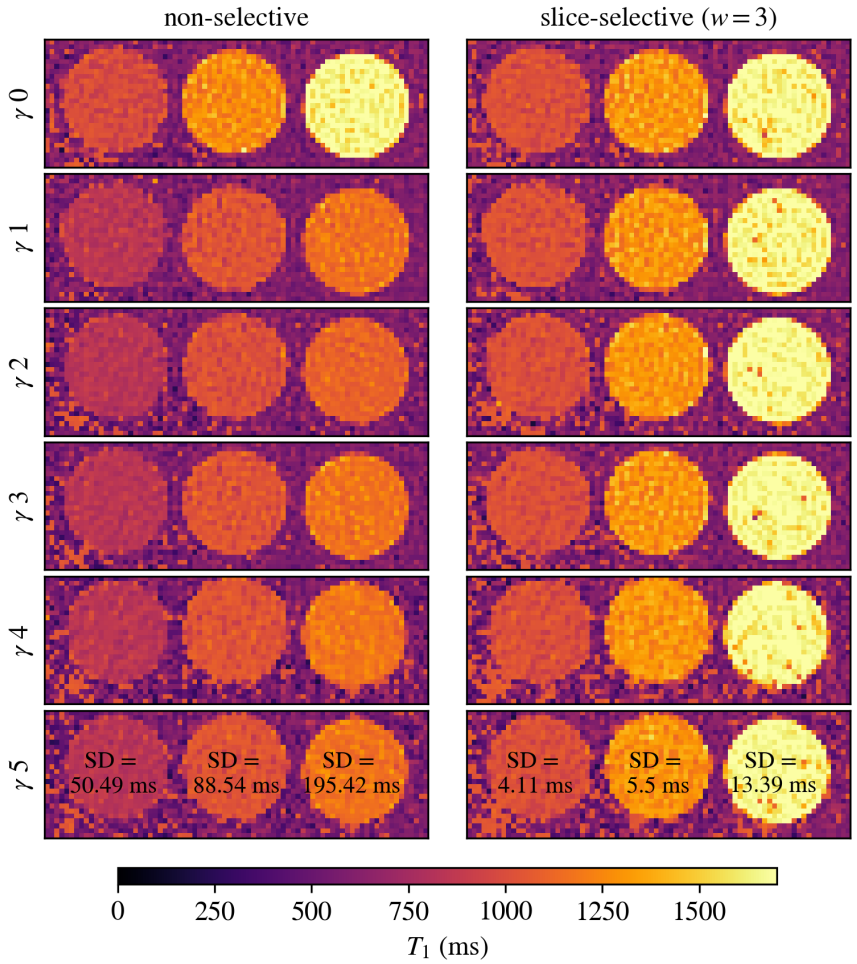

Figure 3.3: Comparison of a multi-slice phantom stack acquisition of five slices with a non-selective inversion pulse and a slice-selective inversion pulse with $w = 3$. The superscript of γ indicates the acquisition order of the slices. The values in the phantom tubes in the lower row indicate the SD over the slices of the respective tube.

In Figure 3.3, the acquisition of a multi-slice stack in a phantom experiment with a non-selective and a slice-selective inversion pulse ($w = 3$) is shown. The T_1 values in the slices using a non-selective inversion pulse showed a high SD in their T_1 values between the slices of 111.48 ± 61.35 ms. The T_1 values using a slice-selective inversion pulse were more precise, with a mean SD between the slices of 7.67 ± 4.09 ms.

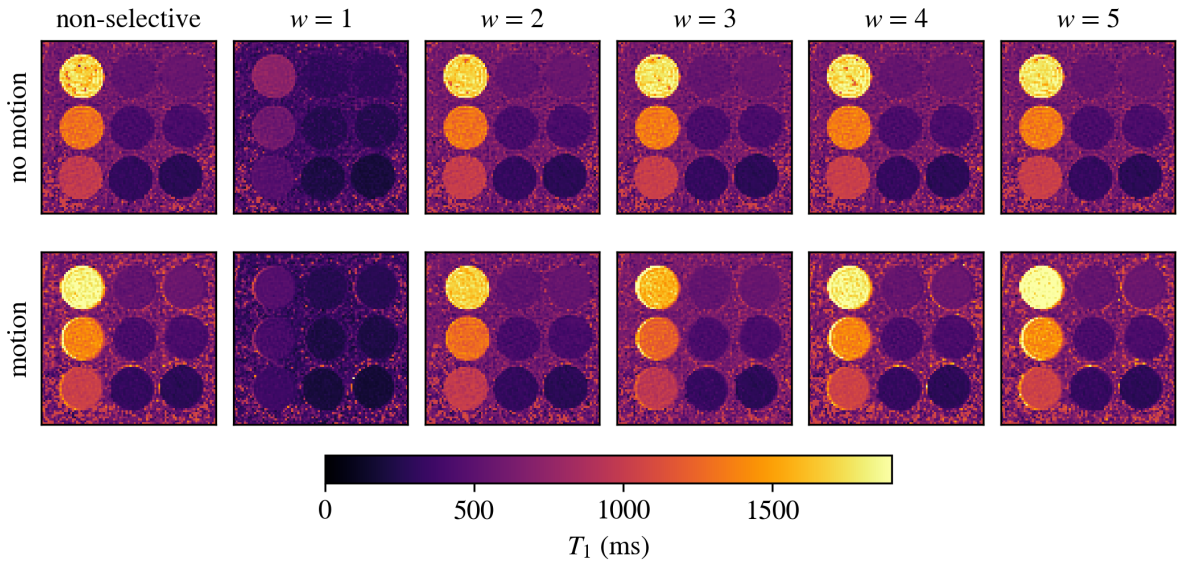

Figure 3.4: T_1 maps of phantom experiments with different inversion pulse width with $\Delta z = 8$ mm. The upper row shows the static phantom, while the lower row shows the phantom placed onto a moving phantom mimicking breathing motion.

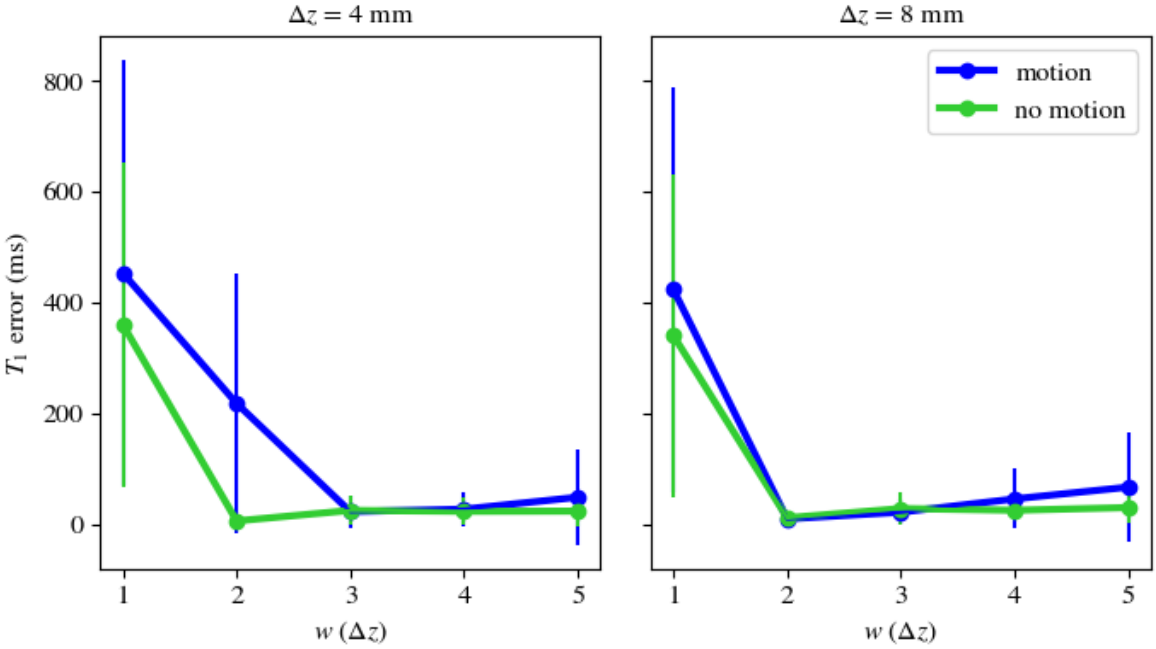

Figure 3.5: Influence of the width w of the slice selective inversion pulse on the T_1 estimation error for $\Delta z = 4$ mm and $\Delta z = 8$ mm compared to the use of a non-selective inversion pulse. The results using a moving phantom are shown in blue, while the static results are shown in green. The error bars indicate the SD over the phantom tubes.

In Figure 3.4 the resulting T_1 maps from phantom scans with different w are shown with and without motion for $\Delta z = 8$ mm. Figure 3.5 shows the respective error of the T_1 times over different w for $\Delta z = 4$ mm and $\Delta z = 8$ mm. The static case is shown in green, while a moving phantom was used for the blue plot. In both cases, a factor of $w = 1$ was not sufficient to provide accurate T_1 values (T_1 error of 350.04 ± 292.53 ms for the static phantom and of 438.09 ± 375.16 ms for the moving case over both Δz). With $\Delta z = 8$ mm, in both the

static and moving case, a factor of $w \geq 2$ decreased the error to 29.4 ± 47.01 ms. With a slice thickness of $\Delta z = 4$ mm, in the case of motion, a width of $w \geq 3$ was necessary for accurate T_1 quantification. The error over both motion states and all tubes decreased with $w \geq 3$ to 32.37 ± 56.35 ms for $\Delta z = 4$ mm.

3.4.3 Gap in between the LR slices

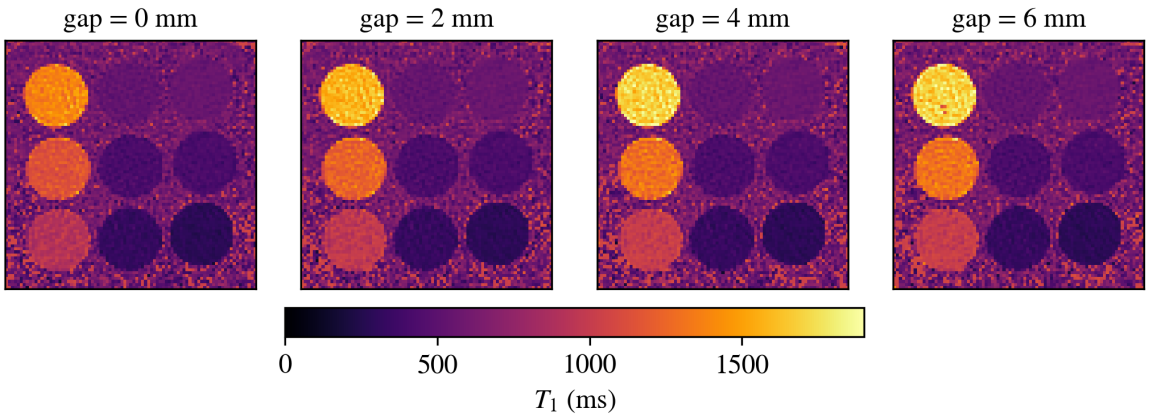

Figure 3.6: T_1 maps of phantom experiments for different slice gaps with $w = 3$ and $\Delta z = 6$ mm

In Figure 3.6, one T_1 map of each multi-slice stack acquired in phantom acquisitions with different gaps in between the LR slices is shown. The respective error of the T_1 times compared to ref_{IRSE} is plotted in Figure 3.7. This shows the mean T_1 error compared to ref_{IRSE} of the phantom tubes over different gaps between the slices of the stack. The error decreased by 59.59 ± 25.17 % to 9.82 ± 6.38 ms when introducing a gap of at least 4 mm compared to no gap.

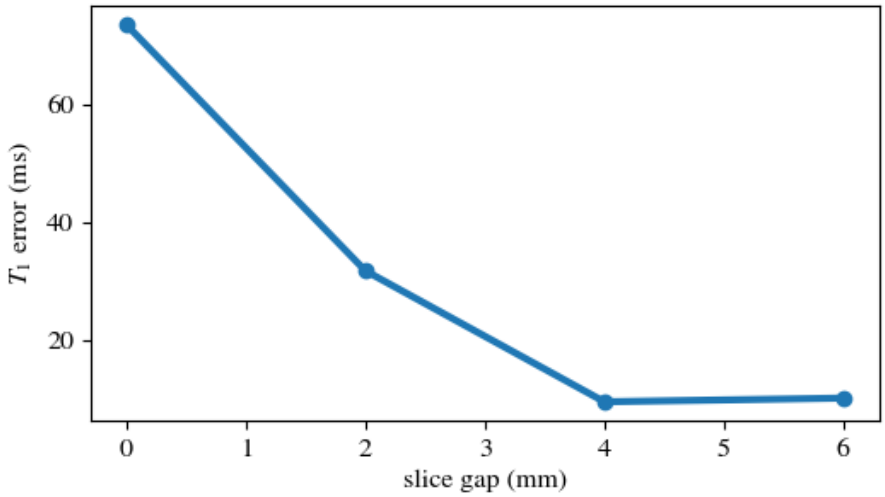

Figure 3.7: Influence of slice gap on T_1 estimation error with $w = 3$ and $\Delta z = 6$ mm

3.4.4 Cardiac motion correction and model-based T_1 reconstruction

Figure 3.8 shows the effect of the cardiac motion correction on both the dynamics and the resulting T_1 maps. Three exemplary dynamics at different time points during the cardiac cycle are shown next to a spatial-temporal plot along the blue line over the dynamics. In the original images, the heart motion is visible as temporal changes of the septum and the ventricular walls. Motion correction ensured that all images were in the same cardiac phase. In the respective T_1 map, cardiac motion correction improved the distinction between the papillary muscle and blood, as highlighted by the arrow.

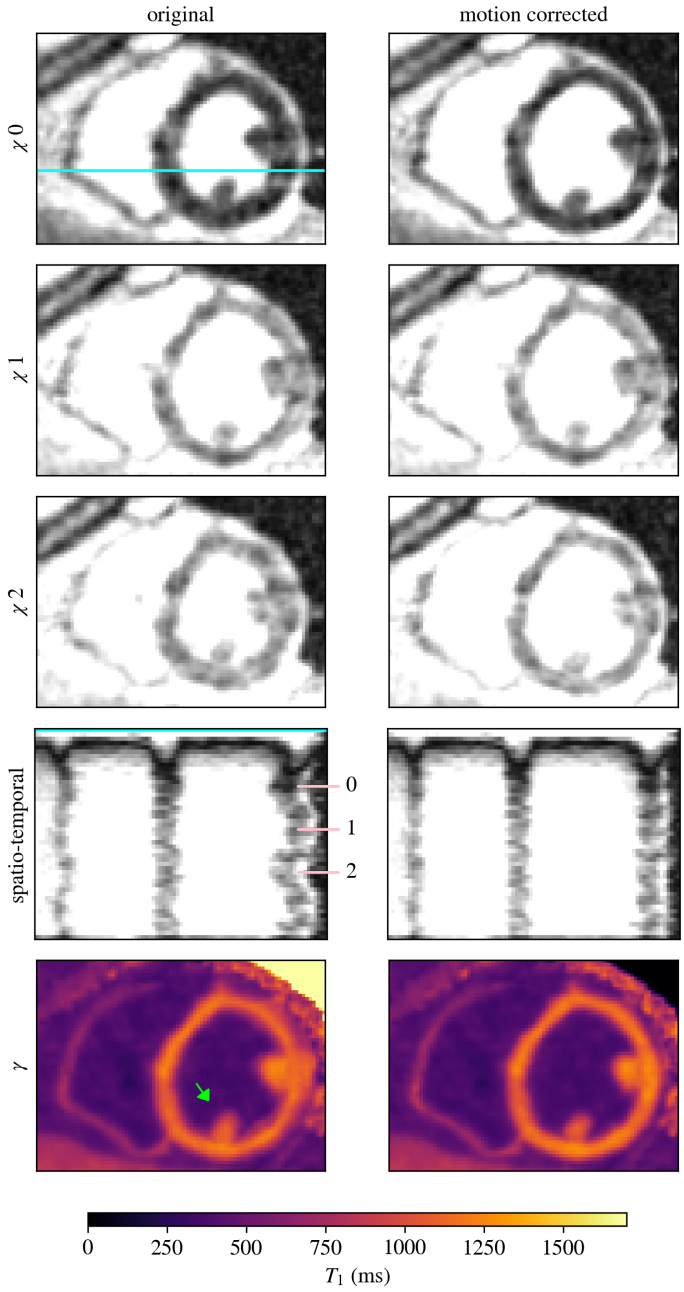

Figure 3.8: The effect of cardiac motion correction on three exemplary dynamics χ at different time points during the data acquisition next to a spatiotemporal plot over the values along the blue line. The respective T_1 map γ reconstructed by the model-based T_1 reconstruction is plotted in the lower row. Artefacts could be reduced using motion correction, as highlighted by the arrow.

3.4.5 *In vivo* T_1 mapping

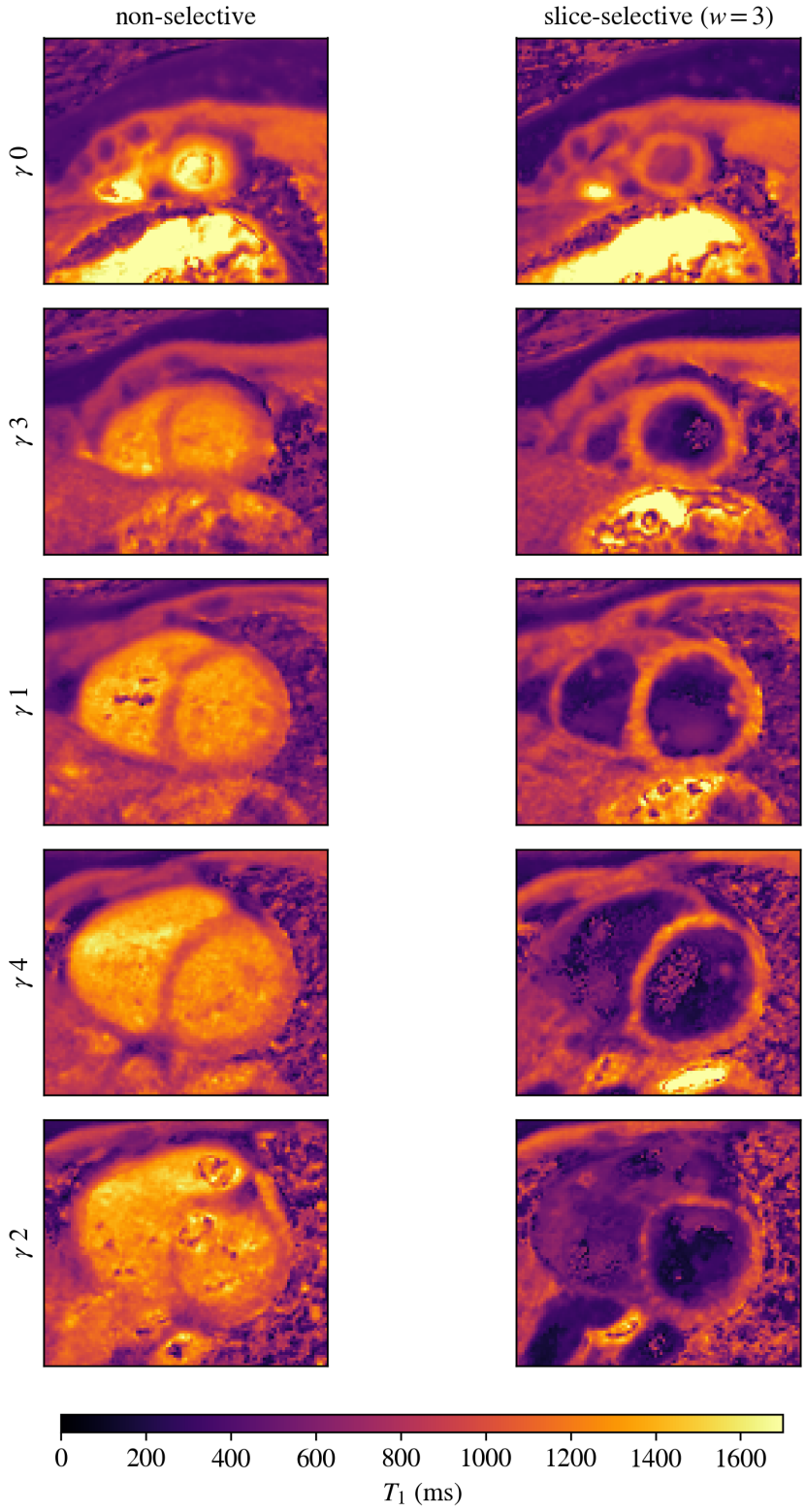

Figure 3.9: Comparison of a multi-slice *in vivo* stack acquisition of five slices with a non-selective inversion pulse and a slice-selective inversion pulse with $w = 3$. The superscript of *gamma* indicates the scan order.

In Figure 3.9, the acquisition of a multi-slice stack with five slices in a single BH *in vivo* is compared between the use of a slice-selective inversion pulse with $w = 3$ and a non-selective one. The superscript of the different rows indicates the scan order of the slices, which is interleaved, as explained in subsection 3.3.1.
With the use of a non-selective inversion pulse, interference between the slices could be seen: While the mean T_1 value between the first (γ^0) and the second (γ^1) acquired slice varied by 43.65 ms with a slice-selective inversion pulse, these slices varied by 132.67 ms when using a non-selective inversion pulse. These results match the results from the phantom experiment as shown with Figure 3.3.
Blood could not be quantified due to a slice-selective inversion pulse.

3.5 Discussion

In this chapter, the acquisition of a multi-slice stack was optimised for maximum SNR and accurate T_1 values of a multi-slice stack of six slices in an acquisition time of 17 seconds for a stack with six slices.
A slice selective inversion pulse was used to avoid waiting times and slice interference. An inversion width factor of $w = 1$ was not sufficient due to the non-rectangular shape of the inversion pulse. A factor of $w = 2$ inverted the whole slice and provided accurate T_1 times in the static case. In the case of motion with a velocity of 1 cm/s, the width of the inversion pulse needed to be broader ($w = 3$) to avoid non-inverted tissue emerging into the slice during the acquisition.
However, a factor of $w \geq 1$ might lead to interference between the slices, even though a slice-selective inversion pulse is used, as adjacent slices to the inverted one might also experience some inversion. Due to the interleaved acquisition order, not the directly adjacent slice is acquired afterwards but one with a greater distance along the SE direction, so there are 5.6 seconds between the excitation of two neighbouring slices. However, after the application of an inversion pulse, for the myocardium with a T_1 time of approximately $T_1 = 1.3$ seconds and a sequence with $\alpha = 5°$ and TR= 0.0049 seconds, it takes about 6.9 seconds for its longitudinal magnetisation to have recovered to 99% of M_0. With a time delay of only 5.6 seconds between two neighbouring slices, however, 1.3 seconds are still left, in which the longitudinal slice of this directly neighbouring slice might not have yet recovered to M_0. An accurate T_1 estimate of all slices made a slice gap of at least 4 mm necessary to avoid interference between the slices, as shown experimentally.
Due to hardware limitations, the inconsistent BH motion was simulated with a speed of 1 cm/s. However, this is slower than the velocities reported in the literature [111], with 1.7 and 1.5 cm/s for diaphragmatic inspiratory and expiratory velocities, respectively, in women and 1.8 and 1.5 cm/s, respectively, for men. The motion experiment did not involve cardiac motion simulation since this follows a more complex pattern compared to inconsistent BH motion. Therefore, a broadening motion buffer of the inversion-pulse width combined with gaps between the LR slices should be used to account for various *in vivo* motion effects not considered in the proposed experiment.
The blood spins within the excited slice were the only ones affected by the slice-selective

inversion pulse. Throughout the cardiac cycle, these spins were replaced by incoming, non-inverted blood spins, which led to an apparent shortening of the T_1 value of the blood [107]. As a consequence, blood could not be quantified. To still be able to calculate the ECV, the necessary information about the blood pool T_1 values could be obtained with a further fast acquisition of a single LR slice with a global inversion pulse.
The relationship between the number of radial spokes and the slice thickness on the SNR of the proposed T_1 mapping approach matched the non-linear relationship described in the literature [60, 59]. A decrease in SNR in the proposed approach smaller than predicted by the model could be attributed to the influence of the non-linear signal model and the signal model fit being robust to a certain extent with respect to noise in the dynamics and serving as a sort of regulariser. A Δz of 8 mm resulted in the highest SNR.
The implementation of cardiac motion correction allowed using approximately 85% of the cardiac cycle data for the calculation of the T_1 map. The cardiac motion correction led to an improved distinction between ventricles and blood. As mentioned in section 2.1, the ventricular and atrial systole are offset in time. However, the cardiac motion correction scheme used in the proposed work was optimised for the application on the ventricles. For the application of the proposed cardiac motion correction scheme on the atria, this offset needs to be considered to also provide accurate T_1 estimates of the atrial walls.

3.6 Conclusion

In this chapter, the sequence parameters for the acquisition of a single multi-slice LR stack were optimised to provide accurate T_1 times and minimise the acquisition time to 17 seconds per stack of six slices. For this, a slice selective inversion pulse was used with a specific width, under consideration of its non-rectangular shape as well as the effect of a potentially non-consistent BH. Cardiac motion correction was applied. Next to that, it was shown that an increase in slice thickness also leads to an increase in SNR for quantitative T_1 mapping, motiving the use of SRR to reconstruct a HR volume out of several LR stacks, as discussed in the next chapter.

4

Model-based SRR T_1 mapping of the ventricles

4.1 Introduction

In the previous chapter, the acquisition of a multi-slice stack within one BH was shown. However, the acquired slices had a low through-plane resolution. With SRR, a HR volume can be reconstructed from multiple LR stacks, profiting from their high SNR and low acquisition time. For quantitative imaging, the quantitative signal model can be incorporated into the SRR to improve the accuracy of the parameter estimates of the SRR result with respect to the root mean squared error (RMSE) to the reference [88].

The acquisition model must be described accurately for a successful SRR. This model consists, among other things, of the relationship between a LR and HR slice, which can be described by the slice profile [64]. Due to hardware limitations, the slice profile that is ultimately applied during the MRI scan may differ from the one originally planned. In the literature, the slice profile is often modelled by a Gaussian function with a FWHM of the slice thickness [68, 102], a smoothed box function [112, 113, 88] while only some measured the slice profile [114]. [115] has shown that inconsistencies between the slice profile used for the forward model and the one used for the reconstruction lead to errors in the SRR result.

Next to that, the acquisition geometry between the LR stacks needs to be known. Unknown motion between the stacks can significantly affect the quality of the SRR [64].

So far, model-based SRR has not been applied to cardiac T_1 mapping, posing further challenges due to breathing and cardiac motion. Different BH positions of the single LR stacks might deteriorate the SRR result. Next to that, the influence of slice profile inaccuracies and motion in between the LR stacks has not yet been evaluated for cardiac quantitative imaging.

In this chapter, a model-based SRR approach for quantitative cardiac T_1 mapping is introduced. Furthermore, the influence of slice profile inaccuracies and motion on the accuracy of the provided T_1 estimates is investigated.

Parts of this chapter were published in J1.

4.2 Methods

In this chapter, a model-based SRR approach for cardiac T_1 mapping is presented, reconstructing a HR T_1 map from the dynamics of the LR stacks and thereby considering the T_1 signal model in the reconstruction. For this, an optimisation problem is set up, which is solved using a variable splitting approach.

4.2.1 Model-based SRR

As mentioned previously, for SRR, several LR stacks acquired with an offset to each other are combined to an HR volume. To estimate that HR volume, LR slices are predicted, and the difference between the acquired LR dynamics χ and the predicted ones is minimised. LR slices are predicted from a HR volume using A. A_s is a matrix describing the relationship between a HR slice with respect to a LR slice of stack s (with $s = 1, \ldots, N_S$ and N_S being the number of stacks). To also make sure the predicted LR slices still match the T_1 signal model q, model-based SRR is used. q_t calculates dynamics from given parameter maps at inversion time t (with $t = 1, \ldots, N_T$ and N_T being the number of inversion times). The model-based SRR incorporates q into SRR to, at the end, obtain a HR parameter volume Γ from the acquired LR dynamics.
The SRR is implemented as a functional based on the sum of the differences between the predicted LR dynamics and χ, together with a total variation-based regularisation term. This functional is minimised, which can be described by the following minimisation problem:

$$\min_{\Gamma} \sum_{t=1}^{N_T} \sum_{s=1}^{N_S} ||\chi_{t,s} - A_s * q_t(\Gamma)||_2^2 + \kappa \|G * \Gamma||_1 \tag{4.1}$$

Regularisation is used to make the solution of the optimisation problem unique, with κ describing the regularisation parameter and G corresponding to the forward finite differences operator. Γ has the dimensions N_x x N_y x N_z (with N_x and N_y being the number of voxels in the image and N_z being the number HR slices)

4.2.2 Variable splitting approach

Since solving problem 4.1 directly is challenging due to the non-smoothness of the L1-norm as well as the non-linear function q, a variable splitting [116, 94, 93] approach is used. This allows for splitting the original problem into several sub-problems and solving them with suitable algorithms. By introducing auxiliary variables $x_t := q_t(\Gamma)$ for all t and $u := \Gamma$, the problem is reformulated as a joint minimisation problem. These equalities are relaxed by including two quadratic penalty terms, weighted by λ and μ, yielding:

$$\min_{\Gamma,x,u} \sum_{t=1}^{N_T} \sum_{s=1}^{N_S} ||\chi_{t,s} - A_s * x_t||_2^2 + \lambda ||x_t - q_t(\Gamma)||_2^2 + \mu ||u - \Gamma||_2^2 + \kappa ||G * u||_1 \tag{4.2}$$

The solution of problem 4.2 is approached by alternating the minimisation of 4.2 with respect to one of the variables and keeping the other two fixed.

For fixed Γ, u, updating x corresponded to solving

$$\min_{x} \sum_{t=1}^{N_T} \sum_{s=1}^{N_S} ||\chi_{t,s} - A_s * x_t||_2^2 + \lambda ||x_t - q_t(\Gamma)||_2^2 \tag{4.4.1}$$

Solving 4.4.1 involves solving a linear system for which a conjugate gradient approach is used. Ten iterations were used per alternation.

For fixed Γ, x, updating u corresponds to solving

$$\min_{u} \frac{\mu}{\kappa} ||u - \Gamma||_2^2 + ||G * u||_1 \tag{4.4.2}$$

Subproblem 4.4.2 is solved using the iterative algorithm proposed in [117].

For fixed u and x, updating Γ corresponds to solving

$$\min_{\Gamma} \sum_{t=1}^{N_T} \lambda ||x_t - q_t(\Gamma)||_2^2 + \mu ||u - \Gamma||_2^2 \tag{4.4.3}$$

In this work, the Limited-memory Broyden–Fletcher–Goldfarb–Shanno algorithm [118] is used to solve the non-linear problem 4.4.3. Four iterations were used per alternation.

To solve Equation 4.2, the subproblems are alternated eight times and the solution of Equation 4.2 is referred to as Γ_{final}.
As initialization Γ_0 of the SRR, LR maps γ are calculated from χ using a voxel-wise three-parameter T_1 fit and combined using the weight $A_s^{h,l}$ of HR slice h with respect to LR slice l in stack s (with $h = 1, ..., N_H$, $l = 1,..., N_L$ and N_H and N_L being the number of HR-slices and the number of LR-slices, respectively)

$$\Gamma_0^h = \sum_{s=1}^{N_S} \sum_{l=1}^{N_L} \sum_{h=1}^{N_H} A_s^{h,l} \gamma_s^l \tag{4.3}$$

4.3 Experiments

4.3.1 Data acquisition

Similar to subsection 3.3.1, data was acquired using a continuous Golden angle radial sampling scheme after applying a slice-selective inversion pulse. A flip angle $\alpha = 5°$ was used.
Simulated data was generated using the XCAT phantom [106]. A dataset $ref_{XCAT,orig}$ with a voxel size of 1.3 x 1.3 x 1.5 mm^3 was generated. From this, eight LR stacks with each six SAX slices were simulated with a slice thickness of 6 mm, a gap between the LR slices of 6 mm to cover the whole ventricles and an offset between the stacks of 1.5 mm along the SE direction.

Using this, simulated k-space data was generated. From this, dynamics were reconstructed, cardiac motion was estimated, and T_1 maps were reconstructed, as described in subsection 3.3.1. As a reference, LR dynamics were simulated from $ref_{XCAT,orig}$ by applying q on the LR stacks and convolving them with a slice profile with FWHM of 1.5 mm along the SE direction. These convolved dynamics were fitted using a voxel-wise three-parameter T_1 fit, resulting in ref_{XCAT}.

4.3.2 Assessment of image resolution

Two cubical fibrotic structures with a T_1 value of 1800 ms were simulated in $ref_{XCAT,orig}$ in the septum along the SE direction to evaluate the performance of the proposed SRR approach with respect to the resolution of small structures. They were separated by an experiment-specific gap of healthy myocardium. Different thicknesses of fibrotic structures and the respective gap in between them were simulated in the range of one to five times the HR slice thickness, so in the range of [1.5, ..., 7.5] mm.
To separate the effect of the SRR from any inaccuracies due to incomplete cardiac motion correction and the model-based T_1 reconstruction, this evaluation was carried out using a simplified simulation of LR data, with SRR performed directly on the LR dynamics. Zero-mean noise was added.
The detectability d between the simulated fibrosis and the surrounding healthy myocardium was measured using the following formula:

$$d = \frac{\mu_{structure} - \mu_{nextStructure}}{\sigma_{background}} \tag{4.4}$$

Where the mean T_1 value $\mu_{structure}$ was measured in a ROI within the fibrosis and the mean T_1 value $\mu_{nextStructure}$ was calculated in a ROI within the healthy myocardium between the two fibrotic structures. The placement of the ROI was based on the position of the simulated fibrotic structures in $ref_{XCAT,orig}$. The SD $\sigma_{background}$ was calculated from a ROI in the healthy myocardium.

4.3.3 Influence of slice profile accuracy on SRR

In SRR, the result of the optimisation problem depends on the known relationship between a LR and a HR slice, which can be described by the slice profile of a single LR slice [64]. Bloch equations were used to calculate a realistic profile based on the RF pulse of the proposed sequence [119, 120]. With this, LR slices were simulated.
To assess the influence of the slice profile accuracy on the SRR result, this profile was approximated using once a Gaussian and once a rectangular approximation. These slice profiles were approximated in such a way as to match the FWHM of the correct slice profile. The different results of the SRR using the different slice profiles were compared.
The effect of inaccuracies in the slice profile on the results of SRR was evaluated quantitatively by calculating and comparing the RMSE of the T_1 values in three different ROI in the septum, the apex, and the midventricular lateral part of the ventricle compared to ref_{XCAT}.

As already mentioned above, this evaluation was carried out using a simplified simulation of LR data, with SRR performed directly on the LR dynamics. Zero-mean noise was added.

4.3.4 Influence of motion on SRR

To investigate the influence of motion in between the LR stacks on the SRR result, different BH positions were simulated by translational shifts of the stacks. Different degrees of motion m were compared, while m described the maximum number of HR voxels the LR stacks were shifted to one another. For example, in the case of $m = 2$, the stacks were shifted to one another by a maximum of two voxels with respect to the reference state. So with $m = 2$, they were shifted, for example, by $+2$ or -2 HR voxel, so $+2*$ or $-2*$ (1.3 x 1.3 x 1.5) mm^3. Factors of m in the range of $[0, 4]$ were compared. Once, the motion was not corrected and once the motion was corrected by using the inverse of the simulated motion, simulating a perfect motion correction. For quantitative evaluation, the detectability of simulated fibrosis with a thickness of 6 mm was measured and compared.
As already mentioned above, this evaluation was carried out using a simplified simulation of LR data, with SRR performed directly on the LR dynamics. Zero-mean noise was added.

4.4 Results

To assess through-plane resolution, images in this publication are often presented orthogonally from the side, resulting in a 4CH view even though images were always acquired in SAX.

4.4.1 Model-based SRR

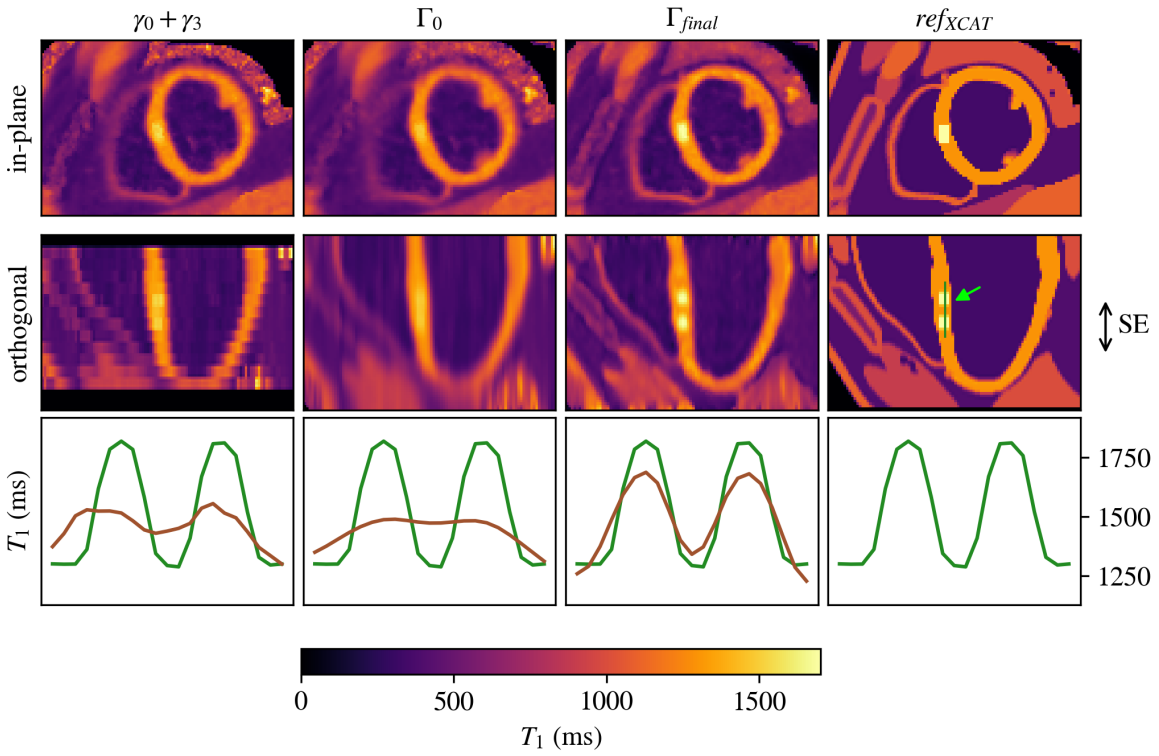

Figure 4.1: Model-based SRR applied on simulated data. The combination of the LR stacks γ_0 and γ_3, the SRR initialization Γ_0 and the result Γ_{final} are shown and compared to ref_{XCAT}. Cardiac motion was simulated and corrected. No BH motion was simulated. Two fibrotic structures with a thickness of each 6 mm and a gap in between of 6 mm were simulated (arrow). The line plot shows the T_1 values in the septum in SE direction in brown along the line, compared to the reference values in green.

Figure 4.1 shows the results of the numerical simulations assuming perfect BH positions and, therefore, no unknown motion in between the LR stacks. The two fibrotic structures could not be distinguished along the SE direction in the LR stacks. The apex was inaccurately depicted in Γ_0. Its visualisation improved after SRR. d of the fibrosis increased from 0.03 in Γ_0 to 4.38 in Γ_{final}, so increased from 0.38% of d in ref_{XCAT} in Γ_0 to 48.63% in Γ_{final}.

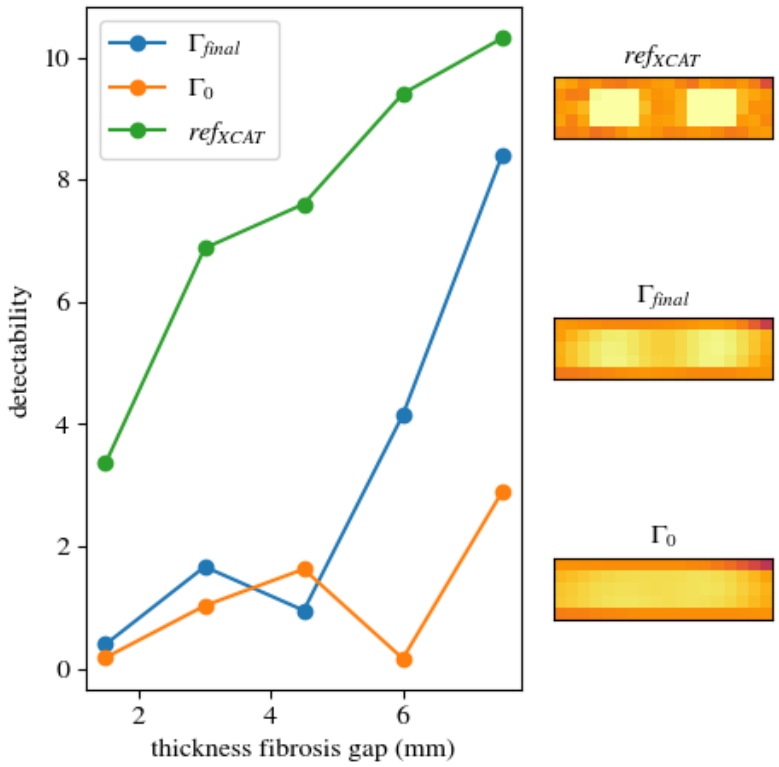

Figure 4.2: Influence of SRR on the visualisation of small structures for different thicknesses of fibrosis as well as a zoom-in for the visualisation of the fibrosis for a thickness of 6 mm.

As also shown in Figure 4.2, SRR could increase the detectability of small structures by $645.02 \pm 927.46\%$. While structures smaller than 4 mm could only partially be recovered, the visualisation of structures bigger than 4 mm improved using SRR.

4.4.2 Influence of slice profile accuracy on SRR

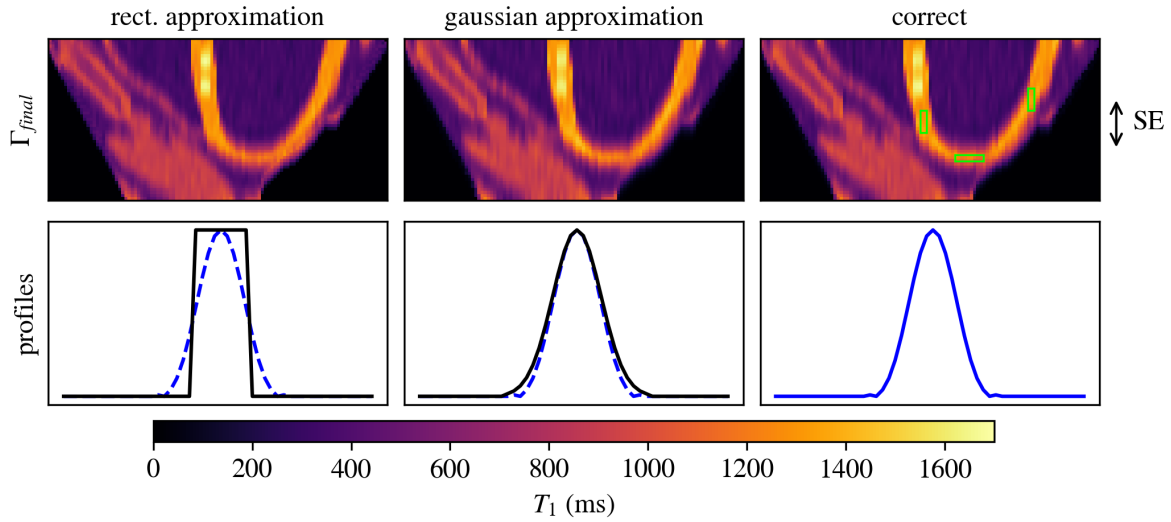

Figure 4.3: Influence of slice profile accuracy on SRR: The results of SRR using the correct slice profile (shown in blue) are compared to two SRR results using approximations (shown in black). The mean T_1 values in the green ROI are calculated for evaluation.

In Figure 4.3, Γ_{final} assuming different slice profiles for the SRR is shown. While the first row shows the SRR result, the second row shows the correct slice profile used for the simulation of the LR slices in blue and the profile used for the optimisation in black. The RMSE of the T_1 values of the ROI in Γ_{final} compared to ref_{XCAT} increased by 12.61% using the Gaussian approximated compared and by 23.39% when using a box-approximated profile.

4.4.3 Influence of motion on SRR

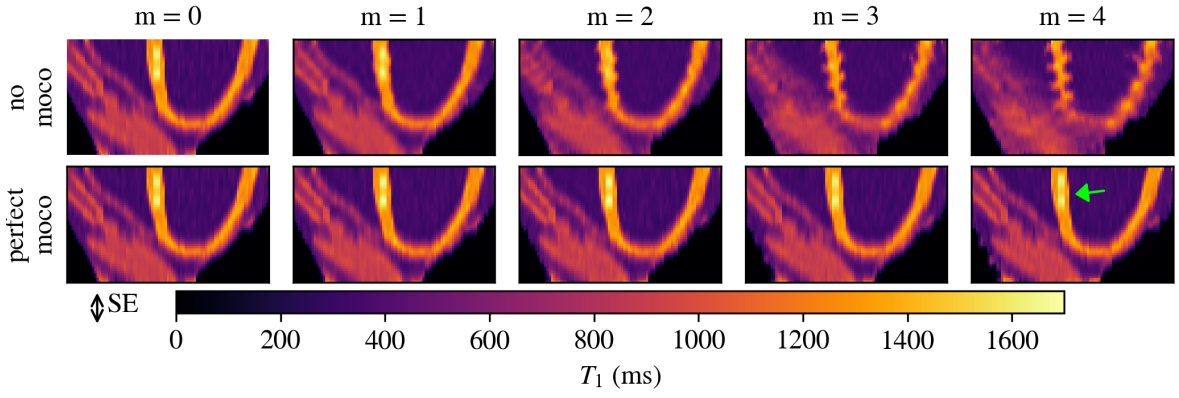

Figure 4.4: Influence of motion between the LR stacks on SRR. m describes the maximum number of HR voxels the LR stacks were shifted. Without any motion correction (moco), strong motion artefacts were visible. Using a perfect moco minor artefacts were still visible using a perfect moco, for example, at the simulated fibrosis (arrow).

Figure 4.4 shows the effect of motion in between the LR stacks on the SRR result. Uncorrected motion larger than one voxel strongly deteriorated the SRR result, while motion in the range of one voxel had only a minor effect.

When correcting the motion perfectly, still minor artefacts could be seen compared to no motion (see arrow). The detectability of fibrotic structures decreased by 15.73% for $m = 4$ compared to $m = 0$ when using a perfect motion correction.

4.5 Discussion

In this chapter, a model-based SRR scheme was presented for cardiac T_1 mapping and applied to simulated data. The proposed model-based SRR scheme improved the visibility of small structures. The detectibility of simulated fibrotic tissue increased by 645.02 ± 927.46% using the proposed SRR scheme. Furthermore, anatomic information, which was impaired in some LR stacks due to partial volume effects, for example, the apex, was successfully recovered by the proposed SRR approach.
Slice profile inaccuracies impaired the accuracy of the quantitative SRR result, which is in accordance with [115].
Accurate modelling of the acquisition geometry has shown to have a strong effect on the SRR result, while especially the knowledge about the LR stack positioning strongly affected the SRR result, which is in agreement with previous work on SRR in the brain [101]. Motion in between the LR stacks strongly impaired the SRR result, indicating a need for accurate motion estimation and correction for a successful SRR. The simulation of different BH positions was simplified by translational shifts of the overall image. However, realistic motion between BH positions might also lead to more complex motion and tissue deformation, which was not considered in this work.
Even perfect motion correction, however, impaired the performance of the SRR, as the motion between the stacks disturbs the original geometrical composition of the stacks. The stacks were planned such that they overlapped with each other by 1.5 mm. As each stack was obtained in a different BH position, the original distribution of stacks was impaired, even if the respiratory motion was correctly estimated and corrected. Hence, some HR positions were lacking information from the LR stacks, and for some HR positions, more than needed LR information was available.

4.6 Conclusion

In this chapter, a model-based SRR scheme was presented for cardiac T_1 mapping and successfully applied to simulated data, improving the visualisation of small structures. It could be shown that accurate modelling of the acquisition model is essential for accurate SRR results. Especially unknown motion between the LR stacks should be corrected, which will be further investigated in the following chapter.

5

In vivo application of SRR with residual breath hold motion correction

5.1 Introduction

In the previous chapter, SRR could successfully be applied to simulated data and improve the visualisation of small structures. However, the presented approach has not yet been applied to *in vivo* data, which is more challenging due to cardiac and respiratory motion.
The principle of SRR is based on knowledge about the geometric relationship between different LR datasets. As also shown experimentally in the previous chapter, motion, for example, due to different BH positions, can lead to misalignment between the different stacks and strongly impair the achievable image quality of SRR [64]. The application of SRR on the heart [95, 96, 93, 76, 78, 79, 97, 98] has so far only been shown for qualitative imaging. For T_1 mapping, SRR taking into account different motion states of the individual LR stacks has so far only been applied on the brain [88, 85, 84].
In this chapter, a motion-corrected model-based SRR for cardiac T_1 mapping is presented. Cardiac and residual respiratory motion was corrected. The motion correction approach was evaluated in native T_1 mapping in numerical simulations and phantom experiments, and feasibility was demonstrated in four healthy volunteers.

Parts of this chapter were published in J1.

5.2 Methods

5.2.1 Model-based cardiac SRR

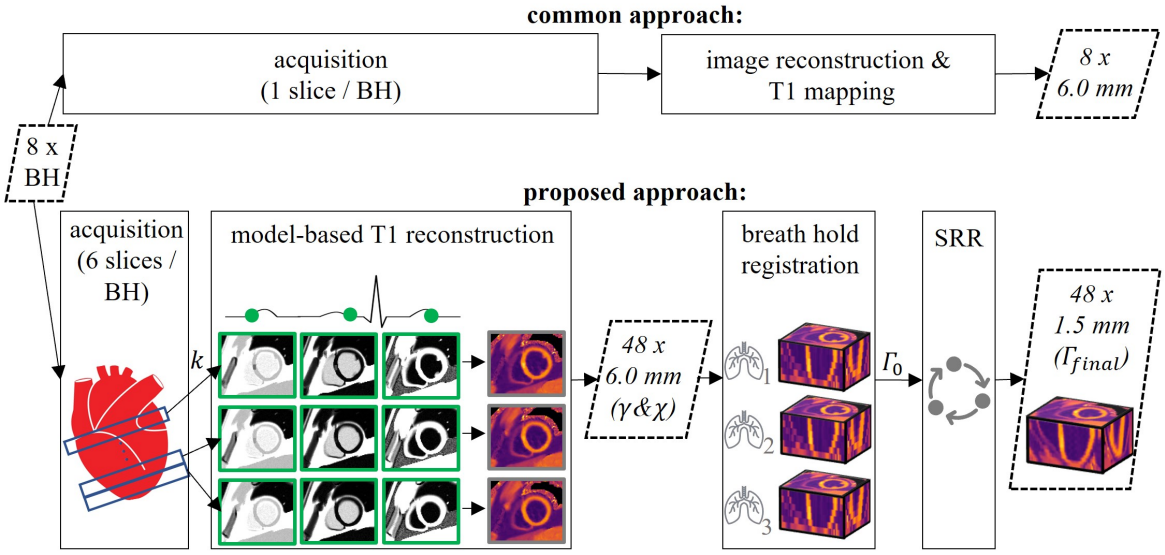

Figure 5.1: Comparison of the proposed motion-corrected model-based SRR workflow and the common approach. Data is acquired over eight BH in this schematic comparison. One slice can be reconstructed per BH in the common approach. In the proposed approach, one stack per BH with six 2D slices each are acquired. The cardiac motion is estimated and included in the model-based T_1 reconstruction of the k-space data k yielding the dynamics χ and the parameter maps γ of the LR stacks. Then, the different stacks are registered to each other. The motion-corrected γ are used to calculate the first estimate of the HR map Γ_0 and SRR yields the 3D HR map Γ_{final}. In this example, the proposed approach leads to six times more slices with the same number of BH, with a slice thickness reduced by a factor of four compared to the common approach. (source of parts: Shutterstock/Yeliena Brovko)

An overview of the proposed workflow for motion-corrected model-based SRR T_1 mapping is depicted in Figure 5.1: Multiple stacks of 2D slices are acquired continuously using a Golden radial angle trajectory with one stack per BH, as described in section 3.2. In the first step, the non-rigid cardiac motion is estimated and used in a model-based T_1 reconstruction (subsection 4.2.1) resulting in the dynamics χ and parameter maps γ (6 slices with a slice thickness of 6 to 8 mm per stack) which are all in the same cardiac motion state. In a second step, the stacks are registered to each other to compensate for different BH positions, as will be described in subsection 5.2.2. After the motion alignment, the maps are used to calculate the first estimate of the HR map Γ_0 as initialization of the SRR. Finally, a HR T_1 map Γ_{final} is generated by SRR, as described in subsection 4.2.1.

5.2.2 Breath hold registration

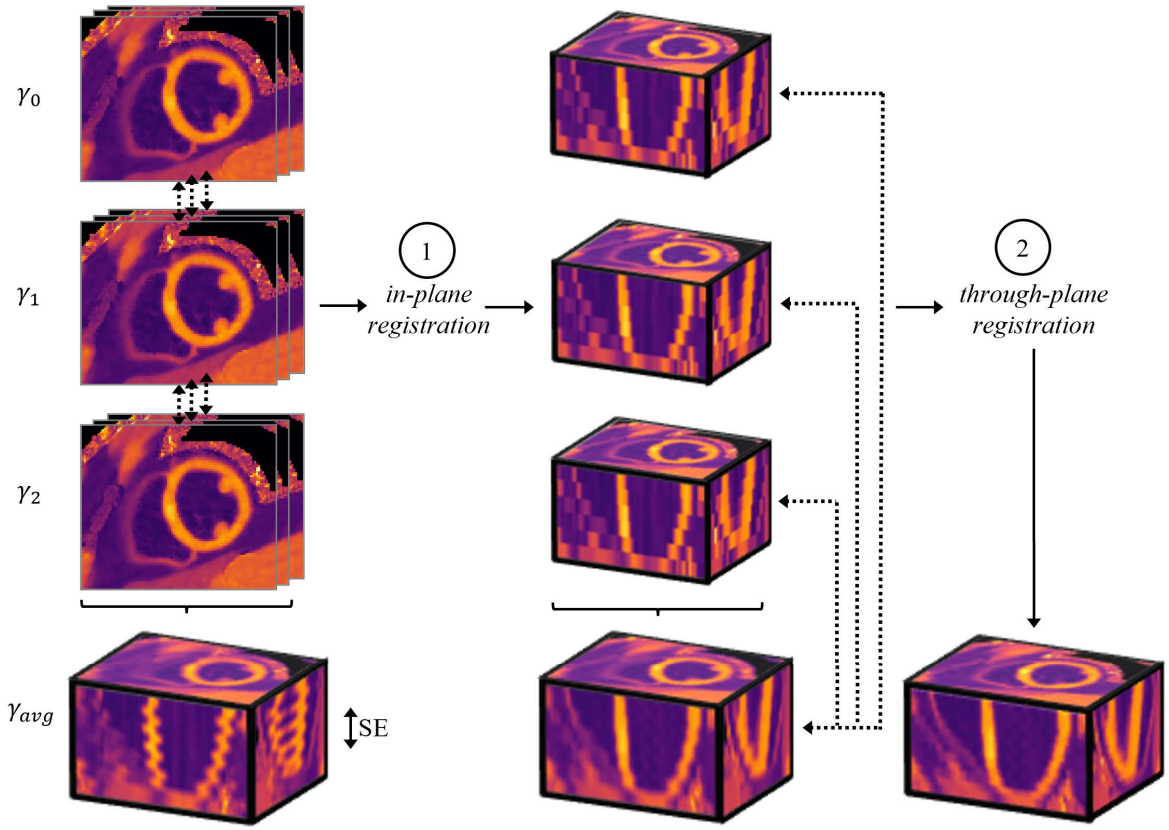

Figure 5.2: BH registration scheme. Different BH positions of the uncorrected T_1 maps of the individual LR stacks, three of which are shown as an example (γ_0,γ_1,γ_2), leads to artefacts when combining them in γ_{avg}. In the first step, each LR slice is registered to the closest slice in the neighbouring stack (in-plane registration), leading to a reduction of artefacts in the orthogonal view of γ_{avg}. In the subsequent through-plane registration, each LR stack is registered to γ_{avg} in an iterative fashion.

Each stack is acquired in a different BH. To correct for potential misalignments of BH positions, the stacks are registered to each other using a cross-correlation approach [121]. For this, a two-stage process was developed, as shown in Figure 5.2. In the first step of the motion estimation, the rigid motion in the in-plane directions of the LR slices γ_s of stack s is determined. For that, the T_1 maps of the LR slices are registered to each other: Each slice of each stack is registered to the slice which is closest (i.e. smallest distance along the SE direction) to it. The stacks are acquired in an overlapping fashion. Therefore, the closest slice is part of another stack, and hence, γ_s is registered to γ_{s-1} using a phase-cross-correlation registration [121]. That yields information about the in-plane motion of every slice of every stack. The median of the motion detected in its six slices is finally assigned to the entire stack of LR slices.
In the second step, the LR stacks are registered with respect to shifts along the SE direction. For that, γ_s are interpolated on a HR grid along the SE direction using bicubic spline interpolation, which also fills the gaps between the LR slices. The interpolated T_1 maps of the LR stacks are then combined, and an average stack γ_{avg} is calculated. In an iterative process, each stack is then registered to γ_{avg}. In the next iteration, a new γ_{avg} is calculated, considering the estimated motion. Only translational shifts are considered. Two iterations were used in total.

5.3 Experiments

5.3.1 Simulations

Simulated k-space data was generated as described in subsection 4.3.1.
Different BH positions were simulated by applying translation shifts. Twenty random configurations with different BH positions of the stacks were simulated. The simulated motion was in the range of (3.5, 1.9, 8.2) mm in the (anterior-posterior, right-left, food-head) direction, based on half of the motion range between end expiration and end inspiration measured in free-breathing experiments [122]. For reasons of computational time, no heart motion was included in this simulation.
To evaluate the accuracy of the alignment of the BH, the RMSE ϵ between the originally simulated motion and the estimated motion was calculated in mm.

5.3.2 Phantom

Phantom data was acquired as described in subsection 3.3.1. Eight LR stacks were acquired with 12 slices per stack to cover the whole phantom. The stacks were shifted to each other along the SE direction by 1.5 mm.
To evaluate the proposed approach in phantom measurements, next to the IR spin-echo reference ref_{IRSE}, a scan ref_{orth} orthogonal to the LR slices was acquired, where the SE direction of γ became an in-plane direction of ref_{orth}.
To assess the outcome of the SRR applied on the T1MES phantom, a ROI was drawn in every tube in γ, Γ_0, Γ_{final} and ref_{IRSE}. The mean and SD of the T_1 values were compared to assess T_1 accuracy and precision, respectively. The Pearson's correlation coefficient and the two-tailed P-value between γ, Γ_0, Γ_{final} and ref_{IRSE} were calculated.
To evaluate the outcome of the BH motion alignment, another dataset was acquired with phantom data at different, well-defined positions simulating different BH positions. The different positions were in the range (5.0, 2.4, 5.0) mm compared to the reference position. The reference motion was known for this acquisition, and the RMSE to the estimated motion was calculated.

5.3.3 *In vivo*

To evaluate the proposed approach in *in vivo* measurements, data was obtained from four healthy subjects (4 males, aged 34.0 $\pm$ 11.7 years) with a commercial 32-channel cardiac coil. All subjects gave written informed consent before participation in accordance with the institution's ethical committee.
Six to ten stacks (one stack per BH) with each six SAX slices were acquired in total with an offset of 1.5 to 2 mm between stacks along the SE direction. As discussed in subsection 3.3.3, a slice selective inversion pulse was used. The slice gap was subject-specific between 4 to 9 mm to cover the desired FOV while avoiding slice interference from the RF inversion and excitation pulses. The subject-specific spatial resolution was $1.3 \times 1.3 \times 6.0$ to 8.0 mm^3 with a FOV of $320 \times 320 \times 84$ to 105 mm^3. The ECG was recorded for retrospective cardiac motion correction.

Similar to the phantom data, an orthogonal scan ref_{orth} was acquired as a reference. Next to that, a 3(3)3(3)5 MOLLI scan ref_{MOLLI} was acquired with the following scan parameter: FOV: 360 × 306 mm^2, TE/TR: 1.12/2.7 ms, α: 35°, spatial resolution: 2.1 × 1.4 × 6 mm^3, orientation: 4CH. Accuracy of the T_1 values was evaluated by a comparison between the SRR result and the MOLLI reference using a ROI placed in the septum.
To assess the outcome of the SRR applied on *in vivo* data, ref_{orth} was qualitatively compared to Γ_{final}. The precision of the T_1 values was evaluated quantitatively by comparing the bull's eye plots [123] before and after the SRR, using four selected slices (apex, apical, mid-cavity and basal) and calculating the SD over four healthy volunteers.
No fibrotic tissue was present in the healthy volunteers, and therefore, the detectability of the right ventricle was calculated to assess the effect of SRR on small structures:

$$d = \frac{\mu_{structure} - \mu_{nextStructure}}{\sigma_{nextStructure}} \tag{5.1}$$

Where the mean T_1 value $\mu_{structure}$ was measured in a ROI within the right ventricle while the mean T_1 value $\mu_{nextStructure}$ and its SD $\sigma_{nextStructure}$ was calculated in a ROI next to the right ventricle.
The edge sharpness of the left ventricle in the anterior apical segment of the ventricle was calculated for γ, Γ_0 and Γ_{final}. The edge sharpness was calculated by manually drawing a line along the edge of interest and calculating an average edge profile perpendicular to this line. The first-order derivative of the edge profile was calculated, and edge sharpness of 100% referred to the case when the maximum derivative of the average edge profile was equal to the maximum intensity difference in the average edge profile, similar to previous work on coronary arteries [124].

5.4 Results

5.4.1 Simulations

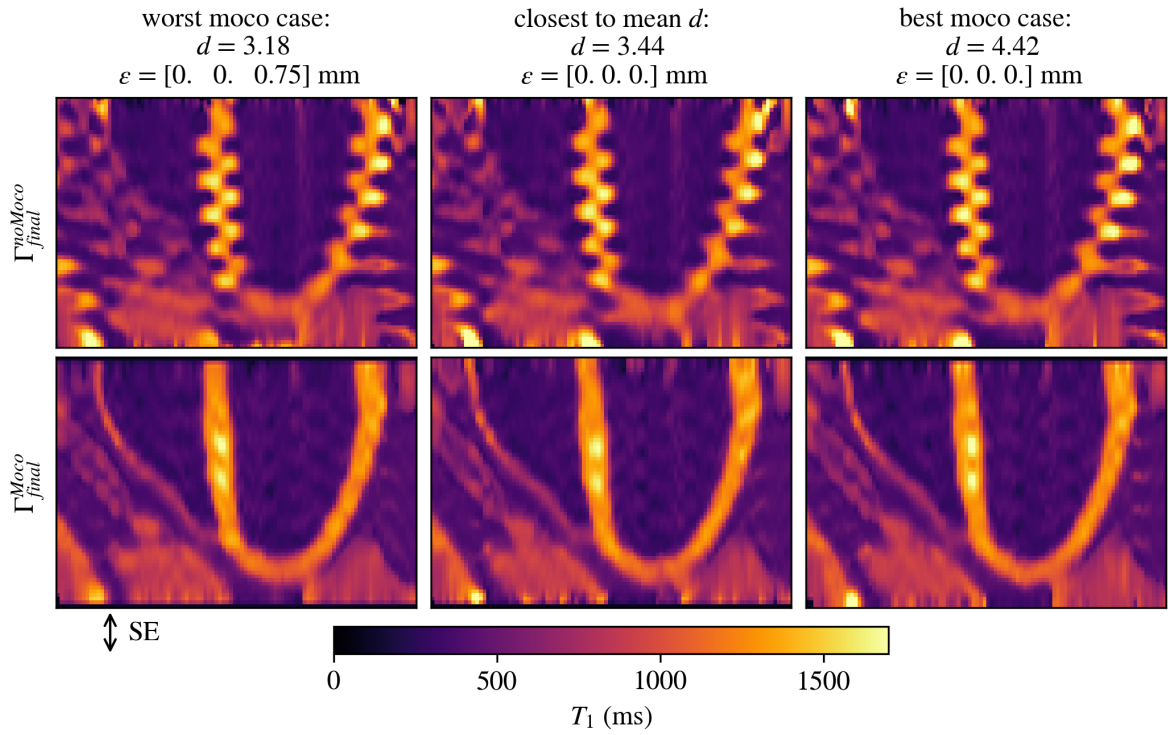

Figure 5.3: SRR applied to simulated data with stack specific BH states. The best and worst result of the motion correction (moco) out of 20 simulations is shown, measured by the moco error in mm (ϵ). The simulation with the detectability d closest to the mean d is shown in the middle column. The result of SRR without moco (Γ_{final}^{noMoco}) is compared to the result including moco (Γ_{final}^{Moco}).

Figure 5.3 shows the SRR applied on simulated data, simulated with different BH positions for every stack. Γ_{final} is shown without motion correction (Γ_{final}^{noMoco}) and with motion correction using the motion estimated with the proposed approach (Γ_{final}^{Moco}). The SRR results are shown once from the simulation with $\epsilon = 0$ (best case), with the largest ϵ (worst case) and once for the simulation with a d closest to the mean d of all simulations. Motion correction improved the outcome of the SRR. In the best motion correction case, the differentiation of healthy and pathological tissue was clearer compared to the worst motion correction case. After applying the calculated motion, d of the simulated fibrosis over all 20 simulations was 3.55 $\pm$ 0.54 in $\Gamma_{final,Moco}$. When applying the correct motion, known from the simulations, d was 3.62 $\pm$ 0.5. d in $\Gamma_{final,noMoco}$ was not calculated because the fibrosis could not be detected for these T_1 maps, as Figure 5.3 shows. The motion estimation error ϵ over all simulations was (0.0, 0.0, 0.18) $\pm$ (0.0, 0.0, 0.28) mm.

5.4.2 Phantom

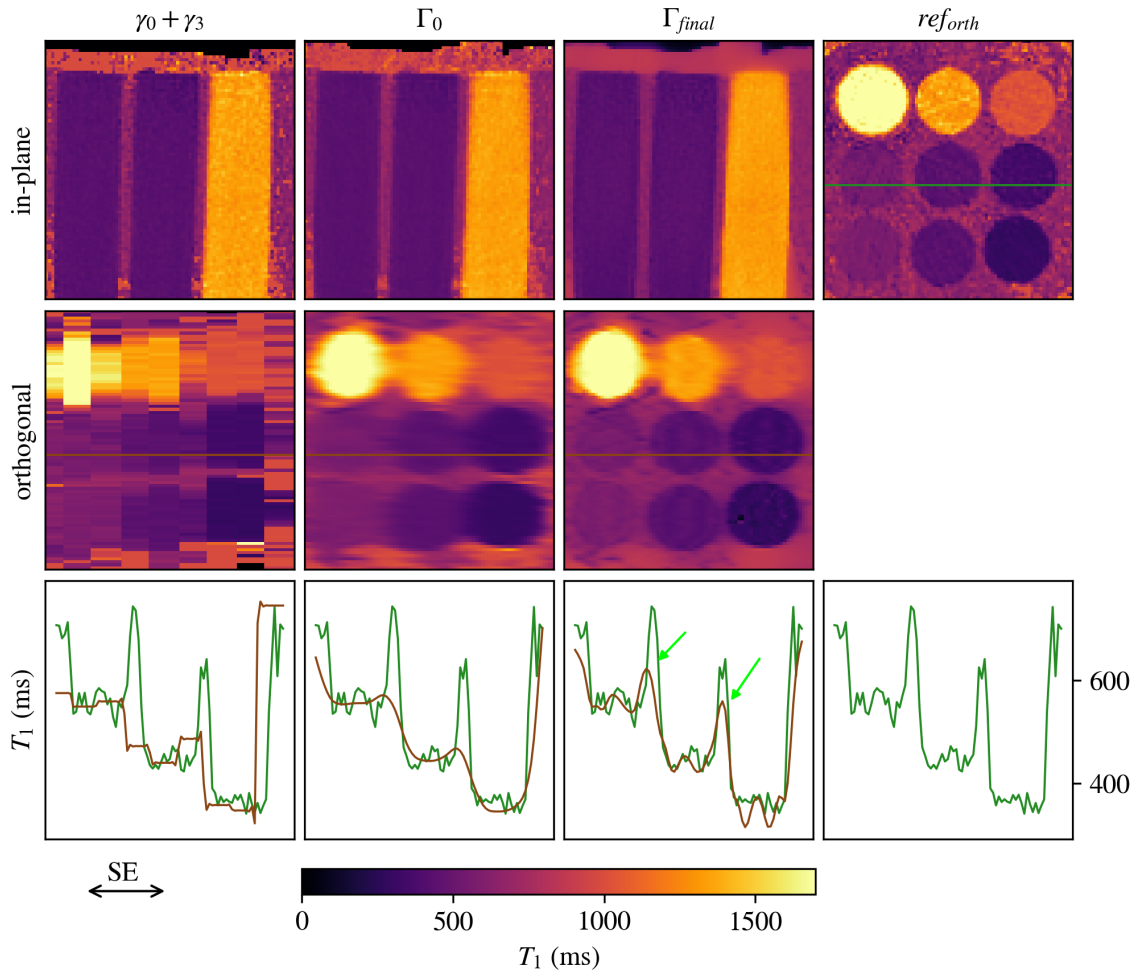

Figure 5.4: SRR applied on phantom data. The in-plane views and the orthogonal reformations of the combination of the LR stacks γ_0 and γ_3, Γ_0 and Γ_{final} are compared to ref_{orth}. A line plot through three tubes (brown line) along the SE direction shows an improved differentiation (arrows) between tubes and background after SRR as shown by the reference in green.

Figure 5.4 shows the in-plane view and the orthogonal reformation of γ, Γ_0 and Γ_{final} and compares it to an orthogonal acquisition ref_{orth}. A line plot through three tubes along the SE direction shows an improved differentiation between tubes and background after SRR.

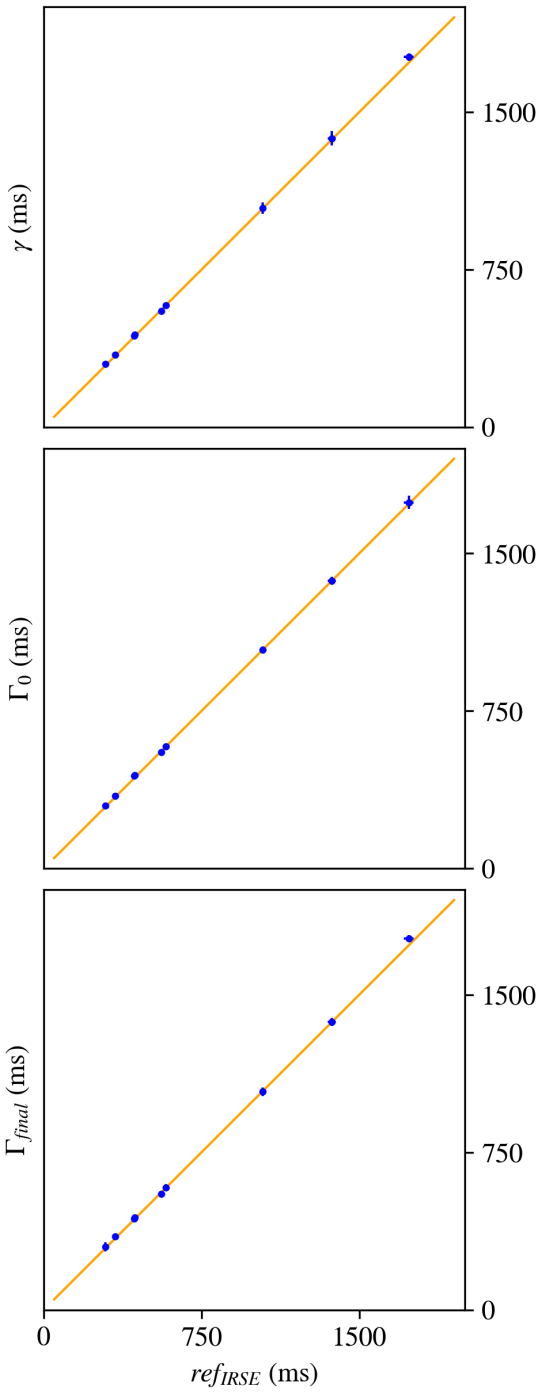

Figure 5.5: T_1 values obtained with an IR spin-echo reference ref_{IRSE} scan are compared to the combination of LR stacks γ, the initialization of SRR Γ_0 and the final SRR result Γ_{final}.

Figure 5.5 assesses the accuracy of SRR: γ, Γ_0 and Γ_{final} showed high correlation with ref_{IRSE} (P<0.001, R^2>0.999). The mean absolute difference between the T_1 values of ref_{IRSE} and Γ_{final} was 7.65 ± 9.24 ms. The mean absolute difference of γ and Γ_0 to ref_{IRSE} was 7.74 ± 7.09 ms and 5.41 ± 3.7 ms, respectively, indicating high T_1 accuracy.

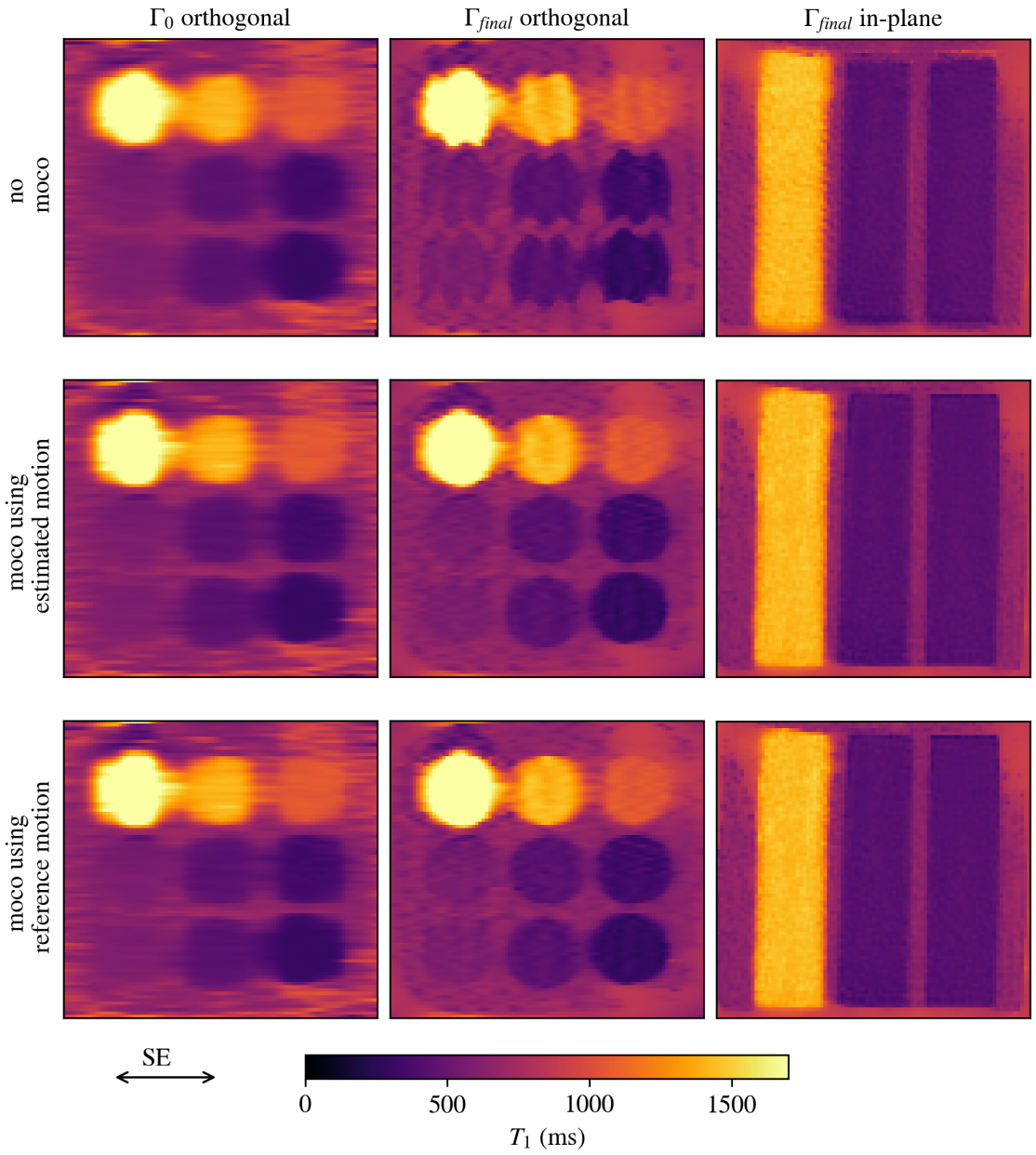

Figure 5.6: Simulated motion in the phantom experiment. The orthogonal view of the SRR initialization Γ_0, the final SRR output Γ_{final} as well as the in-plane view of Γ_{final} are shown when no motion correction (moco) was performed, when the estimated motion was applied and when the reference motion was used during moco.

Figure 5.6 shows the application of SRR on phantom data acquired at different simulated BH positions. The orthogonal view of Γ_0 and Γ_{final} and the in-plane view of Γ_{final} are shown without motion correction, when the estimated motion was applied and when the reference motion was applied during motion correction. SRR without motion correction shows motion artefacts that could be removed after applying the calculated motion correction. After applying the estimated motion shifts, the visual result is similar to applying the reference motion shifts during motion correction. The RMSE between estimated and reference motion was (0.03, 0.04, 0.61) mm.

5.4.3 *In vivo*

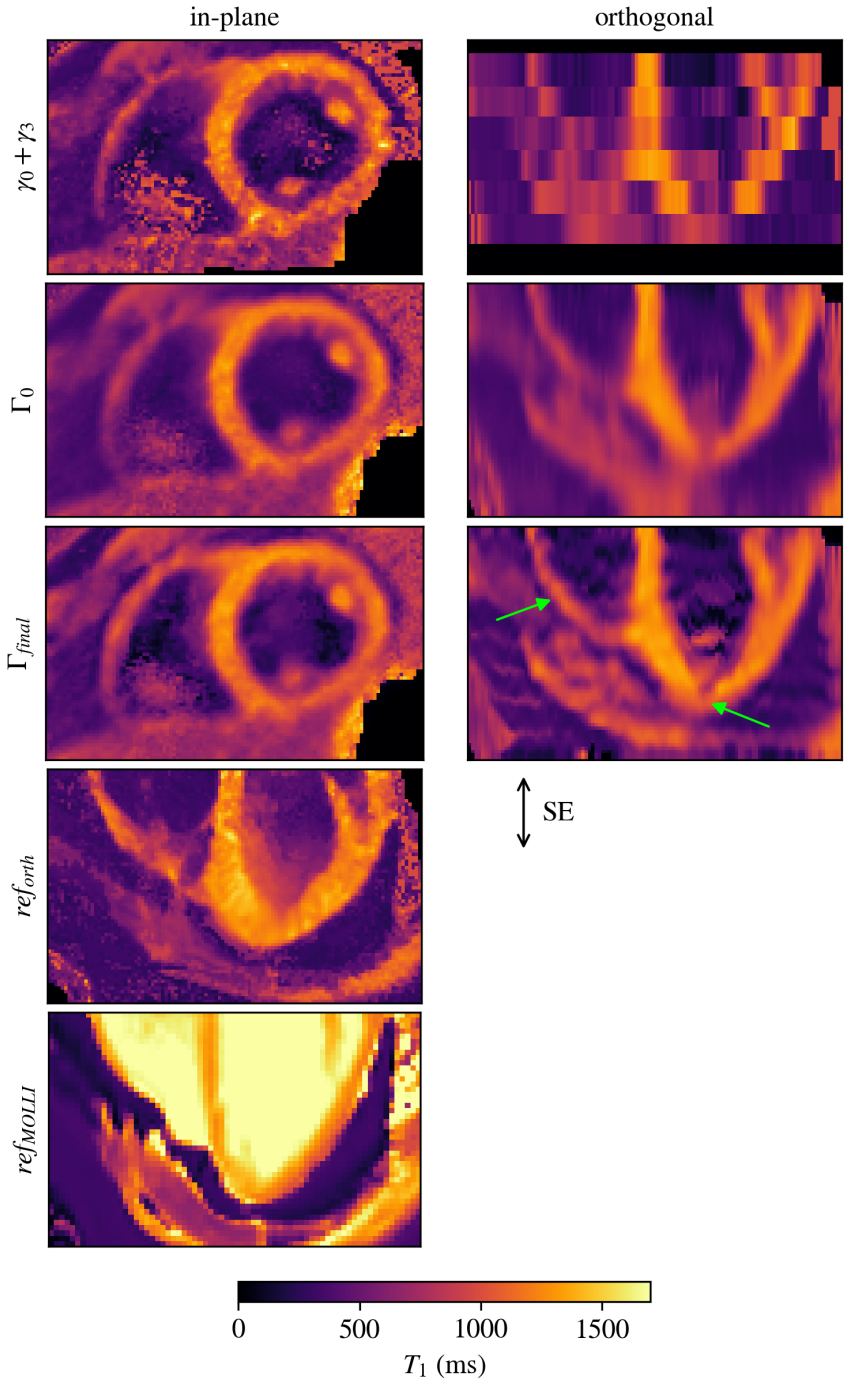

Figure 5.7: SRR applied on *in vivo* data. The combination of the LR stacks γ_0 and γ_3, Γ_0 and Γ_{final} are reformatted orthogonally and compared to ref_{orth} and to ref_{MOLLI}. All the results shown were obtained with the proposed motion correction approach. The visualisation of the apex and the right ventricle improved after SRR (arrows).

Figure 5.7 shows the in-plane view and the orthogonal reformation of γ, Γ_0, Γ_{final} and compares it to an orthogonal acquisition ref_{orth} and to ref_{MOLLI}. Due to the slice-selective inversion pulse, blood appeared with a low T_1 value. The visualisation of the apex and the differentiation between the right ventricle and blood improved after SRR. Due to scan time

limitations, ref_{orth} could not be acquired for one volunteer. The mean T_1 value across all volunteers in a ROI in the septum in Γ_{final} was 1211.49 ± 75.17 ms and in ref_{MOLLI} 1276.11 ± 38.77 ms. One volunteer had to be excluded from the calculation because no ref_{MOLLI} scan was available.

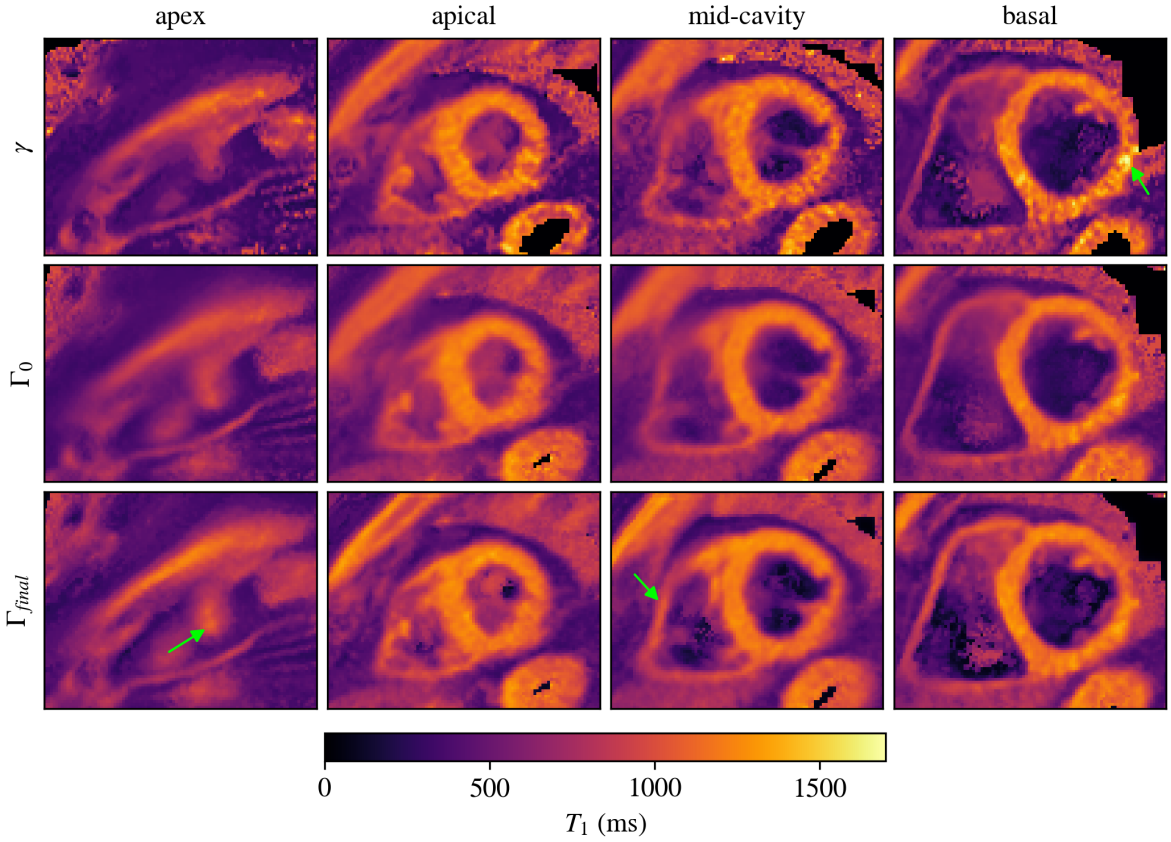

Figure 5.8: Four selected slices (apex, apical, mid-cavity and basal) before and after SRR. The visualisation of the apex and the right ventricle improved in the SRR result Γ_{final} compared to Γ_0 and a single LR stack γ (arrow in apex and mid-cavity slice). SRR reduced artefacts (arrow in basal slice). All the results shown were obtained with the proposed motion correction approach.

In Figure 5.8, four selected slices (apex, apical, mid-cavity and basal) of γ, Γ_0, Γ_{final} are compared in-plane. The apex was more clearly visible after SRR. The visualisation of the right ventricle improved after SRR. In addition, the combination of multiple LR slices in the SRR also reduced artefacts and improved, for example, the quantification of the inferolateral segment of the basal slice. d in the right ventricle increased from 2.4 ± 1.35 in γ, to 3.2 ± 1.63 in Γ_0 and 3.35 ±1.39 in Γ_{final}, thus an increase of d by 40% from γ to Γ_{final}. The edge sharpness in the anterior apical segment was 0.26 ± 0.04 in γ, 0.21 ± 0.02 in Γ_0 and 0.26 ± 0.04 in Γ_{final}. The sharpness of the ventricle was lower in the SRR initialization than in the LR slices, which could be attributed to the mixing of the partial volume effects in the individual LR slices when combining them for the initialization. SRR was able to restore the original edge sharpness of the LR slices. T_1 maps of two more volunteers can be seen in Figure 5.9.

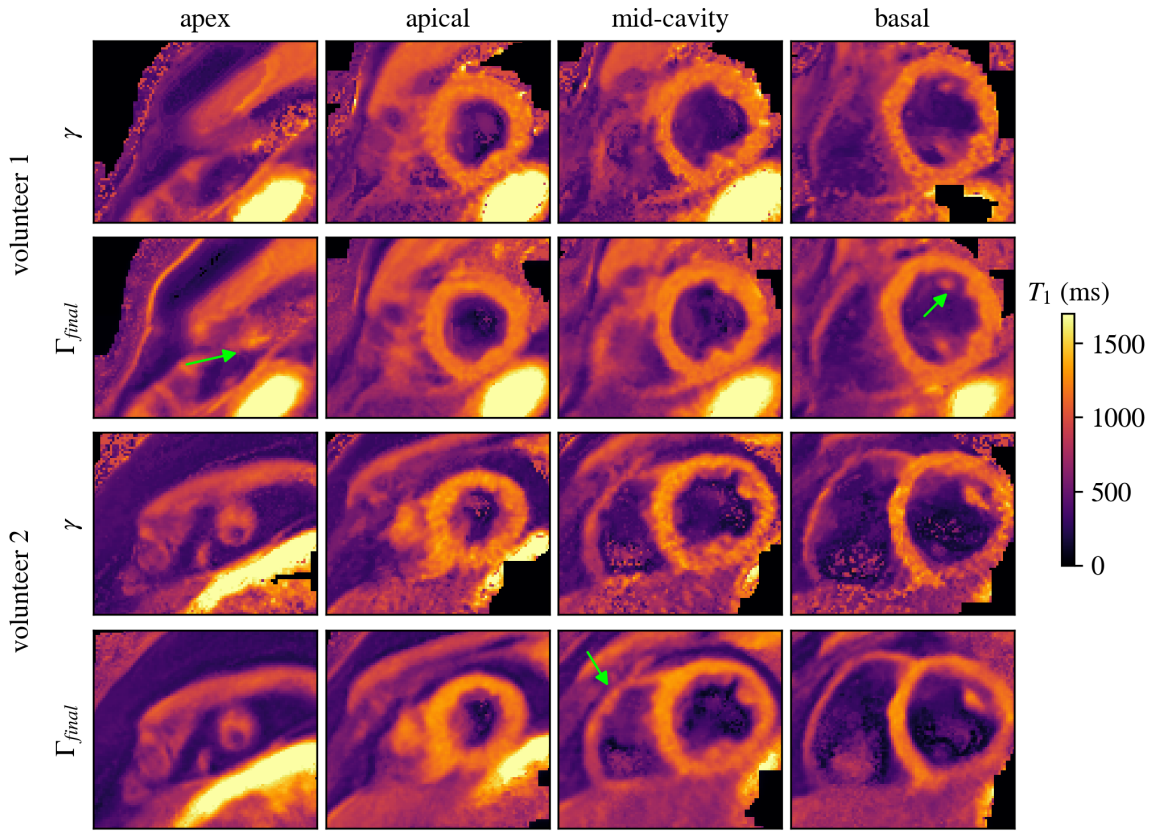

Figure 5.9: Four selected slices (apex, apical, mid-cavity and basal) before and after SRR for two more volunteers, as a complement to Figure 5.8. The visualisation of the apex, the papillary muscle and the right ventricle improved in the SRR result Γ_{final} compared to a single LR stack γ (arrows). All the results shown were obtained with the proposed motion correction approach.

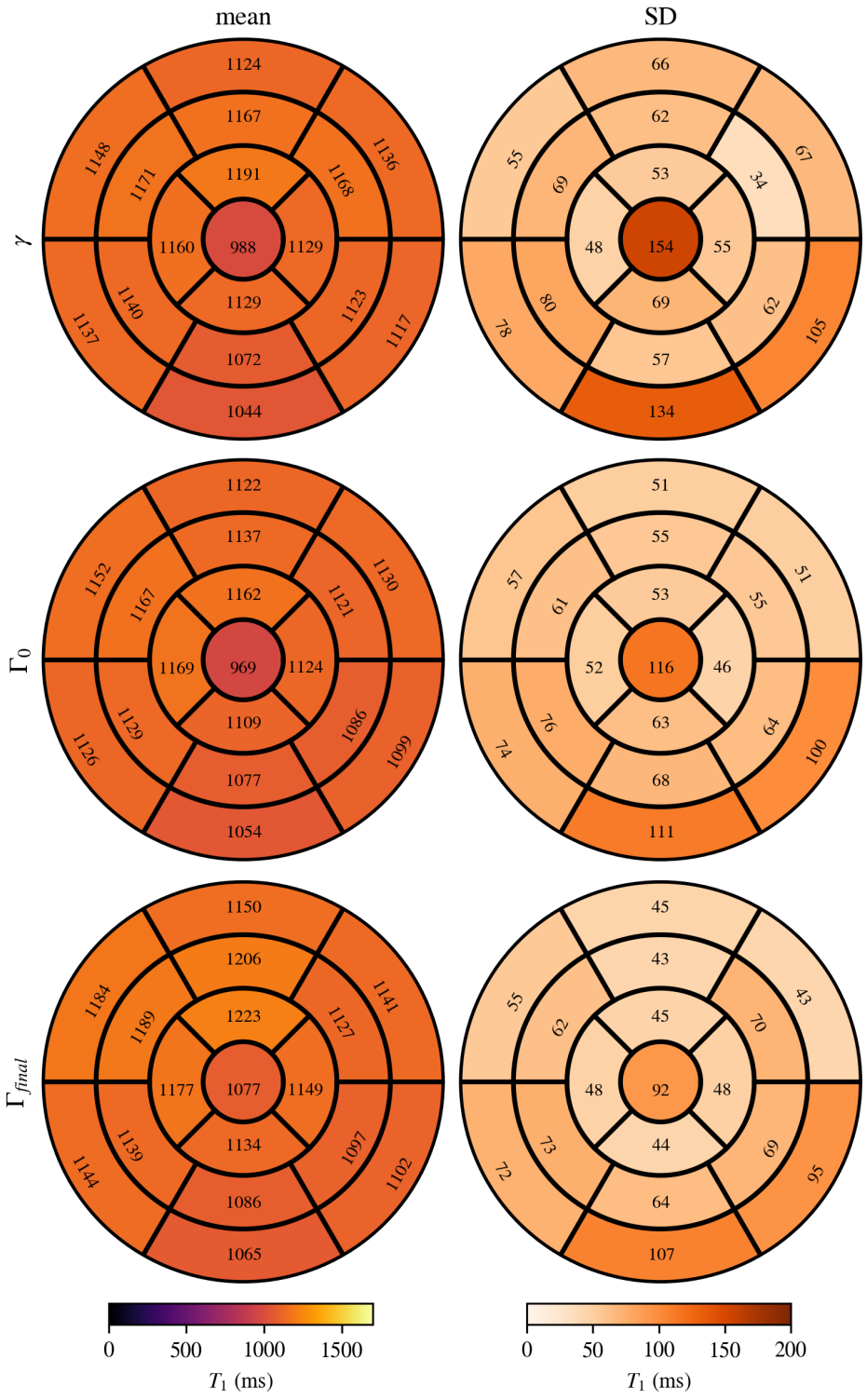

Figure 5.10: Bull's eye plots of the average T_1 values in ms in standardized segments of the left ventricle and their SD.

Figure 5.10 shows the bulls-eye plots of γ, Γ_0 and Γ_{final}, averaged over four healthy volunteers. The SD before and after the SRR remained comparable, indicating that SRR did not affect the precision of the T_1 values. The T_1 values in the segments varied in Γ_{final} by an average of 63.72 ms across the four healthy volunteers. The T_1 intensities of the apical segment were underestimated before the SRR and showed a high SD. This was corrected by SRR.

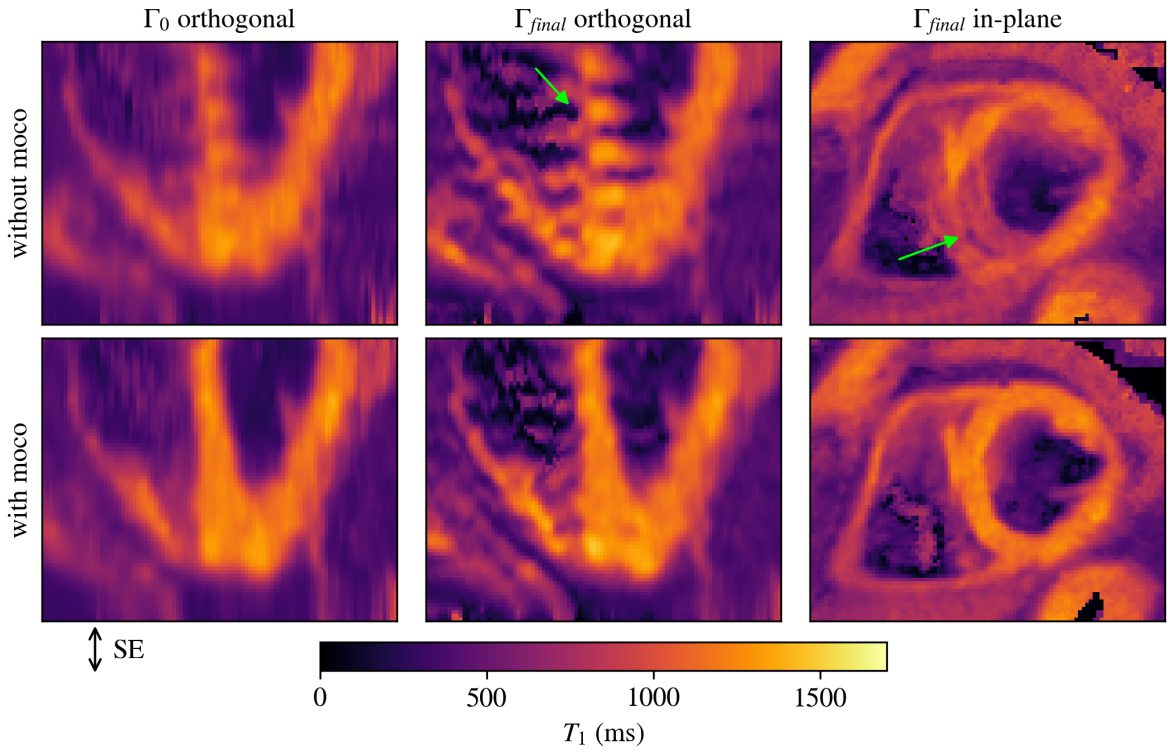

Figure 5.11: Impact of respiratory motion correction (moco) on *in vivo* data. The orthogonal view of Γ_0, Γ_{final}, as well as the in-plane view of Γ_{final} are shown without and with moco.

Figure 5.11 compares the orthogonal view of Γ_0 and Γ_{final} and the in-plane view of Γ_{final} with and without motion correction. Without BH alignment, motion artefacts could be seen as a discontinuous septum in the orthogonal view and an ambiguous delineation of the myocardium in the in-plane view, highlighted by the arrows in the figure. The motion artefacts were less visible in the initialization of the SRR compared to its output. The motion artefacts could be reduced after the proposed BH registration and subsequent correction.

5.5 Discussion

In this study, a respiratory BH motion correction was proposed. A motion-corrected model-based SRR approach was applied on phantom, and *in vivo* data, providing a 3D HR T_1 map in six to ten 17-second breath holds. Matching the results from the simulations in subsection 4.4.1, the proposed model-based SRR scheme improved the visibility of small structures while the accuracy and precision of the T_1 values after SRR remained comparably high.

The visualisation of small structures as the differentiation between phantom tubes and background or the right ventricle could be improved using SRR. Furthermore, anatomic information, which was impaired in some LR stacks due to partial volume effects, for example, the apex, was successfully recovered by the proposed SRR approach.

The accurate mapping of the right ventricular myocardium poses a great challenge due to its small thickness but would help to improve the diagnosis of, for example, right ventricular myocarditis or arrhythmogenic right ventricular cardiomyopathy. Its assessment could be improved by SRR, moving towards whole heart T_1 mapping in the future.

A general improvement in the imaging of small features by SRR can be concluded from the

improved visualisation of small structures in all volunteers of the *in vivo* experiments, such as in the right ventricle.

Every stack was acquired in a separate BH. Due to variations in BH positions, an alignment of different BH states was necessary before SRR. In agreement with [64] and the results from subsection 4.4.3, motion estimation was a key step in the SRR process and significantly affected the quality of the SRR result. Motion correction imperfections led to artefacts in the SRR reconstruction. An alignment of different BH states showed great improvement in the SRR result.

Compared to brain T_1 mapping, cardiac imaging is restricted with respect to the number of LR slices per stack due to limited BH time. To still cover a specific FOV in the SE direction, gaps needed to be introduced between the LR slices. More stacks of LR slices needed to be acquired to compensate for these gaps. According to [80], the more stacks used, the greater the degrading influence of inaccuracies in the motion registration on the SRR. Due to this restriction, the FOV of the presented approach was limited to the ventricles. In the case of focal pathologies, however, there is a clinical need for whole heart T_1 mapping techniques [15]. As described in chapter 6, this could be achieved by acquiring the LR stacks in the long-axis orientation and by also rotating the LR stacks differently to one another instead of shifting them. Furthermore, with that, the SRR result would be more robust with respect to residual motion in between the LR stacks [101].

In clinical practice, 17 seconds BH are sometimes not feasible. To adapt the BH duration, the acquisition time per stack would need to be reduced and compensated for by acquiring more stacks in total. Due to the higher number of stacks, the proposed motion correction approach would have an even greater influence on the SRR result.

The results were compared to a clinical reference scan, and the T_1 values after SRR were in good agreement with both the reference values resulting from the MOLLI reference scan and those presented in literature [125]. The small underestimation of 2.09% of the myocardial T_1 values after the SRR compared to reference values was probably due to the use of a slice-selective inversion pulse. A similar underestimation of the T_1 values was reported in [126], which was attributed to magnetization transfer effects. However, a direct comparison of the SRR results to an *in vivo* reference scan was difficult since this was acquired in another BH, showing a different motion state. Thus, the accuracy of the T_1 values could only be determined in phantom measurement but not in the volunteer scans.

The precision of the T_1 values was not calculated with a retest but as the SD over several healthy volunteers. It was assumed that the T_1 values of the myocardium were similar in all healthy volunteers.

One limitation of this approach is that T_1 values of voxels representing blood could not be estimated and appeared shortened due to the in-flow effect caused by the slice-selective inversion pulse. To still be able to calculate the ECV, a further fast acquisition of a single LR slice with a global inversion pulse would provide the necessary information about the blood pool T_1 values.

To improve the overall result of the SRR in future approaches, the SRR optimization scheme could be integrated into a model-based reconstruction framework as performed in [94] and will be further investigated in chapter 7. By that, the SRR is going to incorporate the acquired

raw data in the entire reconstruction optimization scheme instead of using it only in the model-based T_1 reconstruction as in the presented approach.
This work was only evaluated in healthy volunteers. Nevertheless, from the improved visualisation of pathologies in the simulated data in subsection 4.4.1, it can be concluded that SRR might lead to improved image quality in patients as well.

5.6 Conclusion

In this chapter, a motion-corrected cardiac model-based SRR approach was presented, providing a 3D HR T_1 map of the ventricles in six to ten 17 seconds BH. Cardiac motion and motion in between different BH states could be corrected. The proposed approach was successfully applied in four healthy volunteers, leading to improved visualisation of small structures and precise T_1 values. Nonetheless, the imaging FOV was still limited to the ventricles, which could be improved by using a radial SRR geometry with long-axis LR stacks, as presented in the next chapter.

6

Whole heart T_1 mapping with rotated stacks

6.1 Introduction

In the previous chapter, 3D HR T_1 maps of the ventricles could be obtained using cardiac motion-corrected SRR with SAX stacks, which were shifted to each other by a sub voxel shift along the SE direction. For focal cardiomyopathies, however, there is a clinical need for whole heart T_1 mapping techniques that can provide a thorough evaluation of the complex regional distribution patterns of the disease [15]. In these cases, it is important to examine the regional characteristics of the myocardial tissue to understand the underlying causes of the disease.
Previous studies in the brain have shown that the visualisation of small structures with SRR improves with rotating the single LR stacks differently compared to translating them, in the sense of the least error to the reference. Furthermore, SRR using rotated stacks is more robust with respect to slice profile inaccuracies assumed during reconstruction compared to translated stacks [115]. Previous studies for the brain [115] have shown that the more stacks, i.e. orientations used for the SRR, the better the result in the sense of the least mean squared error to the reference. For cardiac imaging, however, the number of LR slices per stack and the total number of stacks are limited by BH duration and overall acquisition time. Therefore, the rotated SRR geometry needs to be adapted for cardiac applications.
For coverage of the whole heart using multiple LR stacks, fewer images are needed when acquiring the LR images in long-axis orientation compared to SAX due to the geometry of the heart [127]. This has been used for cine MRI [40, 127] or perfusion [128] approaches using slices at different radial long-axis orientations for obtaining volumetric data. So, the overall acquisition time for a whole heart coverage can be reduced by acquiring 4CH or 2CH slices instead of SAX ones.
The relationship between blood flow and the SE direction is, however, more complex in the long axis compared to the SAX: While in the SAX, blood is mainly flowing through the slice [129, 130], blood is moving within the slice [127] in the long axis slice. The ejection fraction

is normally below 72% for men and 74% for women [131]. So when using a slice-selective inversion pulse, inverted blood is mixed at some point during the acquisition with blood that has not been inverted. Especially blood in the apical region does not necessarily get ejected, so this effect is strongly visible there. A similar effect in the apical region has been reported for spin echo sequences [132].
The T_1 value of partially inverted blood can be close to the one of healthy myocardium, making it challenging to distinguish myocardium from blood in this region. This effect depends, on the one hand, on the cardiac blood flow dynamics of each subject but also on the thickness of the slice-selective inversion pulse. Depending on this thickness, more or less inverted blood is available; hence, the mixing ratio of inverted and non-inverted blood changes.

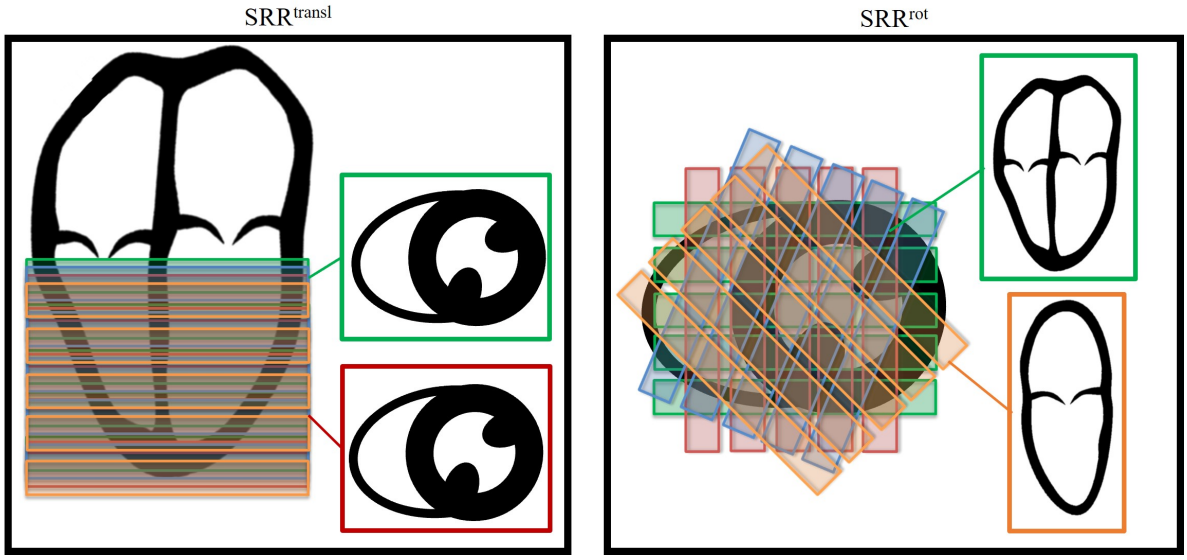

Figure 6.1: Illustrative comparison between the previously used SRR geometry using translated SAX stacks (SRR^{transl}) and one using rotated long-axis stacks (SRR^{rot}) (source of parts: Shutterstock/Noonnin)

In this chapter, a whole heart SRR approach is introduced, acquiring rotated long-axis LR stacks going from the 4CH to the 2CH orientation by placing the rotation axis along the septum, as shown in Figure 6.1. For that, several multi-slice long-axis stacks with high in-plane but low through-plane resolution are acquired. In this chapter, the acquisition scheme of the LR stacks is adapted to provide accurate T_1 estimates. The radial SRR geometry provides radially overlapping LR stacks of the object, from which a HR volume is reconstructed. This acquisition scheme ensures that the stacks overlap and provide information about the complete heart, especially along the LR stack direction. So, in this chapter, the radial SRR geometry will be adapted to cardiac imaging.
The proposed approach will be evaluated in simulations and phantom experiments.

Parts of this chapter have been submitted for publication in J2.

6.2 Methods

In this chapter, SRR acquiring LR stacks in the long-axis orientation is introduced. For that, the model-based T_1 reconstruction is adapted. Next to that, a radial SRR acquisition geometry is introduced. With that, the LR stacks are rotated to one another instead of shifted. A motion estimation and correction scheme, aligning different positions of the LR stacks as, for example, in the case of different BH positions, is presented.

6.2.1 Model-based T_1 reconstruction

The parameter maps are reconstructed as described in subsection 3.2.2. Compared to the SAX, the anatomy and motion of the long-axis orientation are more complex, covering both atrial and ventricular contraction. Therefore, 60% of the ventricular systole is removed prior to the SRR reconstruction.

6.2.2 Radial SRR acquisition

For SRR, several radial LR stacks are acquired. The stacks have the same positions but are rotated around the PE direction. The septum is aligned parallel to PE, so the stacks are rotated from a 4CH to a 2CH and back to a 4CH. Every stack is acquired in a separate BH. As nomenclature, in the following, the superscript describes the geometry of the SRR acquisition (*rot* for rotated or *transl* for translated).
The formulation and way of solving the optimisation problem of the SRR stay the same as introduced in subsection 4.2.1:

$$\min_{\Gamma} \sum_{t=1}^{N_T} \sum_{s=1}^{N_S} ||\chi_{t,s} - A_s * q_t(\Gamma)||_2^2 + \kappa \|G * \Gamma||_1 \tag{6.1}$$

However, the stack-specific acquisition geometry parameter A_s of stack s changed, from shifting the LR stacks differently to one another to rotating them.

6.2.3 Motion estimation and correction

The cardiac motion is estimated using the MIRTK Toolkit [105] as described in subsection 3.2.1 with a temporal resolution of 57 ms.
As each LR stack is acquired in a different BH, translational motion correction is applied to correct for potential misalignment between the BH positions. For that, the LR T_1 maps are interpolated onto a HR grid using A^T. All LR stacks are combined into an average stack, and every stack is registered to this average using a masked cross-correlation approach [121]. Three iterations are used in total.

6.3 Experiments

6.3.1 Data acquisition

Data was acquired using the scanning parameters described in subsection 3.3.1. For SRR, 12 LR stacks were acquired. The number of slices per stack was decreased from six to five slices to

shorten the BH length to approximately 14 seconds, as discussed in section 5.5. To cover the whole heart with each LR stack, gaps of 14 mm were introduced in between the LR slices. The SRR results were reconstructed to an isotropic high resolution of 1.3 mm. When the results from SRR^{rot} were compared to the results from SRR^{transl}, the LR stacks for SRR^{transl} were shifted to one another by 1.3 mm to match the isotropic resolution.

6.3.2 Minimisation of blood-flow artefacts

The geometry of the myocardium in the long-axis orientation is very different to the SAX. The model-based T_1 reconstruction as proposed in [54, 55, 53] was, however, optimised for SAX imaging. Hence, in this chapter, the acquisition of long-axis oriented LR slices is optimised to provide accurate T_1 values.
For this, data from a healthy volunteer was acquired in 4CH orientation with different slice thickness Δz in the range from [4, 5, 6] mm leading to a thickness of the inversion pulse of [12, 15, 18] mm. A flip angle $\alpha = 9°$ was used. The acquired k-space data was reconstructed using a non-uniform FFT [109, 110] to avoid regularisation effects of the model-based reconstruction. The images were reconstructed without cardiac motion correction, and the whole systole was excluded from reconstruction to avoid any influence of the cardiac motion correction on the results.
The accuracy of the T_1 values in the long axis was evaluated qualitatively and quantitatively. The T_1 values along a line through the apical region in the 4CH orientation for different Δz were plotted and compared for qualitative evaluation. For quantitative evaluation, a reference T_1 value $T_1^{blood,ref}$ of blood was calculated as the mean T_1 value in a basal ROI in the blood. For each Δz the mean T_1 value of the blood in an apical ROI was calculated and compared to $T_1^{blood,ref}$.

6.3.3 Optimal flip angle for maximum SNR

As mentioned in the previous chapter, a reduction in Δz leads to a reduction of SNR. This could be counteracted by an adaption of the flip angle α. In this chapter, α was optimised with respect to maximise the SNR. For that, phantom scans were performed with one slice per stack, $\Delta z = 4$ mm and α between 2 and 18°.
The SNR was calculated per phantom tube, as proposed in chapter subsection 3.3.2. Next to that, the RMSE of the fitted T_1 values within ROIs of the phantom tubes were calculated.

6.3.4 Optimize SRR^{rot} for cardiac applications

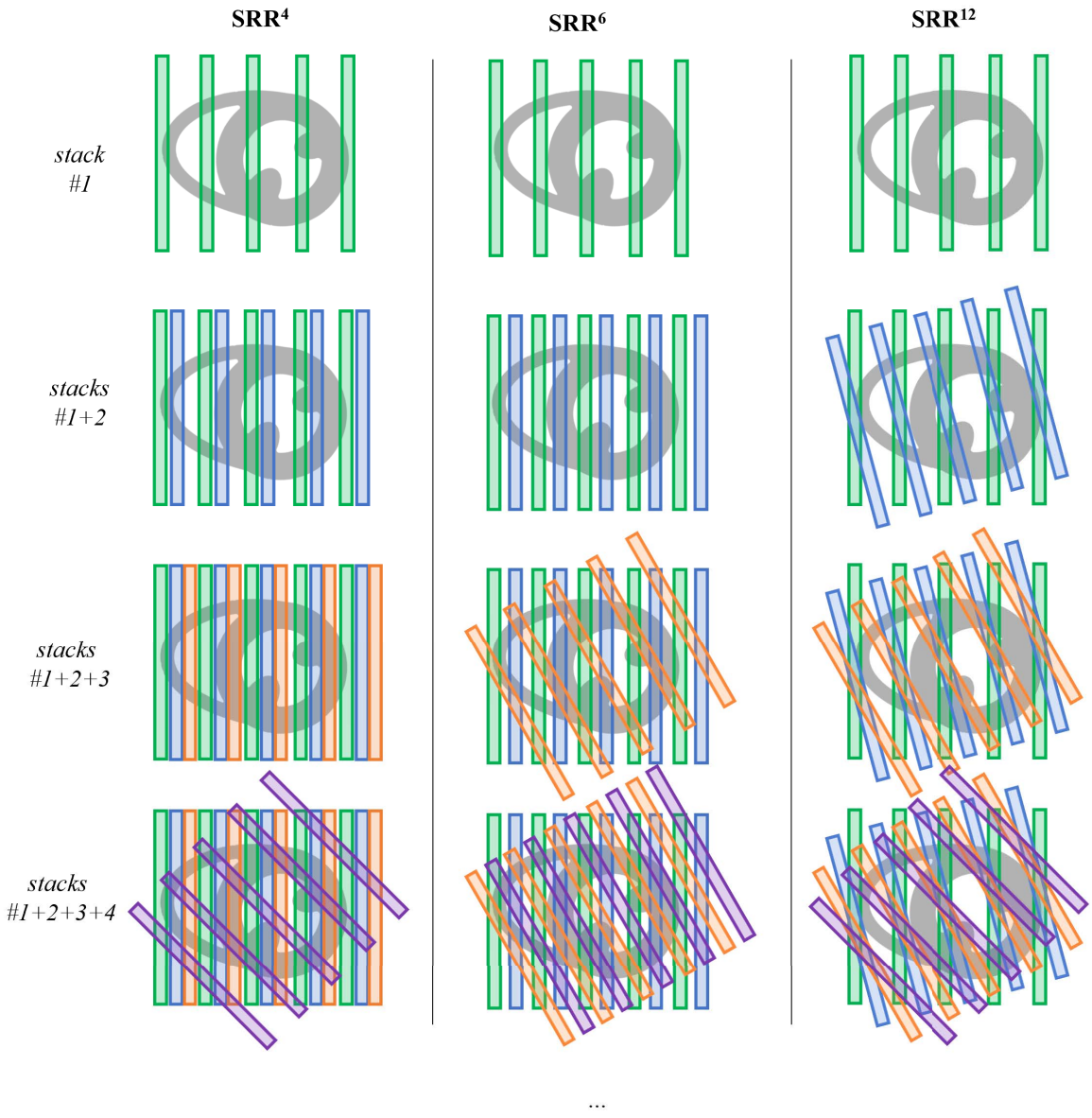

Figure 6.2: Illustration of different SRR^{rot} geometries. While each column represents a different geometry, with each row, one more of the overall 12 stacks is shown

In this chapter, three different acquisition geometries with different orientations and positions of the LR stacks were compared:

- SRR^4: 4 orientations (0, 45, 90, 135)° and three stacks per orientation
- SRR^6: 6 orientations (0, 30, 60, 90, 120, 150)° and two stacks per orientation
- SRR^{12}: 12 orientations (0, 15, 30, 45, 60, 75, 90, 120, 135, 150, 165)°

Each of the geometries used 12 stacks in total, but some used several stacks per orientation and used them for filling the gaps in between the LR slices as shown in Figure 6.2.

The effect of the different geometries on the SRR result was investigated by applying the motion-corrected model-based SRR proposed in chapter subsection 4.2.1 to the LR stacks of simulated and phantom data. Simulated and phantom data was acquired as described in subsection 3.3.1. For both, 12 stacks consisting of five parallel slices each were acquired with the following parameters: $\Delta z = 4$ mm, $\alpha = 9°$. Different stacks within one orientation were placed such that they filled the gaps of the other stack equidistantly, so the offset between the stacks for SRR^4 was 6 mm and for SRR^6 4.5 mm.
To separate the effect of the different SRR geometries from any inaccuracies due to incomplete cardiac motion correction and the model-based T_1 reconstruction, this evaluation was carried out using a simplified simulation of the LR XCAT data, with SRR performed directly on the LR dynamics. Furthermore, no BH motion correction was performed. No noise was added.
For evaluation, the weight distribution of the different slices was calculated. This distribution shows the amount of LR information per HR position, so regions where LR slices overlapped lead to high information and hence appear bright in the weight distribution. Areas where no information was obtained with any LR slice appear dark in the weight distribution.

6.3.5 Numerical simulations and phantom experiments using SRR^{rot}

In this chapter, the SRR^{rot} approach, optimised for cardiac applications based on the experiments described in the previous subsection, is further investigated in simulation and phantom experiments. For both, 12 stacks consisting of five parallel slices each were acquired with the following parameters: orientations: (0, 45, 90, 135)°, three stacks per orientation shifted by 6 mm to each other, $\Delta z = 4$ mm, and $\alpha = 9°$.
For the XCAT data, two different simulations were carried out: once only cardiac motion was simulated and corrected, but not BH motion was simulated, and once no cardiac but BH motion was simulated. Different BH positions were simulated by translational shifts in the range of (5.2, 10.4, 10.4) mm. The range refers to the HR coordinate system, with the first number indicating the long axis of the myocardium and the two others indicating the short axes. The simulated motion range was assumed to be half of the amplitude motion between end expiration and end inspiration as reported in [122].
The performance of the BH motion alignment was evaluated by calculating the RMSE to the known simulated motion in mm. The reduction in RMSE compared to the maximum possible RMSE was calculated as the mean RMSE over the three spatial directions. For that, the simulated dataset with no cardiac motion was used as the performance of cardiac motion correction could influence the performance of the BH motion correction.
For the phantom experiments, data was acquired using a continuous Golden radial acquisition scheme as described previously. A reference scan ref_{orth} orthogonal to the axis of rotation of SRR^{rot} was acquired. So the high in-plane resolution of ref_{orth} was in the plane to which all LR stacks were orthogonal. The SE direction of ref_{orth} was therefore parallel to the rotation axis of SRR^{rot}.

6.3.6 Influence of slice profile accuracy on SRR^{rot}

Analogously to subsection 4.3.3, the influence of the slice profile accuracy on the SRR result using rotated stacks was assessed with $\Delta z = 4$ mm and $\alpha = 9°$. For that, the measured

slice profile from Bloch simulations was approximated using once a Gaussian and once a rectangular approximation. The effect of inaccuracies in the slice profile on the results of SRR was evaluated quantitatively by calculating and comparing the RMSE of the T_1 values in two different ROI in the septum and the basal lateral part of the left ventricle with respect to ref_{XCAT}.
As already mentioned above, this evaluation was carried out using a simplified simulation of LR data, with SRR performed directly on the LR dynamics. Zero-mean noise was added.

6.3.7 Performance of SRR^{rot} with respect to resolving small structures

The performance of SRR^{rot} with respect to resolving small structures was evaluated by calculating the detectability of the fibrotic structures in simulated data as described in subsection 4.3.2, with $\Delta z = 4$ mm and $\alpha = 9°$. For the XCAT simulation, no k-space data was generated, but the SRR was directly applied to the LR dynamics to avoid misleading results due to cardiac motion correction and reconstruction artefacts.
The fibrotic structure was simulated as described in subsection 4.3.2. However, its orientation was changed, such that the differentiation between the fibrosis and the gap was orthogonal to the axis of rotation, so within the plane with the low spatial resolution.
Different thicknesses of fibrotic structures and the respective gap in between them were simulated in the range of one to five times the voxel size, so in the range of [1.3, ..., 6.5] mm. The detectability was compared between Γ_0, Γ_{final} and ref_{XCAT}.

6.4 Results

6.4.1 Minimisation of blood-flow artefacts

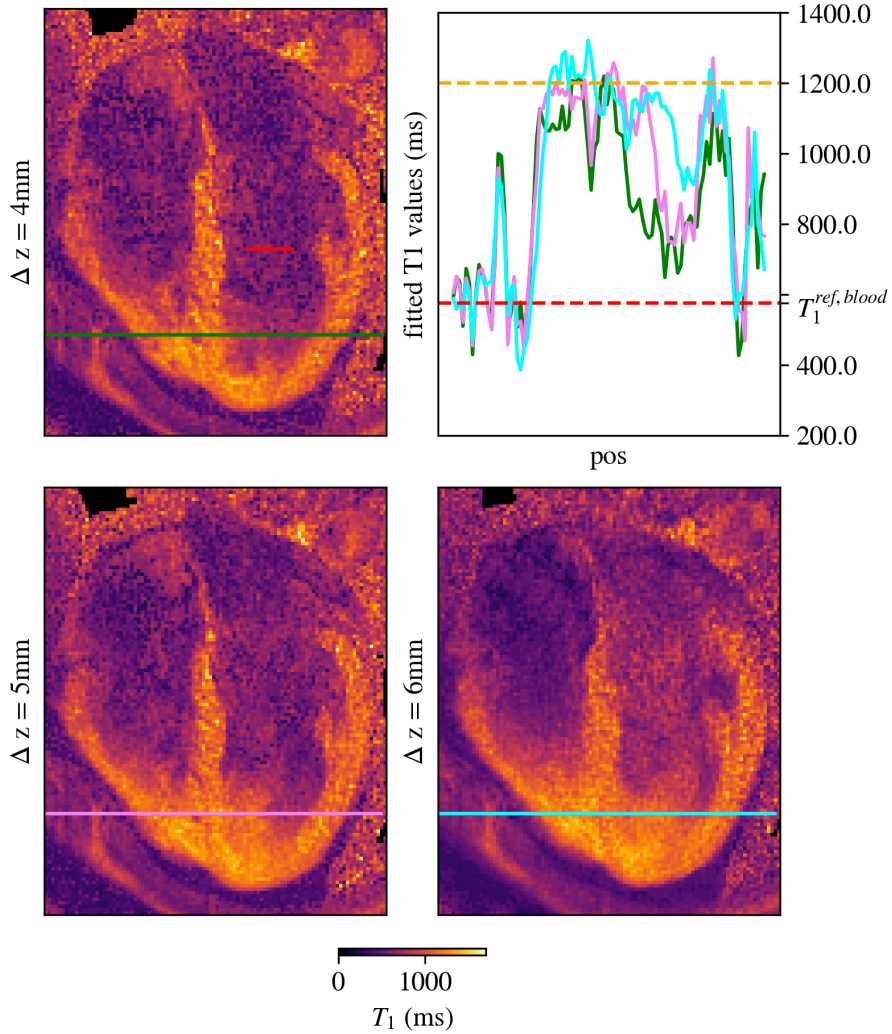

Figure 6.3: 4CH slice of a healthy volunteer with different slice thicknesses Δz. The T_1 values along an apical line are plotted in the upper right subplot. The reference T_1 value for blood $T_1^{ref,blood}$ is plotted dashed in red and the one for the myocardium in orange.

Figure 6.3 shows the T_1 values along a line through the apical region shown for different Δz. A reference value for the blood, the mean T_1 value in a basal blood ROI was calculated (see red line in upper left subplot in Figure 6.3), resulting in $T_1^{ref,blood} = 576.53$ ms. With $\Delta z = 6$ mm, it was challenging to differentiate myocardium and blood, with a T_1 value of the blood of 1098.24 ms (overestimation compared to T_1^{ref} by 90.49%). A Δz of 5 mm improved the differentiability, while the blood T_1 values were with a mean value of 938.19 ms still overestimated by 62.73%. The least overestimation of 34.23% was achieved with $\Delta z = 4mm$, with a T_1 value along the line of 773.88 ms.

6.4.2 Optimal flip angle for maximum SNR

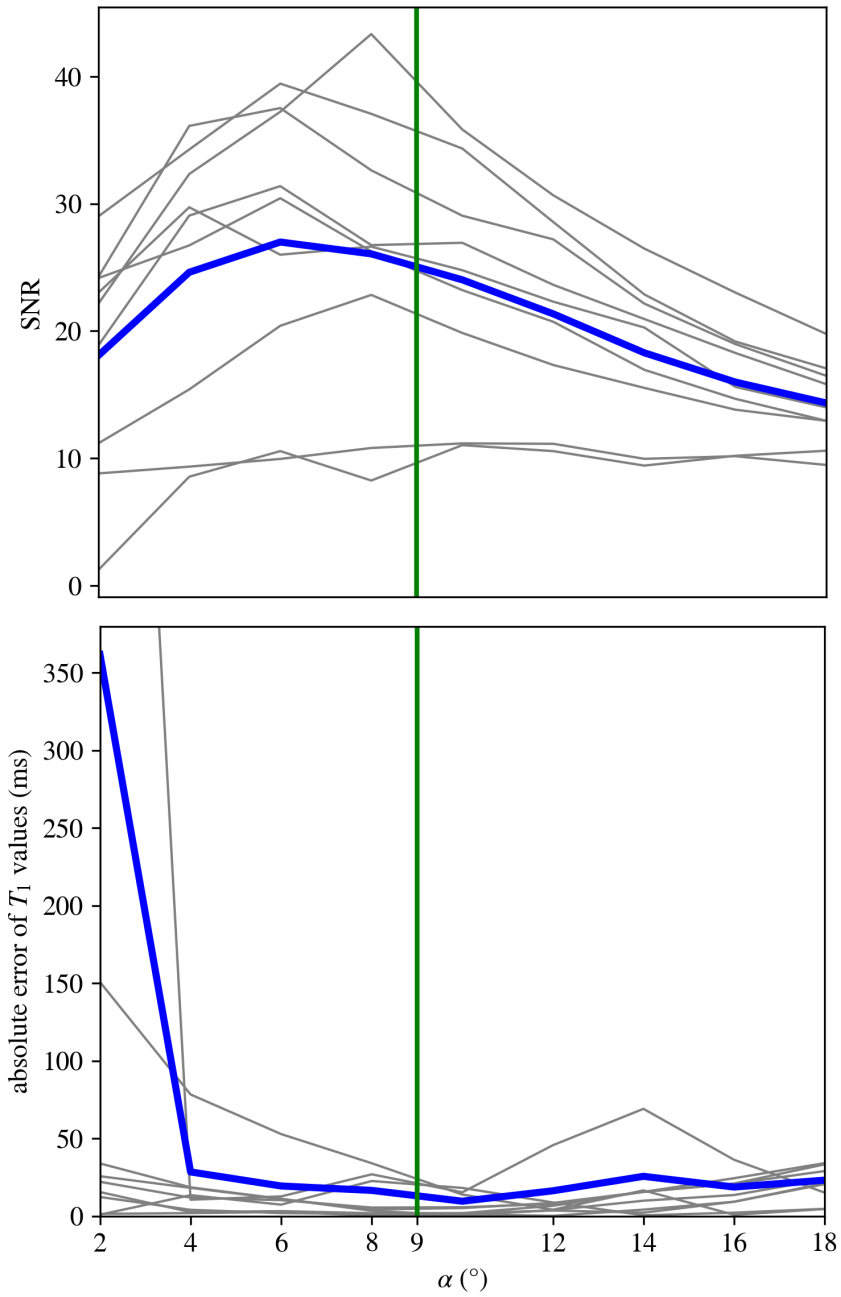

Figure 6.4: Effect of α on the error of fitted T_1 values and the SNR. The values for the single phantom tubes are shown in grey, while blue represents their mean.

The second row in Figure 6.4 shows the mean absolute error of the fitted T_1 values for the single phantom tubes in grey over different α and the RMSE over all tubes in blue. The α with the least RMSE of T_1 was for $\alpha = 10°$. In the first row, the SNR in the T_1 maps is shown. The α with the highest SNR was for $\alpha = 6°$.
An α of 9° will be used in the following work.

6.4.3 Optimize SRR^{rot} for cardiac applications

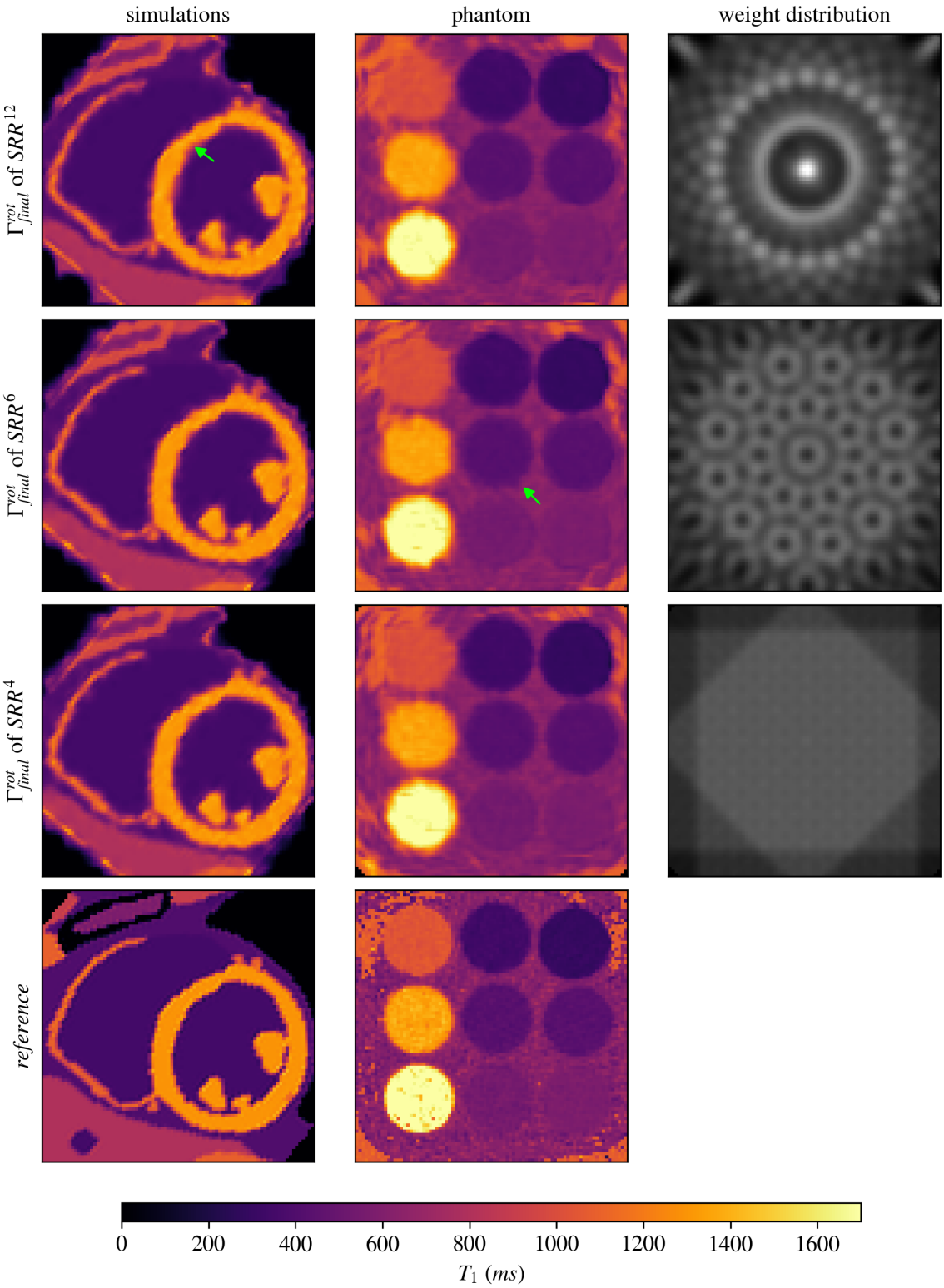

Figure 6.5: Simulation and phantom results of different SRR geometries compared to the reference (ref_{XCAT} for the simulation and ref_{orth} for the phantom data). The weight distribution of the SRR geometries shows the amount of LR information at a specific HR position (the brighter, the more information), as further explained in subsection 6.3.4.

Figure 6.5 shows the application of the model-based SRR on different SRR geometries with rotated stacks, using simulations and phantom data. The weight distribution shows how much information from all LR stacks was available at a HR position (the brighter, the more information). The different orientations of the stacks and filling or not filling of slice gaps in the SRR geometries led to different patterns in the weight distributions.
With SRR^{6} and SRR^{12}, artefacts can be seen, as highlighted by the arrows. The visualisation of small structures is most similar to the reference for SRR^{4}.
SRR^{rot} will from know on always be referring to SRR^{4}.

6.4.4 Numerical simulations and phantom experiments using SRR^{rot}

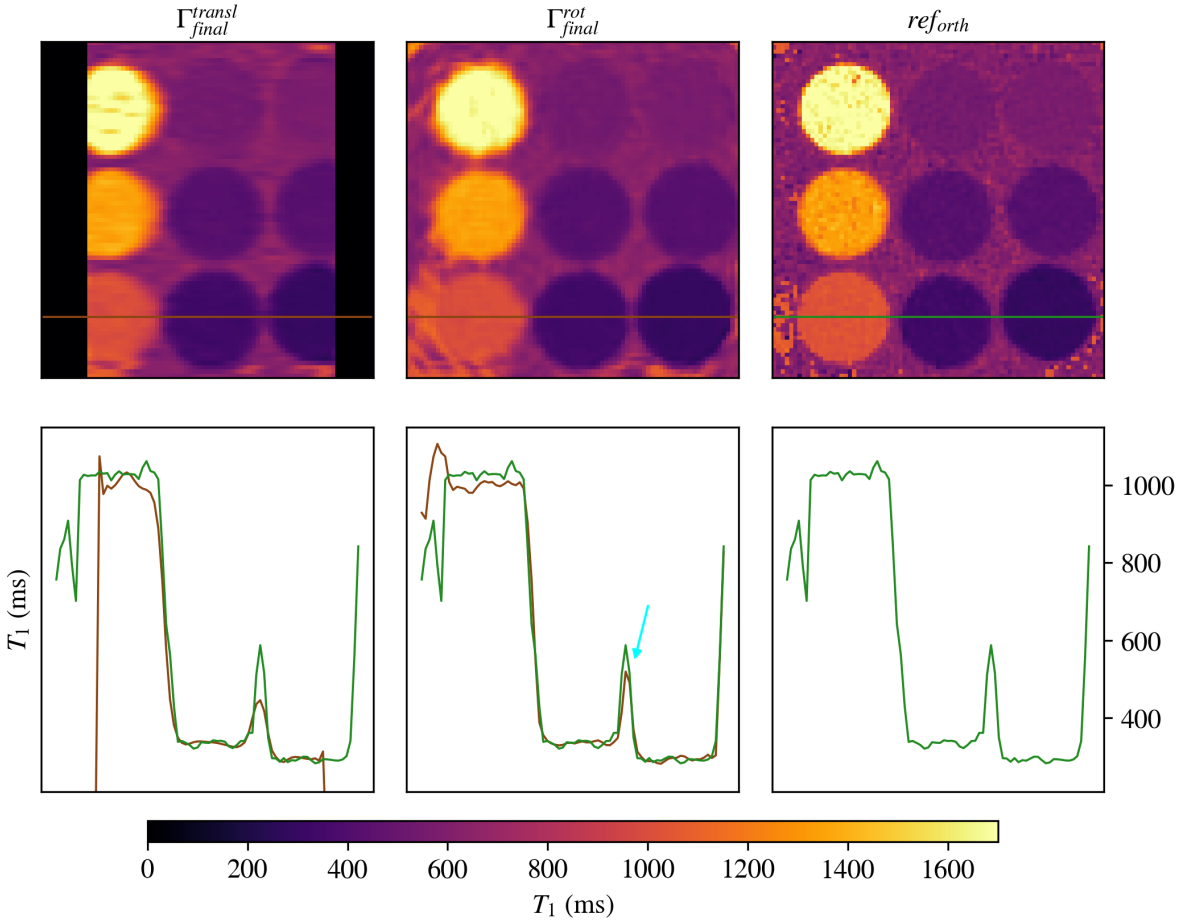

Figure 6.6: Application of the proposed approach on phantom data. In the same acquisition time, Γ^{rot}_{final} but not Γ^{transl}_{final} could recover the whole phantom tubes structure

.

Figure 6.6 shows the application of the proposed approach on phantom data (Γ^{rot}_{final}) and compares it with Γ^{transl}_{final} and ref_{orth}. While with the proposed number of stacks, SRR^{transl} could not image all phantom tubes, SRR^{rot} could cover the whole phantom and therefore captured a larger FOV.

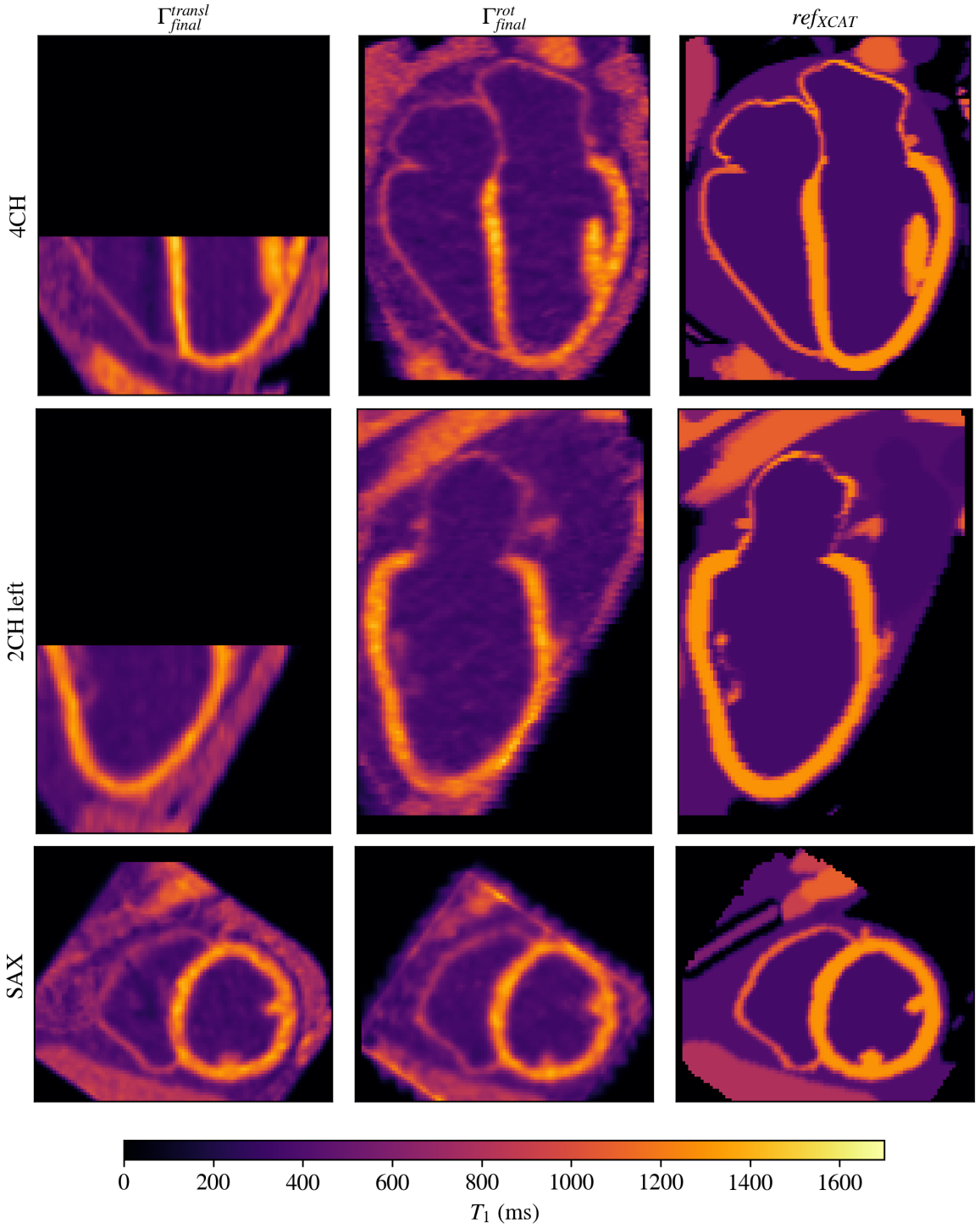

Figure 6.7: Application of the proposed approach on simulated data. Γ^{rot}_{final} and Γ^{transl}_{final} are compared to the ground truth. While SRR^{transl} was limited to the ventricles, the SRR^{rot} approach could cover the whole heart with the same number of LR stacks. No BH motion was simulated.

Figure 6.7 shows Γ^{rot}_{final} for the simulated data in all three common orientations and compares it to Γ^{transl}_{final} and ref_{XCAT}. With the same number of LR stacks and LR slices, SRR^{rot} could cover the whole heart while SRR^{transl} was limited to the ventricles.
As evaluated in a further experiment, The RMSE to the known simulated BH motion in

SRR^{rot} was [1.79, 1.59, 1.18] mm while the maximum possible RMSE was [2.14, 2.24, 1.29] and thus decreased by an average of 36.83%.
Visually, the myocardial structures were well recovered in the SAX of the heart when using rotated stacks, even though this orientation has never been acquired directly but was reconstructed from the other orientations.

6.4.5 Influence of slice profile accuracy on SRR^{rot}

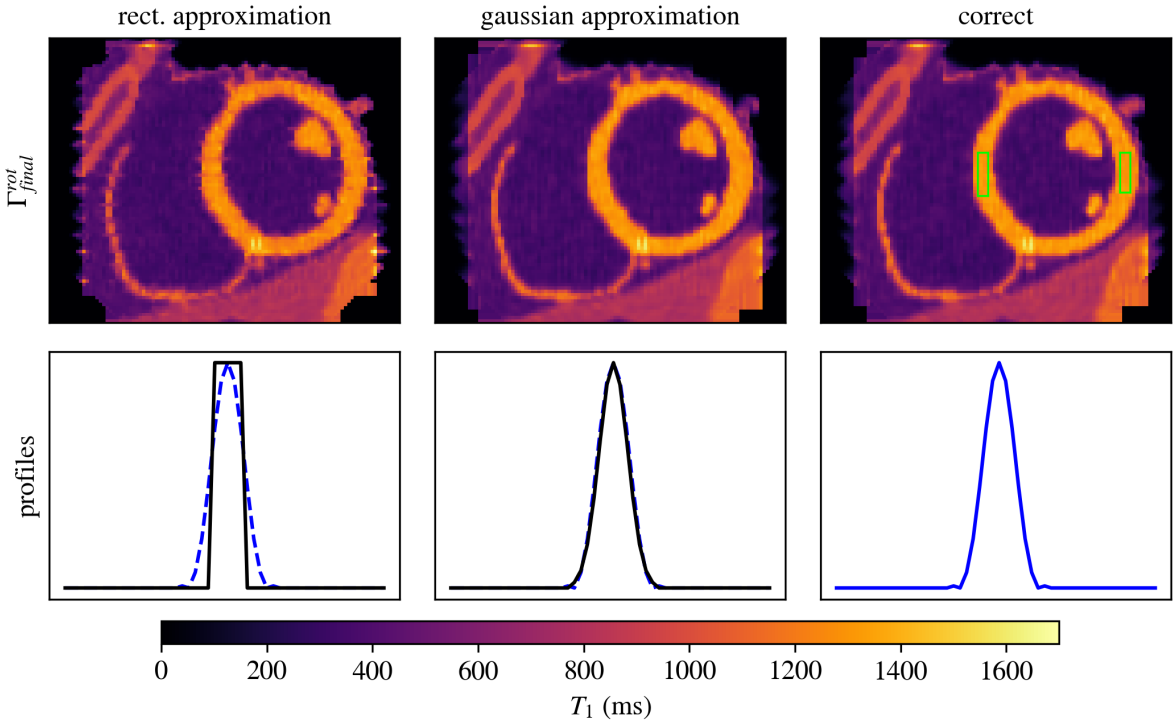

Figure 6.8: Influence of slice profile accuracy on SRR: The results of SRR using the correct slice profile (shown in blue) are compared to two SRR results using approximations (shown in black). The mean T_1 values in the green ROI are calculated for evaluation.

In Figure 6.8, Γ_{final} assuming different slice profiles for the SRR using rotated stacks is shown, analogously to subsection 4.4.2. While the first row shows the SRR result, the second row shows the correct slice profile used for the simulation of the LR slices in blue and the profile used for the optimisation in black.
The RMSE of the ROI in Γ_{final} compared to ref_{XCAT} using the Gaussian approximated increased by 61.66% and by 97.49% using the box-approximated profile. As seen in Figure 6.8, strong image artefacts appeared when assuming a box-approximated slice profile for the SRR.

6.4.6 Performance of SRR^{rot} with respect to resolving small structures

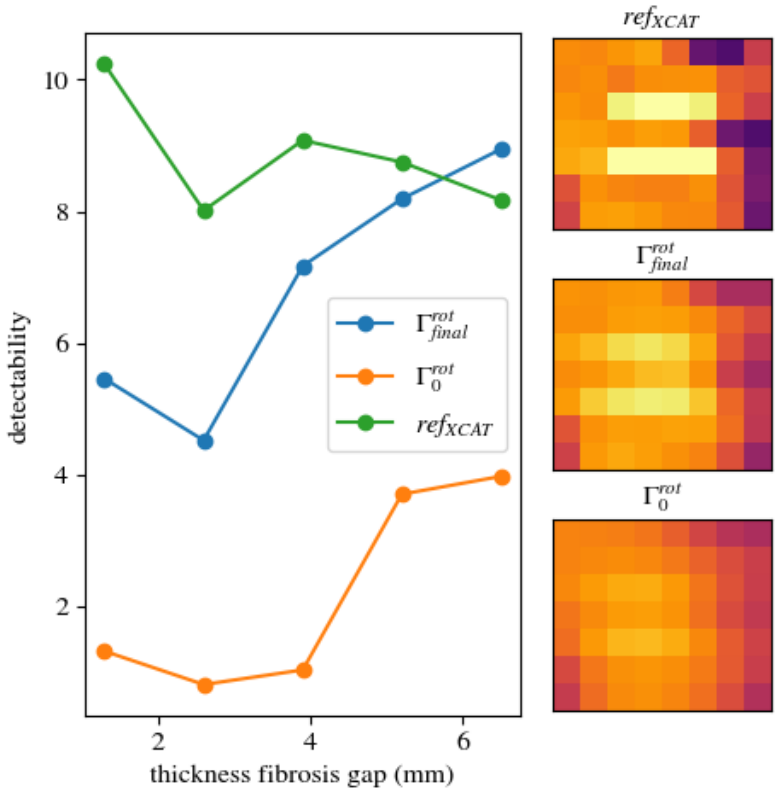

Figure 6.9: Influence of SRR^{rot} on detectability of simulated fibrosis. On the left side, the detectability for different sizes of fibrotic structures are shown for the reference, the SRR initialisation and the result. A zoom into the fibrosis with the size of 1.3 mm is shown on the right side.

Figure 6.9 shows the effect of SRR^{rot} on the simulated fibrotic structure. The SRR improved the detectability of the gap between the fibrosis by 419.07 ± 182.56% on average over all thicknesses compared to the SRR initialisation. The fibrosis gap with the thickness of 1.3 mm could not be resolved in Γ_0^{rot} but could be resolved after the SRR.

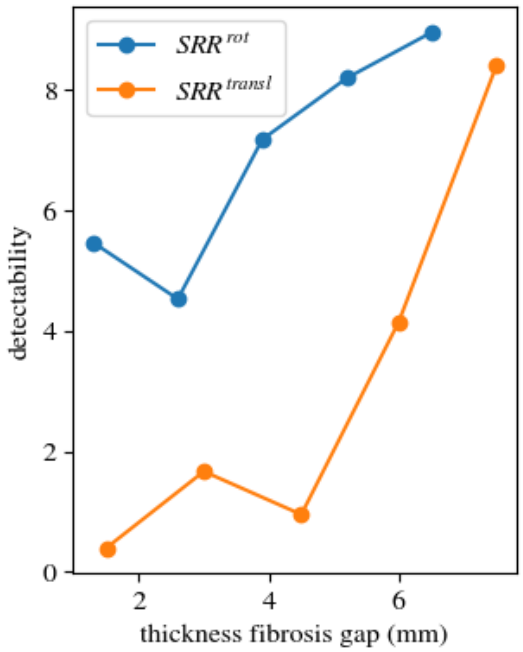

Figure 6.10: Comparison of the detectability of small structures after SRR^{rot} compared to SRR^{transl}.

In Figure 6.10, the comparison of the detectability achieved with SRR^{rot} and with SRR^{transl} is shown. The visualisation of small structures increased by 439.09 ± 470.62% over all fibrosis thicknesses using SRR^{rot} compared to SRR^{transl}.

6.5 Discussion

In this chapter, a SRR geometry with rotated stacks was proposed, which was able to increase the FOV of the HR volume to the whole heart without an increase in scan time. SRR^{rot} was therefore more efficient with respect to the heart coverage compared to SRR^{transl}.
For that, the acquisition parameter of the LR slices needed to be optimised to provide accurate T_1 values, especially in the apical region, while maximising the SNR. This led to a change of the LR slice thickness of Δz =4 mm and of the flip angle to $\alpha = 9°$. To still be able to accurately distinguish different T_1 relaxation times using the proposed signal model, the used flip angle should be less than 10° [49]. The inaccurate intensity values in the apical region are most likely due to some inverted blood staying inside the myocardium and not getting ejected, mixing with blood which has not been inverted.
The SRR acquisition geometry needed to be adapted for cardiac applications. Gaps needed to be introduced between the LR slices to cover the whole heart with each stack. However, the gaps between the slices could lead to an inhomogeneous amount of information contribution to different HR positions. As already shown for SRR applied on fetal brain MRI, gaps between the slices increase the number of stacks needed for a successful SRR [75]. As shown experimentally in this chapter, using some stacks to fill gaps of other stacks instead of introducing a new orientation reduced artefacts in the SRR result. This correlated with the respective weight distribution being the most homogeneous and the least amount of areas where no or only

little LR information was available. The artefacts, therefore, could be explained by the SRR having too little information from the LR stacks at these positions to reconstruct the original structures.
Next to that, the number of slices per LR stack was limited due to BH duration, so the gap between the slices was adjusted such that every stack covered a FOV of 76 mm in the SE direction. This resulted in an area of maximum LR information about approximately 76 mm in diameter, centred on the septum as the axis of rotation. However, this is only sufficient for patients with a rather small overall heart size [133]. This can be adapted to a larger heart by increasing the gap between the slices and thus requiring more stacks to fill the gaps.
The radial acquisition scheme leads to more information per HR position the closer the HR position is to the rotation axis since more stacks overlap in this region. This can also be seen in Figure 6.6, in which the tubes in the corner of the phantom received less LR information than the centre tube. This effect can be adjusted by changing the FOV in the SE direction acquired with each LR stack. The higher the covered FOV per LR stack, the farther the area with less LR information is from the rotation axis.
Matching the results from subsection 4.4.2, slice profile inaccuracies for the SRR led to artefacts. When using SRR^{rot}, the approximation of the slice profile led to strong image artefacts and significantly impaired the T_1 accuracy of the SRR result. Therefore, it can be concluded that an accurate modelling of the slice profile is an important factor for an accurate SRR result, which is in accordance with [115].
A model-based SRR scheme with differently rotated LR stacks could be applied for the first time to quantitative cardiac imaging. The performance of the proposed SRR scheme was evaluated quantitatively, and it could be shown that structures in the size of 1.3 mm could be resolved. The detectability of small structures of all sizes increased when using SRR^{rot} compared to SRR^{transl}, which is in accordance with previous research conducted on the brain [101, 115].
However, the proposed image-space-based SRR approach is limited by a lack of feedback between the SRR result and the raw k-space data. Undersampling artefacts in the reconstructed LR dynamics might propagate into the SRR result and impair the visualisation of small structures. This could be improved by using a k-space based SRR approach, as presented in chapter 7 and also used in [93, 94]. This might improve the overall image quality and the visualisation of small structures.

6.6 Conclusion

The reconstruction of a whole heart HR 1.3 mm isotropic cardiac T_1 map was proposed. For that, the acquisition of long-axis LR stacks with accurate T_1 estimates was optimised. Next to that, a SRR acquisition scheme with rotated stacks was presented and adapted for whole heart cardiac T_1 mapping. However, with the proposed image-space based SRR approach, undersampling artefacts in the reconstructed LR dynamics might propagate into the SRR result and impair the visualisation of small structures. This could be improved using a k-space-based approach, as introduced in the next chapter.

7

K-space-based whole-heart T_1 mapping

7.1 Introduction

Often for SRR, image-space-based approaches are used, so the LR images are reconstructed from the k-space data in a preprocessing step and then serve as a starting point for the SRR. Hence, for model-based SRR, the aim is to minimise the difference between the acquired LR dynamics and those predicted from the SRR result. However, these approaches mainly use fully sampled LR images [85, 84, 88]. Others [93, 94] used a k-space-based SRR approach, where no preprocessing reconstruction step is necessary for the SRR. So, the difference between the acquired k-space data and the one predicted from the SRR result is minimised. Thereby, the coil sensitivity maps and the FFT are integrated into the optimisation. This improved the visualisation of small structures compared to an image-space-based reconstruction [94]. Nevertheless, k-space-based SRR has so far only been applied to qualitative cardiac imaging [93] or to quantitative cartesian brain imaging [94].
In the previous chapter, high image quality could be achieved with the presented image-space-based SRR approach. Nonetheless, further improvement could be expected using a k-space-based SRR, considering the undersampled k-space trajectory.
This chapter proposes a cardiac whole-heart k-space-based SRR T_1 mapping approach and applies it to ten healthy volunteers. The proposed approach was evaluated in numerical simulations by comparing the proposed k-space SRR approach with an image-space-based SRR approach using rotated stacks (chapter 6) and with an image-space-based SRR approach using translated stacks in SAX orientation (chapter 4).

Parts of this chapter have been submitted for publication in J2.

7.2 Methods

7.2.1 Overall workflow of k-space-based cardiac SRR

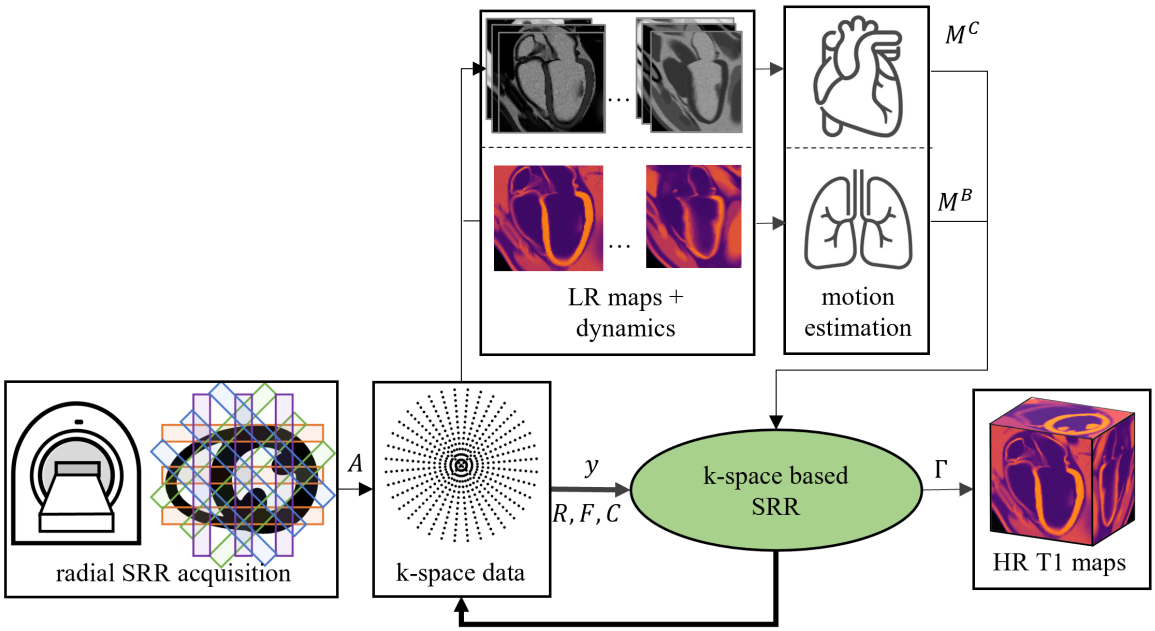

Figure 7.1: Schematic pipeline of the proposed approach. Several stacks were acquired with long-axis orientations rotated to each other, described by A. For cardiac motion estimation and BH alignment, LR dynamics and T_1 maps were reconstructed in a preprocessing step. The estimated motion M^C and M^B served as input for the following SRR. The SRR was k-space-based, so the acquired k-space data y as well as the radial k-space trajectory R, coil maps C and FFT F were part of the signal model in SRR. The SRR yielded a HR 3D T_1 map Γ. (source of parts: Shutterstock/howcolour)

The proposed workflow to acquire whole heart isotropic T_1 maps using a k-space-based SRR is depicted in Figure 7.1: After the application of an inversion pulse, multiple stacks of 2D slices with high in-plane but low through-plane resolution at different angles are acquired with a Golden radial k-space sampling scheme and a radial SRR acquisition scheme with one stack per BH. This results in radially overlapping stacks covering the whole heart, as described in subsection 6.2.2. The respective k-space data is then used to reconstruct the LR dynamics and T_1 maps, which are needed to estimate cardiac motion and BH alignment. The proposed scheme is k-space-based, so the SRR is applied to the raw k-space data and therefore also includes information about the k-space trajectory R, the coil maps C and the FFT F. After the iterative optimisation scheme of the SRR, a HR 3D T_1 map is obtained.

7.2.2 K-space-based SRR

For the proposed k-space-based SRR, the difference between the acquired k-space data y and the one predicted from the application of the acquisition model on the SRR volume Γ is minimised (see Equation 7.1). As for the image-space-based SRR (subsection 4.2.1), the acquisition model thereby consists of the T_1 relaxation model q, the translational BH motion M^B, and the downsampling operator A. For the k-space-based SRR, the cardiac motion fields M^C, the coil maps C, the FFT F and the radial k-space sampling operator R are also

integrated into the acquisition model. For regularisation, the parameter κ weights the influence of the total variation regularisation based on the forward finite differences operator G and the data consistency term. The sum over all stacks s and inversion times t (with $s = 1, \dots N_S$ and $t = 1, \dots, N_T$, with N_S being the number of stacks and N_T being the number of inversion times) is minimised.

$$\min_{\Gamma} \sum_{t=1}^{N_T} \sum_{s=1}^{N_S} ||y_{t,s} - R * F * C_s * M_s^C * M_s^B * A_s * q_t(\Gamma)||_2^2 + \kappa ||G * \Gamma||_1 \tag{7.1}$$

M^B only includes the detected motion in the readout and SE direction. As the LR stacks are rotated around the PE axis, shifts in the PE correspond to a shift in the in-plane dimension of the LR images. So translation in the PE direction is implemented as a preprocessing phase shift directly applied to the acquired k-space data.
Since the non-smoothness of the L1-norm as well as the non-linear function q make solving Equation 7.1 challenging, a variable splitting [93, 94, 116] approach is used, analogously to subsection 4.2.2. Auxiliary variables $x_t := q_t(\Gamma)$ for all t and $u := \Gamma$ are introduced, and these equalities are relaxed by including two quadratic penalty terms, weighted by λ and μ. This yields the following equation:

$$\min_{\Gamma,x,u} \sum_{t=1}^{N_T} \sum_{s=1}^{N_S} ||y_{t,s} - R*F*C_s*M_s^C*M_s^B*A_s*x_t||_2^2 + \lambda||x_t - q_t(\Gamma)||_2^2 + \mu||u-\Gamma||_2^2 + \kappa||G*u||_1 \tag{7.2}$$

Equation 7.2 is split into three subproblems, and its solution is approached by alternating the minimisation of the subproblems. For that, only one of the variables of the subproblem is optimised, and the two others are fixed. Fixing Γ and x thus leads to

$$\min_{u} \frac{\mu}{\kappa} ||u - \Gamma||_2^2 + ||G * u||_1 \tag{7.2.1}$$

Subproblem 7.2.1 is solved using the iterative algorithm proposed in [117].
Fixing Γ and u thus leads to

$$\min_{x} \sum_{t=1}^{N_T} \sum_{s=1}^{N_S} ||y_{t,s} - R * F * C_s * M_s^C * M_s^B * A_s * x_t||_2^2 + \lambda ||x_t - q_t(\Gamma)||_2^2 \tag{7.2.2}$$

Subproblem 7.2.2 is solved using a conjugate gradient approach. Five iterations were used per alternation.
Fixing x and u and updating Γ leads to

$$\min_{\Gamma} \sum_{t=1}^{N_T} \lambda ||x_t - q_t(\Gamma)||_2^2 + \mu ||u - \Gamma||_2^2 \tag{7.2.3}$$

Since the phase difference between x_t and $q_t(\Gamma)$ is assumed not to influence the other subproblems relevantly, the constraint is further relaxed by $\angle x_t = \angle q_t(\Gamma)$, similarly to [134]. Subproblem 7.2.3 is solved using the Limited-memory Broyden-Fletcher-Goldfarb-Shanno algorithm [118] with ten iterations per alternation.

To approach the solution of Equation 7.1, all subproblems are alternated three times.
For initialisation of Γ and subproblem 7.2.3, the individual slices of the LR stacks are reconstructed using a conjugate gradient approach, a three-parameter fit is applied and combining these maps using the transpose of A results in Γ_0, analogously to subsection 4.2.2. For initialization of subproblem 7.2.1, u is set to Γ_0. Subproblem 7.2.2 is initialized by $x_t = q_t(\Gamma_0)$. Γ_0 for initialisation of the subproblems is updated after every alternation.

7.3 Experiments

Data was acquired with the geometry as described in subsection 6.3.5, so 12 stacks were acquired, with the orientations (0, 45, 90, 135)° and three stacks per orientation, shifted to one another by 6 mm.
As nomenclature, in the following, the subscript will describe the type of SRR reconstruction (i for image-space-based or k for k-space-based). The subscript, therefore, will no longer indicate whether the variable shows the SRR initialisation or result, but from now on, only the SRR result will be shown. So the proposed method yielded Γ_k^{rot}.

7.3.1 Simulations

Simulated k-space data was generated as described in subsection 3.3.1. No BH motion was simulated, as its correction was already evaluated in subsection 6.4.4. As a quantitative evaluation, the edge sharpness of the septum in Γ_i^{transl}, Γ_i^{rot}, Γ_k^{rot} and ref_{XCAT} was compared, calculated as described in subsection 5.3.3.

7.3.2 Phantom

Phantom data was acquired as described in subsection 3.3.1.
The edge sharpness of the phantom tubes was calculated and compared between the different approaches. The difference between the average edge sharpness of Γ_i^{rot} and Γ_k^{rot} was evaluated on statistical difference using a paired student T-test.
Next to that, several ROI were selected in each of the nine phantom tubes and the average and SD of the T_1 values were compared between Γ_i^{rot} and ref_{IRSE} as well as between Γ_k^{rot} and ref_{IRSE}. To assess the accuracy of the SRR, Pearson's correlation coefficients and the paired student T-test P-values between Γ_i^{rot} and ref_{IRSE} and Γ_k^{rot} and ref_{IRSE} were calculated.

7.3.3 *In vivo*

To evaluate the proposed approach *in vivo*, data was obtained from ten healthy subjects (7 males, 3 females, aged 30.3 ± 2.28 years). All subjects gave written informed consent before participation in accordance with the institution's ethical committee.
For quantitative reference, a 3(3)3(3)5 MOLLI scan ref_{MOLLI} was acquired with the following scan parameter: FOV: 360 × 323 mm^2, TE / TR: 1.12 / 2.7 ms, α: 35°, and spatial resolution: 2.1 × 1.4 × 6 mm^3. Overall, eight slices were acquired with the following orientations and positions: 4CH, 2CH of the left ventricle, 2CH of the right ventricle, and SAX at the following

positions: apex, apical, mid-ventricular, basal and atrial.
For anatomic reference, a turbo-spin-echo (TSE) black-blood sequence ref_{TSE} was used with the following parameters: FOV: 340 × 276 mm^2, TE / TR: 28.0 / 700.0 ms, α: 180°, and spatial resolution: 1.3 × 1.3 × 5 mm^3. Overall, five slices were acquired with the following orientations and positions: 4CH, 2CH of the left ventricle, 2CH of the right ventricle, and SAX at mid-ventricular and atrial positions.
To assess the performance of the k-space-based reconstruction in *in vivo* experiments, γ^{rot}, Γ_i^{rot} and Γ_k^{rot} were qualitatively compared. Next to that, a qualitative comparison between Γ_k^{rot} and ref_{MOLLI} and ref_{TSE} reference scans was performed.
The accuracy of the T_1 values was evaluated quantitatively by comparing the bull's eye plots [123] of Γ_k^{rot} to ref_{MOLLI}. For this, the mean T_1 values in each myocardial segment of each volunteer were calculated, and the mean and SD over the volunteers of these values were plotted for Γ_k^{rot} and ref_{MOLLI}. Next to that, the mean absolute difference in the T_1 values of the different myocardial segments between ref_{MOLLI} and Γ_k^{rot} was calculated. The precision of the T_1 values was evaluated by comparing the SD of the T_1 values within the different myocardial segments between Γ_k^{rot} and ref_{MOLLI} over all segments and all ten healthy volunteers.
Improvements compared to image-space-based SRR^{transl} and k-space-based SRR^{rot} approaches as well as the impact of motion on SRR^{rot} were investigated in a qualitative comparison between Γ_k^{rot} and Γ_i^{transl}.
The influence of the k-space-based reconstruction on noise and image contrast was evaluated using the contrast-to-noise ratio CNR. This was evaluated at the septum using the following formula:

$$CNR = \frac{\mu_{septum} - \mu_{blood}}{\sigma_{blood}} \tag{7.3}$$

Thereby, μ_{septum} describes the mean T_1 intensity in a ROI placed in the septum, μ_{blood} describes the mean T_1 intensity in a ROI placed in the blood adjacent to the septum and σ_{blood} describes the SD of the T_1 intensities in a ROI placed in the blood.

7.4 Results

7.4.1 Simulations

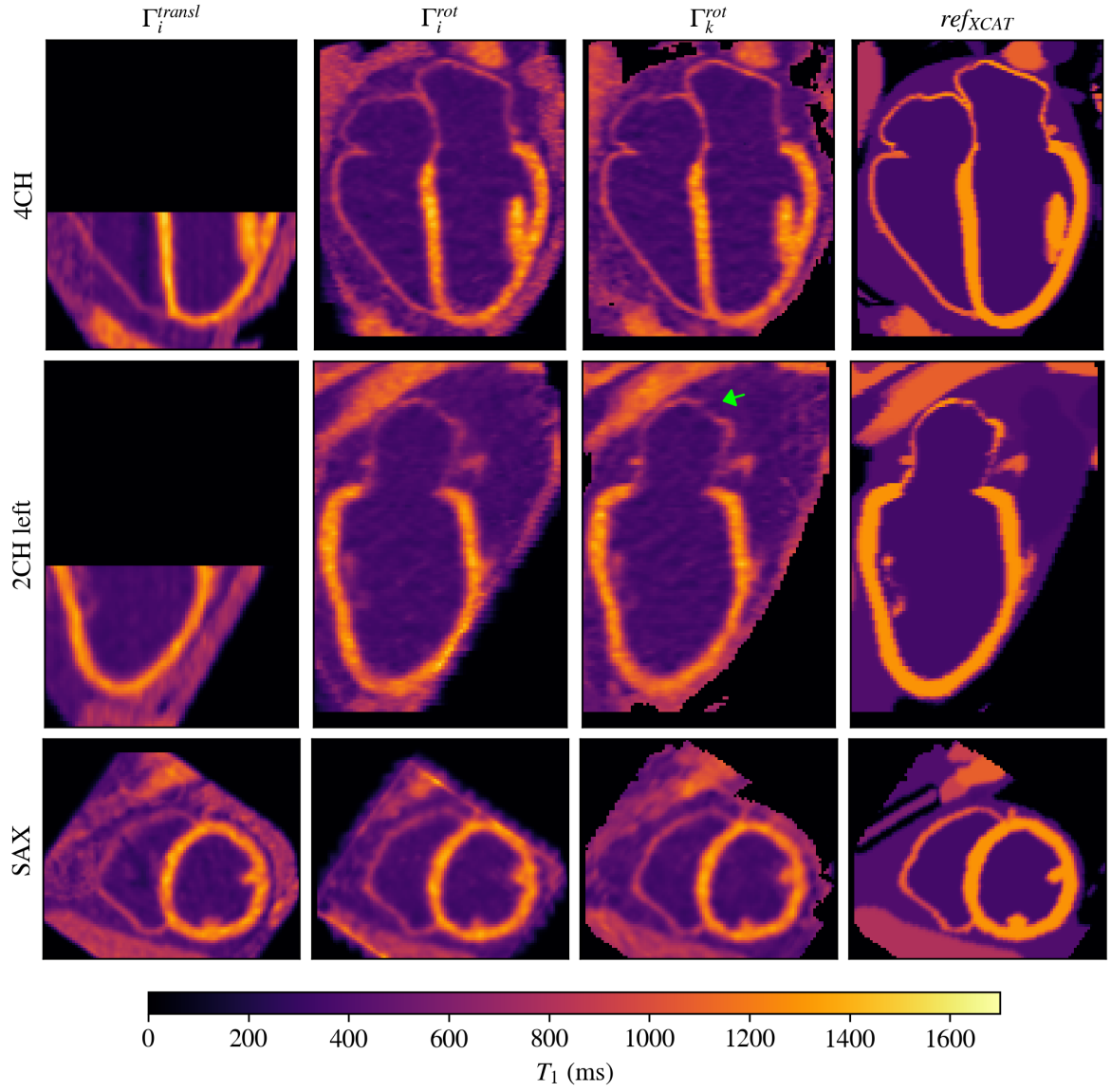

Figure 7.2: Application of the proposed approach on simulated data. While Γ_i^{transl} was limited to the ventricles, Γ_k^{rot} could cover the whole heart with the same number of LR stacks. Using a k-space-based reconstruction improved the visualisation of small structures such as the atrial wall (arrow). No BH motion was simulated.

Figure 7.2 shows the application of the proposed approach on simulated data and compares Γ_i^{transl} with the results from Γ_i^{rot}, Γ_k^{rot} and the ref_{XCAT}. The k-space-based reconstruction in Γ_k^{rot} improved the visualisation of thin structures such as the atrial wall (green arrow in Figure 7.2).

The edge sharpness of the septum increased from 0.28 in Γ_i^{rot} to 0.29 for Γ_k^{rot} and was 0.42 for ref_{XCAT}. So, the k-space-based reconstruction increased the edge sharpness of the septum by 6.2% compared to the image-space-based reconstruction.

7.4.2 Phantom

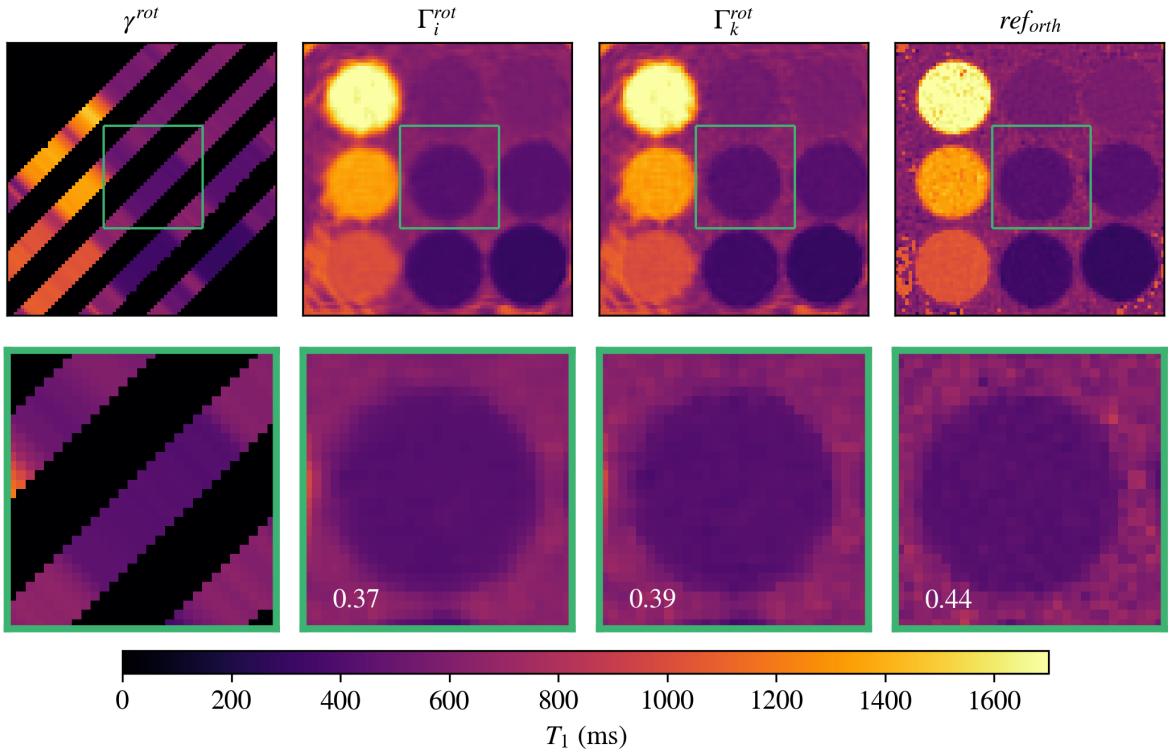

Figure 7.3: Application of the proposed approach on phantom data. The sharpness of the interface between tubes and phantom background increased when using the k-space-based SRR. This is highlighted in the zoom-ins in the second row with the measured sharpness value of the single tube in the corner.

Figure 7.3 shows the application of the proposed approach on phantom data and compares it with one of the LR stacks, Γ^i_{rot} and ref_{orth}. The sharpness of all tubes increased from 0.33 ± 0.05 for Γ_i^{rot} to 0.35 ± 0.05 for Γ_k^{rot}, corresponding to an increment in the sharpness of the tubes by 4.73% through the k-space-based reconstruction. The difference in sharpness values was statistically significant (P=0.01). The sharpness in ref_{orth} was 0.45 ± 0.08.
The average T_1 values of both Γ_k^{rot} and Γ_i^{rot} showed high correlation (P>0.61, R^2 >0.99) with the spin-echo reference ref_{IRSE}. The mean difference between the T_1 times in Γ_i^{rot} and ref_{IRSE} was 3.9 ± 21.18 ms and between Γ_k^{rot} and ref_{IRSE} 3.77 ± 23.26 ms. The mean absolute difference between the T_1 times in Γ_i^{rot} and ref_{IRSE} was 13.36 ± 16.90 ms and between Γ_k^{rot} and ref_{IRSE} 14.53 ± 18.56 ms.

7.4.3 *In vivo*

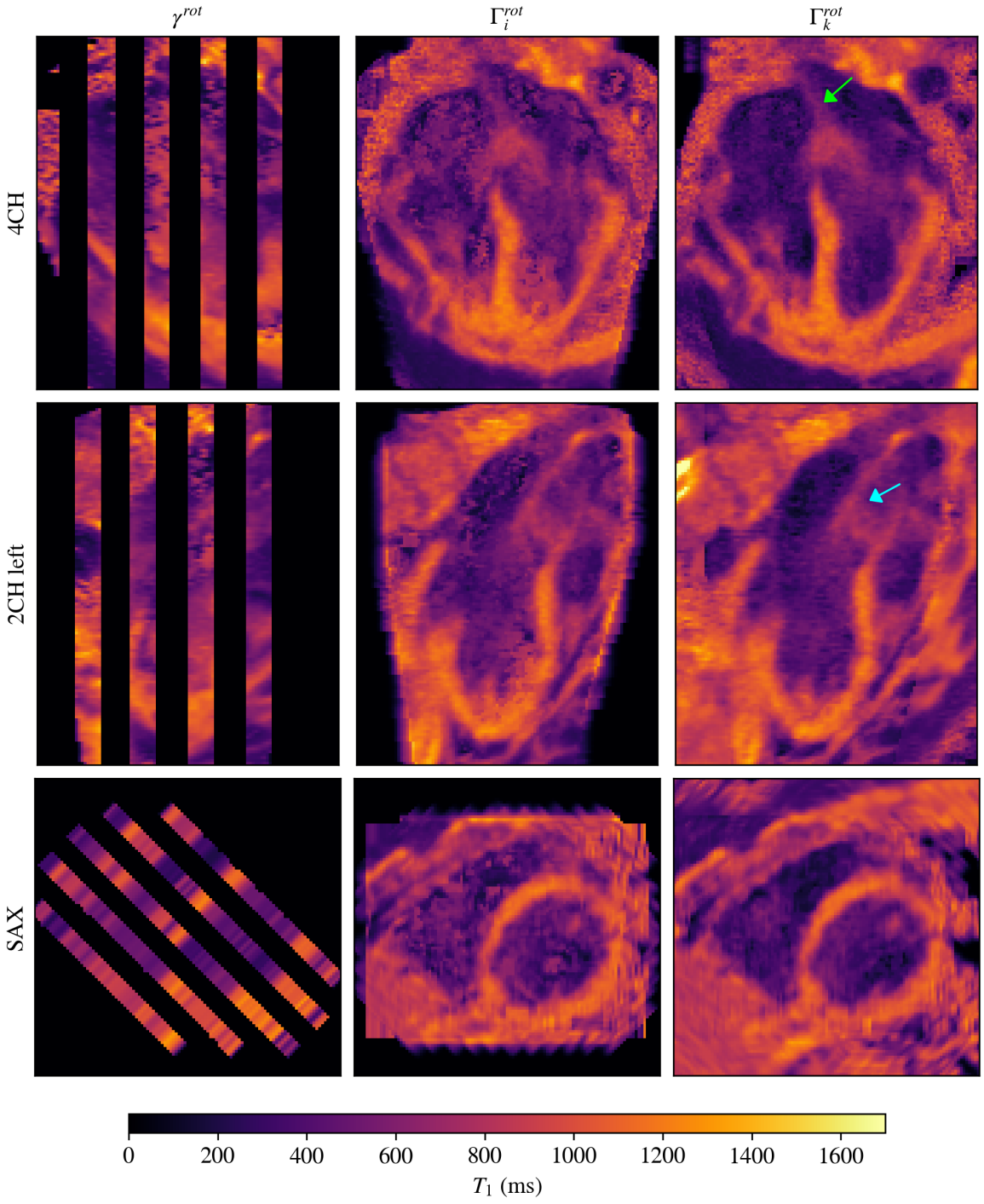

Figure 7.4: Application of k-space-based SRR on *in vivo* data. The SRR using rotated stacks could recover the standard SAX view. The k-space-based SRR improved the visualisation of small structures such as the interatrial septum (see green arrow) and the aortic wall (see blue arrow) and decreased the overall noise level.

In Figure 7.4, the application of the proposed approach on *in vivo* data is compared to the image-space-based SRR approach next to one LR stack. The whole myocardium, including the atria, could be visualised with the proposed approach. The image quality improved with the k-space-based SRR, as seen in the decreased overall noise and the increased contrast between myocardium and blood. The visualisation of small structures, such as the atrial wall, improved

(see arrows). The CNR at the septum over all volunteers was 8.44 ± 3.30 in Γ_i^{rot} and 9.66 ± 3.77 in Γ_k^{rot}, corresponding to an increment of 14.50% using a k-space-based SRR.

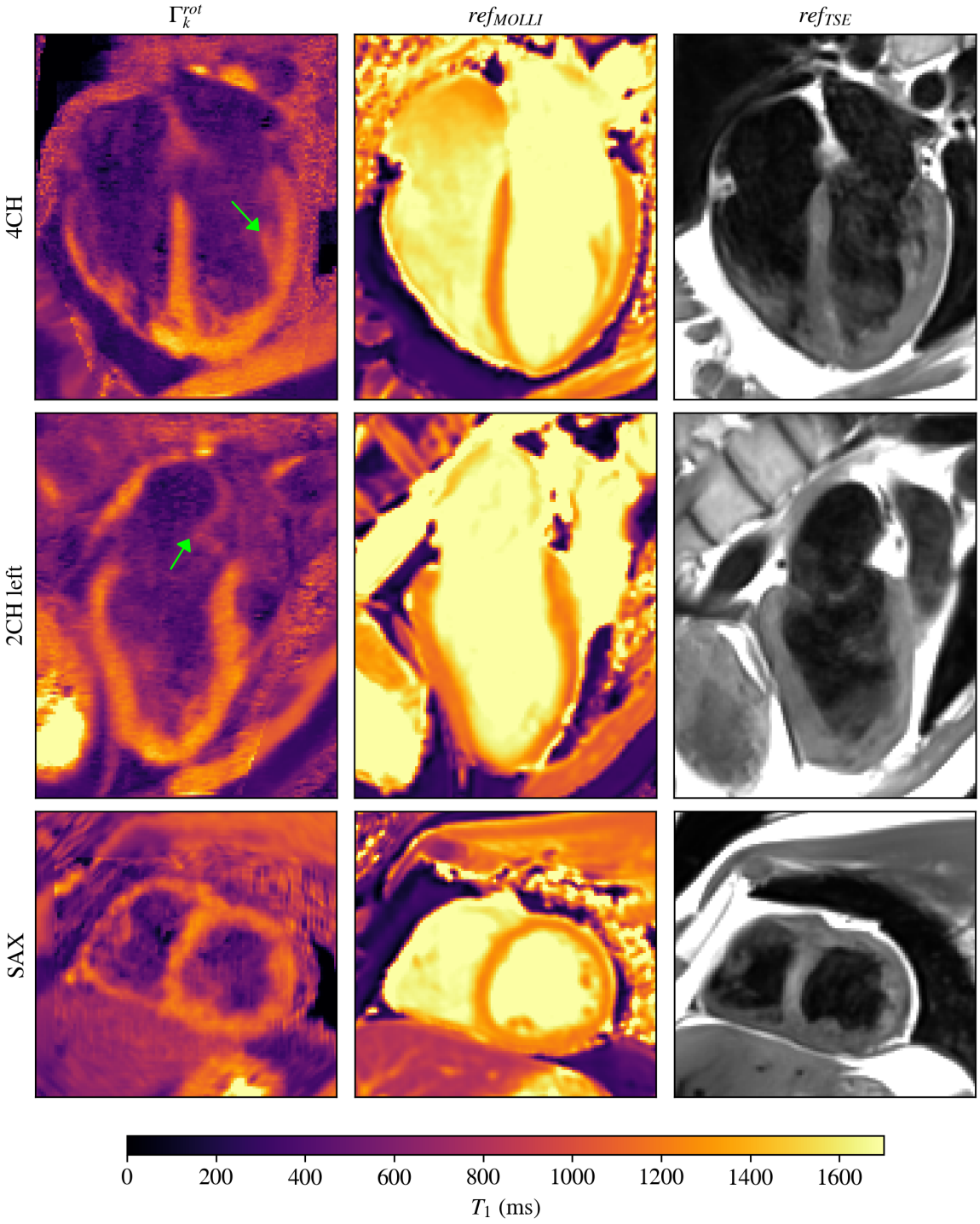

Figure 7.5: Application of the proposed approach on *in vivo* data, and comparison to ref_{MOLLI} and ref_{TSE}. Γ_k^{rot} matched the reference scans, and small structures such as the atrial wall or the papillary muscles could be recovered (arrows). In contrast to ref_{MOLLI}, blood could not be visualised with the SRR approach due to the use of slice-selective inversion pulses.

Figure 7.5 compares Γ_k^{rot} of one volunteer to ref_{MOLLI} and ref_{TSE} in all three orientations (SAX, 4CH, 2CH of the left ventricle). All three orientations could be captured well, and small details, such as the atrial wall (arrow), could be visualised.

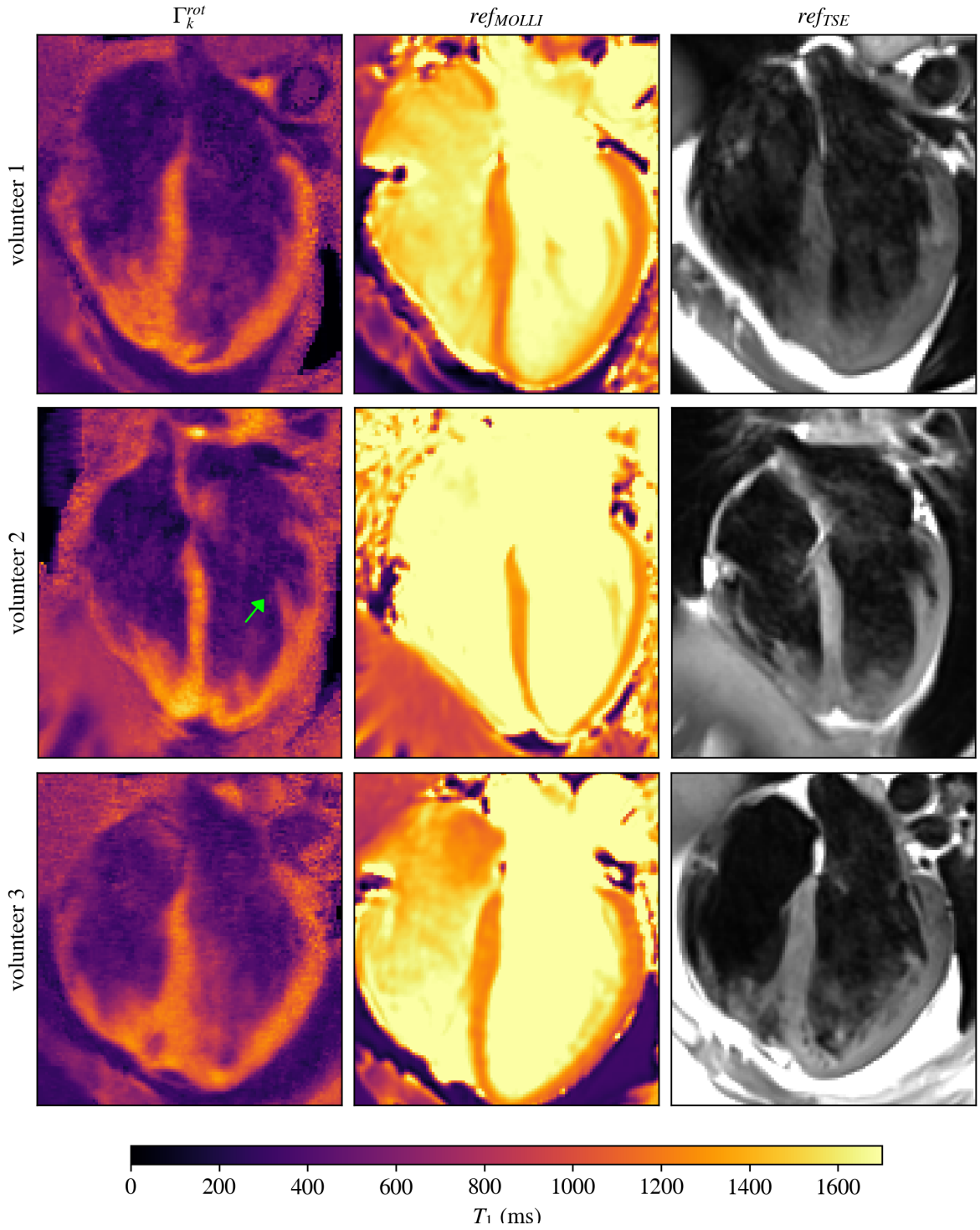

Figure 7.6: Application of the proposed approach Γ_k^{rot} on *in vivo* data and comparison to ref_{MOLLI} and ref_{TSE} in 4CH orientation. In addition to Figure 7.5, three more volunteers are shown here. Γ_k^{rot} matches the reference scans, and small structures such as the atrial wall or the papillary muscles could be captured.

Additionally, Figure 7.6 shows the results of the proposed approach applied to three more volunteers in 4CH and compares them to the reference scans. The results again matched the references, and small structures as the papillary muscles could be visualised (arrow).

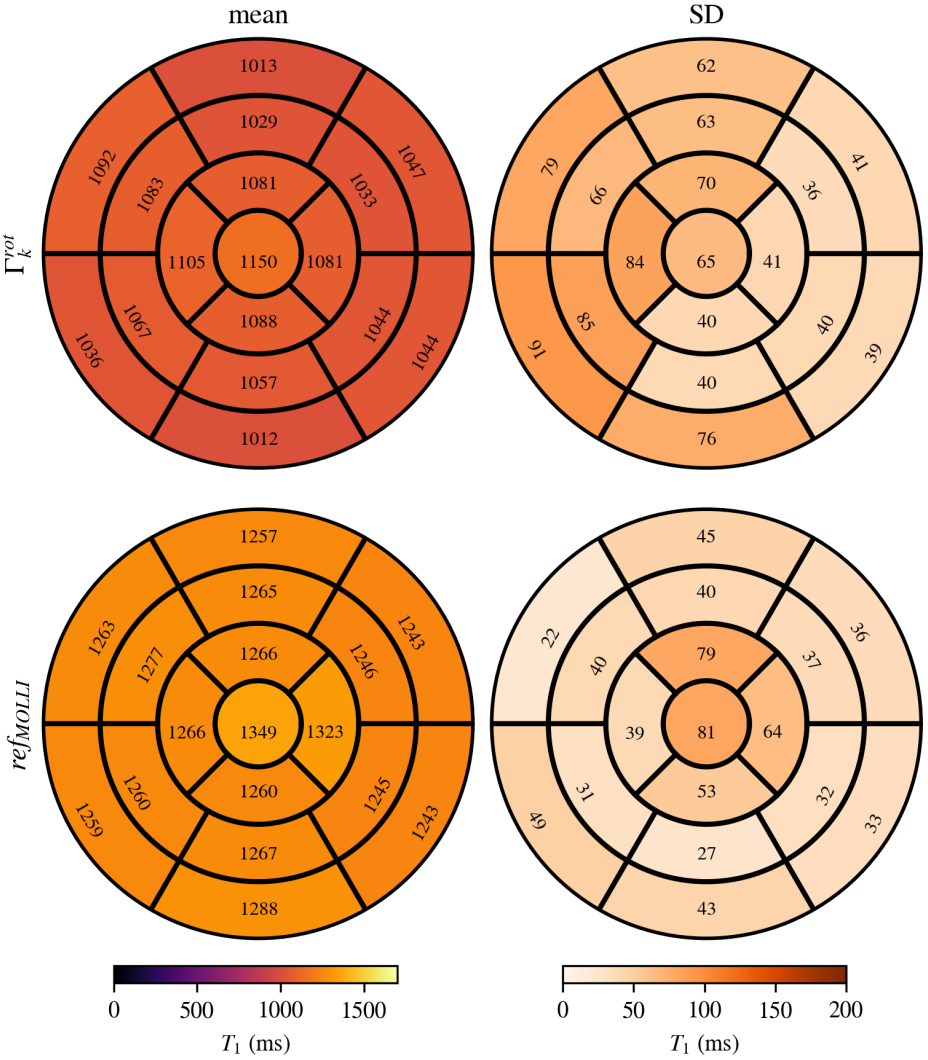

Figure 7.7: A bull's eye plot evaluation of the mean T_1 values and their standard deviation (SD) in ms in standardised myocardial segments of Γ_k^{rot} and of a MOLLI reference acquisition.

Figure 7.7 shows a bull's eye plot analysis [123] of the T_1 times of Γ_k^{rot} and ref_{MOLLI} of all ten healthy volunteers. The mean T_1 value over all volunteers and all myocardial segments was 1068.02 ± 71.45 ms using the proposed approach and 1261.15 ± 55.50 ms using MOLLI. T_1 was underestimated in Γ_k^{rot} by 193.14 ± 80.73 ms compared to ref_{MOLLI}, which can be attributed to the magnetisation transfer effects as a consequence of the slice selective inversion pulses [126] as well as residual BH motion artefacts. The SD within the myocardial segments was 64.32 ± 22.77 ms over all segments and volunteers for Γ_k^{rot} and 44.73 ± 31.90 ms for ref_{MOLLI}. These SD were comparable, indicating high precision.

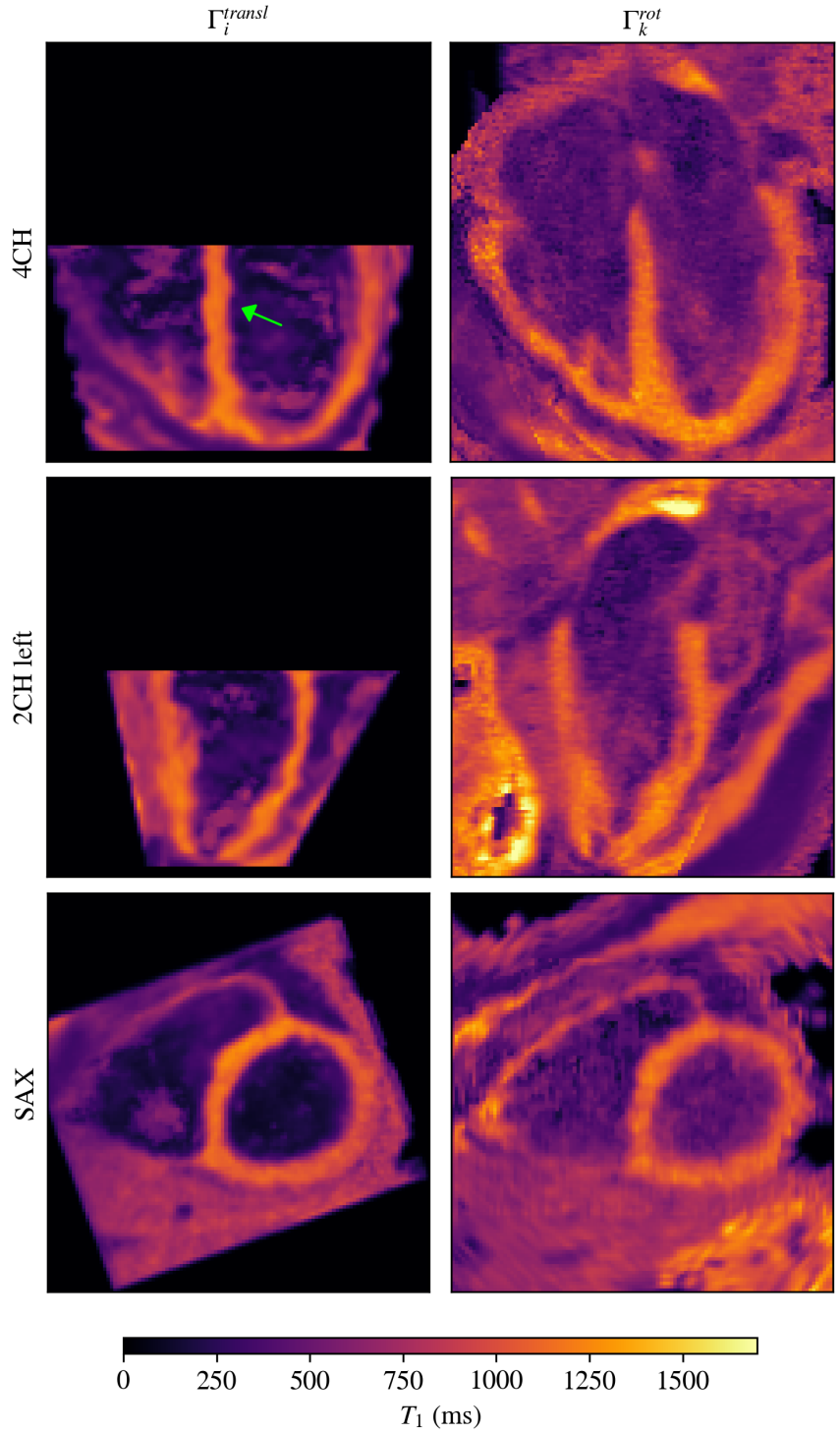

Figure 7.8: A comparison of Γ_k^{rot} and Γ_i^{transl} *in vivo*: With Γ_k^{rot} the whole heart could be covered while Γ_i^{transl} was restricted to the ventricles. Artefacts appearing as discontinuities in the septum (arrow) could be seen in Γ_i^{transl} but not in Γ_k^{rot}, which could be attributed to residual motion artefacts in Γ_i^{transl}.

In Figure 7.8, Γ_k^{rot} is compared to Γ_i^{transl}. With the same number of LR stacks, Γ_k^{rot} could cover the whole heart while Γ_i^{transl} was restricted to the ventricles. Artefacts appearing as discontinuities in the septum (arrow) could be seen in Γ_i^{transl} but not in Γ_k^{rot}, which could be attributed to residual motion artefacts.

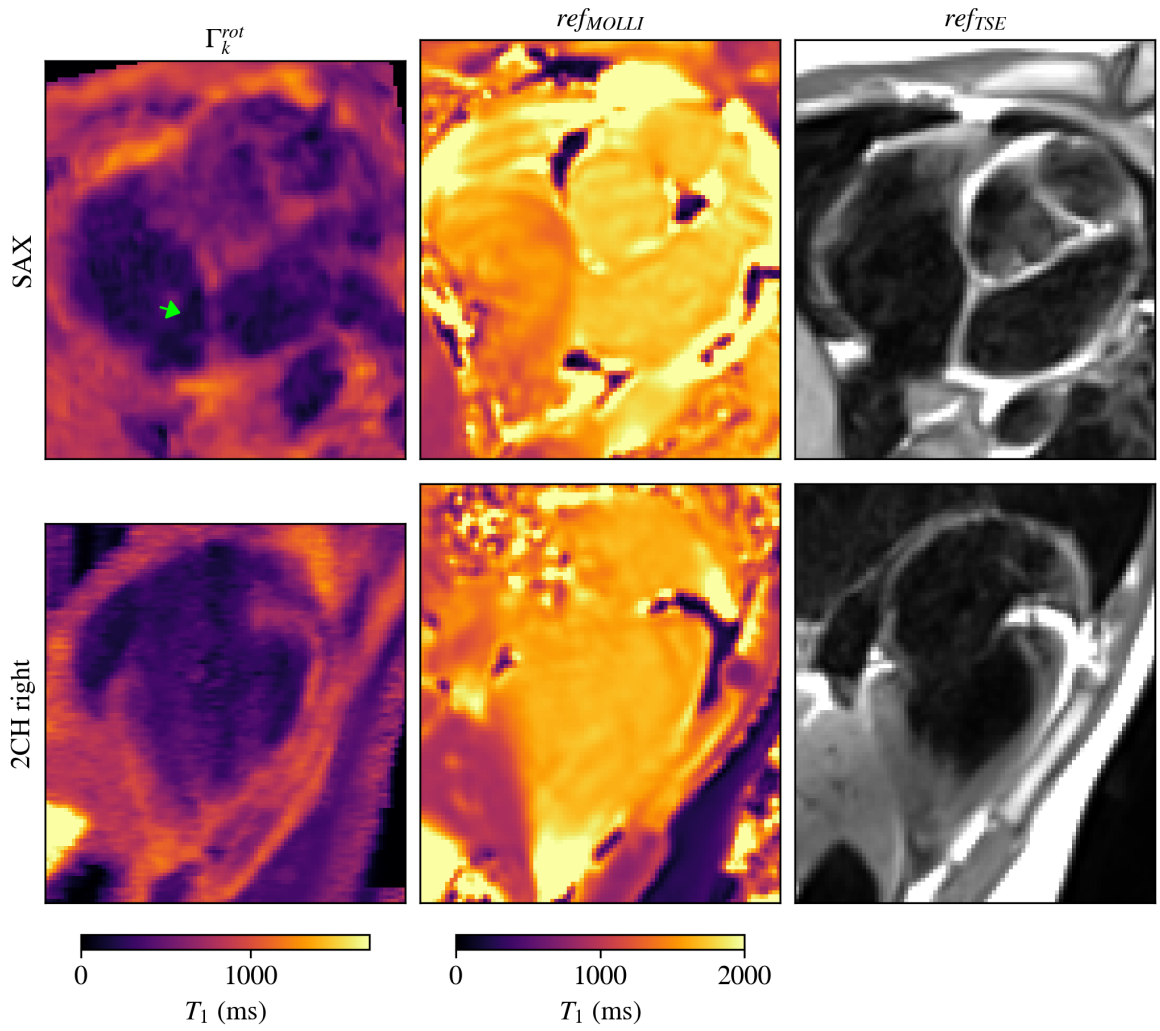

Figure 7.9: The application of the proposed approach on *in vivo* data in uncommon slice positions showing small myocardial structures and comparison to ref_{MOLLI} and ref_{TSE}. Small structures in the SAX view through the interatrial septum (arrow) and in the 2CH view of the right ventricle could be recovered. Different colour bars have been used for ref_{MOLLI} and Γ_k^{rot} to adapt to the different T_1 intensities of blood.

Figure 7.9 compares the application of the proposed approach to reference scans at oblique slice positions showing small myocardial structures such as the SAX through the atria and the 2CH of the right ventricle. The proposed approach could partially recover small details in the atrial walls. The right ventricular wall could be fully captured.

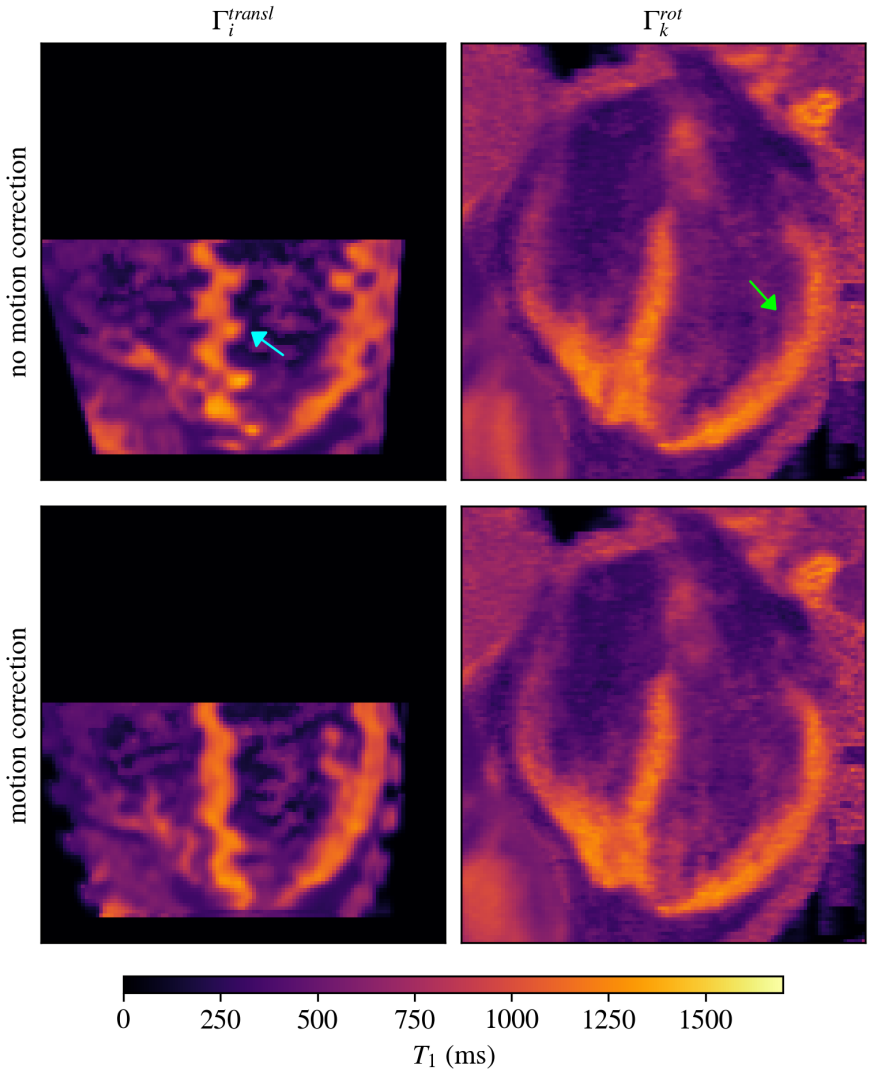

Figure 7.10: Comparison of the influence of motion on different SRR schemes applied to *in vivo* data. Major motion artefacts (blue arrow) were induced by different BH positions in Γ_i^{transl} without any motion correction. In Γ_k^{rot}, motion between the stacks led to minor artefacts such as blurring (green arrow), which could be removed after applying the proposed moco scheme.

In Figure 7.10, the influence of motion on different SRR schemes is shown. The motion detected in Γ_i^{transl} was in the range of [7.8, 9.1, 2.6] mm in the three different directions and the range of [1.3, 3.9, 3.9] mm for Γ_k^{rot}. Motion induced by different BH positions led to major zig-zag artefacts in Γ_i^{transl}. In the proposed approach, motion led to minor artefacts, such as blurring, which could be reduced with the proposed motion correction scheme.

7.5 Discussion

In the proposed approach, the whole heart could be covered in 12 BH and an overall scan time of approximately three minutes, excluding breaks between individual BH. The application of a k-space-based radial SRR allowed the visualisation of, for example, the wall of the right ventricle and parts of the atrial wall. Cardiac motion could be corrected, and different BH positions could be aligned. The proposed approach provided precise T_1 maps.

The proposed k-space-based reconstruction outperformed the previously presented image-space-based reconstruction. By the integration of the T_1 relaxation model, the BH motion, the downsampling operator, the cardiac motion fields, the coil maps, the FFT and the radial k-space trajectory into the optimisation, the visualisation of small structures improved, which is in accordance with previous methods proposed for k-space-based SRR of the brain [94].
The results of the proposed approach agreed well with the reference scans. The *in vivo* results could, however, not be directly compared with ref_{MOLLI} and ref_{TSE} because each scan was acquired in a different BH. Nevertheless, the simulations and phantom experiments suggest that the proposed approach provides accurate T_1 quantification.
As shown in Figure 7.10, SRR^{rot} showed less pronounced artefacts due to motion compared to SRR^{transl}, which was in agreement with [101]. Motion using SRR^{transl} led to strong zig-zag artefacts, while motion using SRR^{rot} led to minor artefacts such as blurring. Any residual uncorrected motion, therefore, also impairs the quality of the T_1 maps more using SRR^{transl} than using SRR^{rot}.
The approach was limited by not being able to accurately quantify the T_1 values of blood due to the use of a slice-selective inversion pulse. However, the low apparent T_1 time of blood can also be an advantage, as the contrast between the myocardium and the blood increases. This can be especially interesting for assessing small structures such as the atrial wall. To calculate the ECV, the acquisition of a single LR slice with a global inversion pulse would provide the required information regarding the T_1 values of the blood pool.
A limitation of the proposed approach is that the SAX for some volunteers showed more artefacts compared to SRR^{transl}. This can be traced back to imperfectness in motion correction, as unknown motion between the LR stack worsens the SRR result [64]. In the proposed approach, the SAX has never been acquired directly but was only reconstructed from other orientations using SRR, whereas SRR^{transl} always acquired SAX images and then reconstructed 4CH or 2CH out of the SRR result. Improvements in cardiac and BH motion correction and the use of more complex motion registration algorithms [85, 84, 114, 91, 75, 135, 81] might therefore improve the overall SRR result.
This work was only evaluated in healthy volunteers. However, based on the improved visualisation of small structures such as the atrial wall, it can be concluded that SRR will also lead to improved image quality with future applications in patients.

7.6 Conclusion

In this study, a novel 3D k-space-based SRR T_1 mapping approach with rotated stacks was proposed. Whole heart isotropic 1.3 mm T_1 maps were provided in an overall acquisition time of approximately three minutes. The visualisation of small structures improved, and the whole heart could be covered, including the atria.

8

Summary

In this thesis, a novel approach to obtain a whole-heart HR 3D cardiac T_1 map in an overall acquisition time of three minutes was developed and evaluated in numerical simulations, phantom experiments and *in vivo* studies. Scan time was used efficiently with a SRR approach, providing a HR volume with precise T_1 estimates in a short acquisition time. Good visualisation of small structures such as the right ventricular and atrial walls in a 3D HR T_1 map could be provided with a motion-corrected k-space-based SRR approach. Whole heart coverage was achieved with a radial SRR geometry. The provided T_1 estimates were accurate as shown in phantom experiments, and showed high precision in *in vivo* experiments.

As an alternative to SRR, HR imaging can be achieved by acquiring thin slices directly. However, keeping the acquisition time fixed would lead to a lower SNR. In chapter 3, it was confirmed experimentally for quantitative T_1 maps that it is more efficient to acquire thick slices compared to increasing the acquisition time and acquiring thin slices, motivating the use of SRR. As the output of the SRR depends strongly on its LR input data, in this chapter, the parameter for the acquisition of a single multi-slice stack with accurate T_1 estimates in a low acquisition time was optimised. The acquisition time of a single LR stack was minimised by using a slice-selective inversion pulse and, therefore, reducing the acquisition time of a single LR slice by approximately 60% compared to a non-selective inversion pulse. Furthermore, the width of the slice-selective inversion pulse was adapted with respect to robustness in case of motion and under consideration of the non-rectangular shape of the inversion pulse. Gaps between the LR slices were introduced for independence between the single slices. Next to that, a minimisation in acquisition time was demonstrated by using a cardiac motion correction approach. These optimisations allowed the acquisition of a single multi-slice slice stack of six slices of accurate and precise T_1 maps in an overall acquisition time of 16 seconds.

In chapter 4, a model-based SRR approach was developed, reconstructing a 3D HR T_1 map from the reconstructed dynamics and therefore being image-space based. The visualisation of small structures increased from 0.38% compared to the ground truth to 48.63%. Next to that, the influence of uncertainties in the knowledge about the acquisition geometry, for example,

slice profile or slice position, on the SRR was analysed. Uncorrected motion between the LR stacks has shown to be a major factor influencing the performance of the SRR.

In chapter 5, a motion correction scheme was developed to align different BH states. The proposed motion correction scheme performed successfully and reduced the residual motion by 97.79%. This allowed the successful application of the developed motion-correction SRR scheme on *in vivo* data and provided accurate ($P<0.001$, $R^2>0.999$) and precise (SD of 63.72 ms across the four healthy volunteers) T_1 values. The ability to differentiate small structures has been enhanced by 40% through the developed model-based motion-corrected SRR scheme and allowed the acquisition of a 3D HR T_1 map in six to ten 17 seconds long BH.

While the provided T_1 maps of the previous chapter were limited to the ventricles, a novel approach was developed in chapter 6, allowing an increase of the FOV to the whole heart by introducing a new SRR acquisition scheme. Acquiring long-axis images of the heart with different orientations instead of acquiring shifted SAX images thereby allowed the coverage of the whole heart in the same acquisition time. For that, the acquisition parameters needed to be optimised to provide accurate T_1 values for the long-axis images and to maximise the acquired signal. Different radial SRR acquisition geometries were evaluated to provide accurate T_1 estimates in cardiac applications. The motion alignment of different BH positions was adapted to the radial acquisition geometry. In simulation experiments, structures in the size of 1.3 mm could be differentiated with the proposed approach.

The developed approach was further improved in chapter 7 by introducing a k-space-based SRR approach, which could be successfully applied to ten healthy volunteers. The provided T_1 values were precise, and the contrast between myocardium and blood increased by 14.50% compared to an image-space-based SRR. Consequently, the whole heart could be covered in only three minutes overall acquisition time while a good visualisation of small structures was possible with an isotropic spatial resolution of 1.3 mm.

Uncorrected BH misalignment in between the different LR stacks has a strong impact on the final SRR results, as shown in subsection 4.4.3. Similar effects can be expected from insufficiently corrected cardiac motion. In future research, more advanced motion correction for the cardiac and BH motion correction might, therefore, improve the overall SRR result. The results of the motion correction could be improved by its integration into the optimisation scheme of the SRR, as described in [83–85, 93]. Furthermore, the integration of motion correction approaches as proposed for the application of SRR on fetal imaging [114, 91, 75, 135, 81] could further improve the overall SRR result. In this work, only translational misalignment between the BH states was corrected. Integrating rotation and deformation into the BH motion correction would probably further improve the SRR result. Registering the slices within one stack separately to the HR volume would also account for inter-stack motion due to poor breath holding.
In addition, instead of correcting the BH positions retrospectively, the position of the slices could be tracked prospectively and the acquisition adjusted accordingly, for example, using the

Pilot tone [57]. As assessed in subsection 3.4.2, a slice-selective inversion pulse broader than theoretically necessary needed to be used to account for motion in case of a non-consistent BH. In case of a prospective BH position correction, this buffer would not be necessary, thus avoiding the potential source of slice inversion error due to incorrectly estimated motion.
A drawback of the proposed approach is the computational complexity, leading to an overall computation time of approximately 24 hours for the reconstruction of the whole heart T_1 map of one volunteer, using a high-performance computer (2x24 Cores, Dual Intel Xeon Gold 6246, 768GB RAM).
For cardiac SRR, Deep Learning is used extensively in the literature [136, 137, 95, 138, 139] as also described in section 2.5. However, the physical acquisition model between the acquired k-space data and the SRR result has not been considered for quantitative cardiac imaging. For qualitative brain imaging, the integration of physics-based knowledge in the data-consistency layers of a neural network, along with deep learning regularisation techniques, has greatly enhanced the quality of the reconstructed images [140]. Future research could, therefore, combine physics-informed Deep Learning methods and multi-image SRR. This could combine the strong computational power of Deep Learning with the knowledge about the acquisition models of different LR stacks proposed in this work. By that, the reconstruction time could be accelerated, and the data consistency term of the physics-informed Deep Learning model would ensure the acquired k-space data still matches the SRR result.
To further speed up the total acquisition time, a simultaneous multi-slice sequence [141] could be used to acquire several slices in one stack at once and reduce the acquisition time per stack. For that, a multi-slice inversion pulse would be needed as described in [142].
The proposed SRR reconstruction problem relates the acquired k-space data to the HR T_1 parameter map via an acquisition and a signal model. This formulation is universal and can be applied to different quantitative imaging techniques, such as T_2 mapping, or even extended to MRI fingerprinting [143] approaches. Low through-plane resolution of cardiac T_2 maps may lower the sensitivity to small focal areas of inflammation [144] or oedema detection [145]. Next to that, in cardiac T_2 mapping, the FOV is often restricted to only a fraction of the left ventricle, potentially missing focal areas of inflammation [145]. In future applications, therefore, an application of SRR on T_2 mapping could also provide diagnostic information about oedema [15] in patients with myocardial infarction [146, 147], heart transplant rejection [148] or inflammatory cardiomyopathy [149].

9

Author's Publications

Journal Articles

J1 **Simone Hufnagel**, Selma Metzner, Kirsten Miriam Kerkering, Christoph Stefan Aigner, Andreas Kofler, Jeanette Schulz-Menger, Tobias Schaeffter, Christoph Kolbitsch. 3D model-based super-resolution motion-corrected cardiac T1 mapping. *Physics in Medicine and Biology.* 2022; 67 p. 245008, DOI: 10.1088/1361-6560/ac9c40

J2 **Simone Hufnagel**, Patrick Schuenke, Jeanette Schulz-Menger, Tobias Schaeffter, Christoph Kolbitsch. 3D whole heart k-space-based super-resolution cardiac T1 Mapping using rotated stacks. (*Under revision*)

J3 Maximilian Fenski, Darian Viezzer, Vy-An Nguyen, **Simone Hufnagel**, Christoph Kolbitsch, Maša Božić-Iven, Sebastian Weingaertner, Jeanette Schulz-Menger. Heart rate sensitivity in T1 -MOLLI, T2-bSSFP and T2-gradient echo based parametric mapping techniques at 1.5 Tesla – results of a simulation, phantom and healthy volunteer study (*Under revision*)

Conference Proceedings

C1 Maximilian Fenski, Darian Viezzer, Vy-An Nguyen, **Simone Hufnagel**, Christoph Kolbitsch, Jeanette Schulz-Menger. T1- and T2-parametric mapping at 1.5 Tesla: influence of heart rates in phantom study and healthy volunteers. *Proceedings of the 25th Annual Meeting of SCMR*, Florida, USA, pp. 000091, 2022

C2 **Simone Hufnagel**, Selma Metzner, Kirsten Miriam Kerkering, Christoph Stefan Aigner, Andreas Kofler, Jeanette Schulz-Menger, Tobias Schaeffter, Christoph Kolbitsch. 3D super-resolution motion-corrected cardiac T1 mapping. *Proceedings of the 30th Annual Meeting of ISMRM*, London, UK, pp. 1114, 2022

C3 **Simone Hufnagel**, Matthias Anders, Christoph Stefan Aigner, Helge Herthum, Heiko Tzschaetzsch, Tobias Schaeffter, Ingolf Sack, Christoph Kolbitsch. 3D super-resolution

MR elastography of the brain. *Proceedings of the 30th Annual Meeting of ISMRM*, London, UK, pp. 2065, 2022

C4 **Simone Hufnagel**, Patrick Schuenke, Jeanette Schulz-Menger, Tobias Schaeffter, Christoph Kolbitsch. Towards isotropic 3D whole-heart T1 mapping using model-based motion-corrected super-resolution reconstruction. *Proceedings of the 31st Annual Meeting of ISMRM*, Toronto, Canada, pp. 1093, 2023

C5 **Simone Hufnagel**, Patrick Schuenke, Jeanette Schulz-Menger, Tobias Schaeffter, Christoph Kolbitsch. Comparing different geometries for 3D radial super-resolution cardiac T1 Mapping. *Proceedings of the 25th Annual Meeting of DS-ISMRM*, Berlin, Germany, 2023.

References

[1] G. A. Roth, G. A. Mensah, C. O. Johnson, G. Addolorato, E. Ammirati, L. M. Baddour, N. C. Barengo, A. Z. Beaton, E. J. Benjamin, C. P. Benziger, A. Bonny, M. Brauer, M. Brodmann, T. J. Cahill, J. Carapetis, A. L. Catapano, S. S. Chugh, L. T. Cooper, J. Coresh, M. Criqui, N. DeCleene, K. A. Eagle, S. Emmons-Bell, V. L. Feigin, J. Fernandez-Sola, G. Fowkes, E. Gakidou, S. M. Grundy, F. J. He, G. Howard, F. Hu, L. Inker, G. Karthikeyan, N. Kassebaum, W. Koroshetz, C. Lavie, D. Lloyd-Jones, H. S. Lu, A. Mirijello, A. M. Temesgen, A. Mokdad, A. E. Moran, P. Muntner, J. Narula, B. Neal, M. Ntsekhe, G. Moraes de Oliveira, C. Otto, M. Owolabi, M. Pratt, S. Rajagopalan, M. Reitsma, A. L. P. Ribeiro, N. Rigotti, A. Rodgers, C. Sable, S. Shakil, K. Sliwa-Hahnle, B. Stark, J. Sundström, P. Timpel, I. M. Tleyjeh, M. Valgimigli, T. Vos, P. K. Whelton, M. Yacoub, L. Zuhlke, C. Murray, V. Fuster, G. A. Roth, G. A. Mensah, C. O. Johnson, G. Addolorato, E. Ammirati, L. M. Baddour, N. C. Barengo, A. Beaton, E. J. Benjamin, C. P. Benziger, A. Bonny, M. Brauer, M. Brodmann, T. J. Cahill, J. R. Carapetis, A. L. Catapano, S. Chugh, L. T. Cooper, J. Coresh, M. H. Criqui, N. K. DeCleene, K. A. Eagle, S. Emmons-Bell, V. L. Feigin, J. Fernández-Sola, F. G. R. Fowkes, E. Gakidou, S. M. Grundy, F. J. He, G. Howard, F. Hu, L. Inker, G. Karthikeyan, N. J. Kassebaum, W. J. Koroshetz, C. Lavie, D. Lloyd-Jones, H. S. Lu, A. Mirijello, A. T. Misganaw, A. H. Mokdad, A. E. Moran, P. Muntner, J. Narula, B. Neal, M. Ntsekhe, G. M. Oliveira, C. M. Otto, M. O. Owolabi, M. Pratt, S. Rajagopalan, M. B. Reitsma, A. L. P. Ribeiro, N. A. Rigotti, A. Rodgers, C. A. Sable, S. S. Shakil, K. Sliwa, B. A. Stark, J. Sundström, P. Timpel, I. I. Tleyjeh, M. Valgimigli, T. Vos, P. K. Whelton, M. Yacoub, L. J. Zuhlke, M. Abbasi-Kangevari, A. Abdi, A. Abedi, V. Aboyans, W. A. Abrha, E. Abu-Gharbieh, A. I. Abushouk, D. Acharya, T. Adair, O. M. Adebayo, Z. Ademi, S. M. Advani, K. Afshari, A. Afshin, G. Agarwal, P. Agasthi, S. Ahmad, S. Ahmadi, M. B. Ahmed, B. Aji, Y. Akalu, W. Akande-Sholabi, A. Aklilu, C. J. Akunna, F. Alahdab, A. Al-Eyadhy, K. F. Alhabib, S. M. Alif, V. Alipour, S. M. Aljunid, F. Alla, A. Almasi-Hashiani, S. Almustanyir, R. M. Al-Raddadi, A. K. Amegah, S. Amini, A. Aminorroaya, H. Amu, D. A. Amugsi, R. Ancuceanu, D. Anderlini, T. Andrei, C. L. Andrei, A. Ansari-Moghaddam, Z. A. Anteneh, I. C. Antonazzo, B. Antony, R. Anwer, L. T. Appiah, J. Arabloo, J. Arnlov, K. D. Artanti, Z. Ataro, M. Ausloos, L. Avila-Burgos, A. T. Awan, M. A. Awoke, H. T. Ayele, M. A. Ayza, S. Azari, D. B. B, N. Baheiraei, A. A. Baig, A. Bakhtiari, M. Banach, P. C. Banik, E. A. Baptista, M. A. Barboza, L. Barua, S. Basu, N. Bedi, Y. Béjot, D. A. Bennett, I. M. Bensenor, A. E. Berman, Y. M. Bezabih, A. S. Bhagavathula, S. Bhaskar, K. Bhattacharyya, A. Bijani, B. Bikbov, M. M. Birhanu, A. Boloor, L. C. Brant, H. Brenner, N. I. Briko, Z. A. Butt, F. L. Caetano dos Santos, L. E. Cahill, L. Cahuana-Hurtado, L. A. Camera, I. R. Campos-Nonato, C. Cantu-Brito, J. Car, J. J. Carrero, F. Carvalho, C. A. Castaneda-Orjuela, F. Catala-Lopez, E. Cerin, J. Charan, V. K. Chattu, S. Chen, K. L. Chin, J.-Y. J. Choi, D.-T. Chu, S.-C. Chung, M. Cirillo, S. Coffey, S. Conti, V. M. Costa, D. K. Cundiff, O. Dadras, B. Dagnew, X. Dai, A. A. Damasceno, L. Dandona, R. Dandona, K. Davletov, V. De la Cruz-Gongora, F. P. De la Hoz, J.-W. De Neve, E. Denova-Gutierrez, M. Derbew Molla, B. T. Derseh, R. Desai, G. Deuschl, S. D. Dharmaratne, M. Dhimal, R. R. Dhungana, M. Dianatinasab, D. Diaz, S. Djalalinia, K. Dokova, A. Douiri, B. B. Duncan, A. R. Duraes, A. W. Eagan, S. Ebtehaj, A. Eftekhari, S. Eftekharzadeh, M. Ekholuenetale, N. El Nahas, I. Y. Elgendy, M. Elhadi, S. I. El-Jaafary, S. Esteghamati, A. E. Etisso, O. Eyawo, I. Fadhil, E. J. A. Faraon, P. S.

Faris, M. Farwati, F. Farzadfar, E. Fernandes, C. Fernandez Prendes, P. Ferrara, I. Filip, F. Fischer, D. Flood, T. Fukumoto, M. M. Gad, S. Gaidhane, M. Ganji, J. Garg, A. K. Gebre, B. G. Gebregiorgis, K. Z. Gebregzabiher, G. G. Gebremeskel, L. Getacher, A. G. Obsa, A. Ghajar, A. Ghashghaee, N. Ghith, S. Giampaoli, S. A. Gilani, P. S. Gill, R. F. Gillum, E. V. Glushkova, E. V. Gnedovskaya, M. Golechha, K. B. Gonfa, A. H. Goudarzian, A. C. Goulart, J. S. Guadamuz, A. Guha, Y. Guo, R. Gupta, V. Hachinski, N. Hafezi-Nejad, T. G. Haile, R. R. Hamadeh, S. Hamidi, G. J. Hankey, A. Hargono, R. K. Hartono, M. Hashemian, A. Hashi, S. Hassan, H. Y. Hassen, R. J. Havmoeller, S. I. Hay, K. Hayat, G. Heidari, C. Herteliu, R. Holla, M. Hosseini, M. Hosseinzadeh, M. Hostiuc, S. Hostiuc, M. Househ, J. Huang, A. Humayun, I. Iavicoli, C. U. Ibeneme, S. E. Ibitoye, O. S. Ilesanmi, I. M. Ilic, M. D. Ilic, U. Iqbal, S. S. N. Irvani, S. M. S. Islam, R. M. Islam, H. Iso, M. Iwagami, V. Jain, T. Javaheri, S. K. Jayapal, S. Jayaram, R. Jayawardena, P. Jeemon, R. P. Jha, J. B. Jonas, J. Jonnagaddala, F. Joukar, J. J. Jozwiak, M. Juerisson, A. Kabir, T. Kahlon, R. Kalani, R. Kalhor, A. Kamath, I. Kamel, H. Kandel, A. Kandel, A. Karch, A. S. Kasa, P. D. Katoto, G. A. Kayode, Y. S. Khader, M. Khammarnia, M. S. Khan, M. N. Khan, M. Khan, E. A. Khan, K. Khatab, G. M. Kibria, Y. J. Kim, G. R. Kim, R. W. Kimokoti, S. Kisa, A. Kisa, M. Kivimäki, D. Kolte, A. Koolivand, V. A. Korshunov, S. L. Koulmane Laxminarayana, A. Koyanagi, K. Krishan, V. Krishnamoorthy, B. Kuate Defo, B. Kucuk Bicer, V. Kulkarni, G. A. Kumar, N. Kumar, O. P. Kurmi, D. Kusuma, G. F. Kwan, C. La Vecchia, B. Lacey, T. Lallukka, Q. Lan, S. Lasrado, Z. S. Lassi, P. Lauriola, W. R. Lawrence, A. Laxmaiah, K. E. LeGrand, M.-C. Li, B. Li, S. Li, S. S. Lim, L.-L. Lim, H. Lin, Z. Lin, R.-T. Lin, X. Liu, A. D. Lopez, S. Lorkowski, P. A. Lotufo, A. Lugo, N. K. M, F. Madotto, M. Mahmoudi, A. Majeed, R. Malekzadeh, A. A. Malik, A. A. Mamun, N. Manafi, M. A. Mansournia, L. G. Mantovani, S. Martini, M. R. Mathur, G. Mazzaglia, S. Mehata, M. M. Mehndiratta, T. Meier, R. G. Menezes, A. Meretoja, T. Mestrovic, B. Miazgowski, T. Miazgowski, I. M. Michalek, T. R. Miller, E. M. Mirrakhimov, H. Mirzaei, B. Moazen, M. Moghadaszadeh, Y. Mohammad, D. K. Mohammad, S. Mohammed, M. A. Mohammed, Y. Mokhayeri, M. Molokhia, A. A. Montasir, G. Moradi, R. Moradzadeh, P. Moraga, L. Morawska, I. Moreno Velasquez, J. Morze, S. Mubarik, W. Muruet, K. I. Musa, A. J. Nagarajan, M. Nalini, V. Nangia, A. A. Naqvi, S. Narasimha Swamy, B. R. Nascimento, V. C. Nayak, J. Nazari, M. Nazarzadeh, R. I. Negoi, S. Neupane Kandel, H. L. Nguyen, M. R. Nixon, B. Norrving, J. J. Noubiap, B. E. Nouthe, C. Nowak, O. O. Odukoya, F. A. Ogbo, A. T. Olagunju, H. Orru, A. Ortiz, S. M. Ostroff, J. R. Padubidri, R. Palladino, A. Pana, S. Panda-Jonas, U. Parekh, E.-C. Park, M. Parvizi, F. Pashazadeh Kan, U. K. Patel, M. Pathak, R. Paudel, V. C. F. Pepito, A. Perianayagam, N. Perico, H. Q. Pham, T. Pilgrim, M. A. Piradov, F. Pishgar, V. Podder, R. V. Polibin, A. Pourshams, D. R. Pribadi, N. Rabiee, M. Rabiee, A. Radfar, A. Rafiei, F. Rahim, V. Rahimi-Movaghar, M. H. Ur Rahman, M. A. Rahman, A. M. Rahmani, I. Rakovac, P. Ram, S. Ramalingam, J. Rana, P. Ranasinghe, S. J. Rao, P. Rathi, L. Rawal, W. F. Rawasia, R. Rawassizadeh, G. Remuzzi, A. M. Renzaho, A. Rezapour, S. M. Riahi, R. L. Roberts-Thomson, L. Roever, P. Rohloff, M. Romoli, G. Roshandel, G. M. Rwegerera, S. Saadatagah, M. M. Saber-Ayad, S. Sabour, S. Sacco, M. Sadeghi, S. Saeedi Moghaddam, S. Safari, A. Sahebkar, S. Salehi, H. Salimzadeh, M. Samaei, A. M. Samy, I. S. Santos, M. M. Santric-Milicevic, N. Sarrafzadegan, A. Sarveazad, T. Sathish, M. Sawhney, M. Saylan, M. I. Schmidt, A. E. Schutte, S. Senthilkumaran, S. G. Sepanlou, F. Sha, S. Shahabi, I. Shahid, M. A. Shaikh, M. Shamali, M. Shamsizadeh, M. S. R. Shawon, A. Sheikh, M. Shigematsu, M.-J. Shin, J. I. Shin, R. Shiri, I. Shiue, K. Shuval, S. Siabani, T. J. Siddiqi, D. A. Silva, J. A. Singh, A. S. Mtech, V. Y. Skryabin, A. A. Skryabina, A. Soheili, E. E. Spurlock, L. Stockfelt, S. Stortecky, S. Stranges, R. Suliankatchi Abdulkader, H. Tadbiri, E. G. Tadesse, D. B. Tadesse, M. Tajdini, M. Tariqujjaman, B. F. Teklehaimanot, M.-H. Temsah, A. K. Tesema, B. Thakur, K. R. Thankappan, R. Thapar, A. G. Thrift, B. Timalsina, M. Tonelli, M. Touvier, M. R. Tovani-Palone, A. Tripathi, J. P. Tripathy, T. C. Truelsen, G. M. Tsegay, G. W. Tsegaye, N. Tsilimparis, B. S. Tusa, S. Tyrovolas, K. K. Umapathi, B. Unim, B. Unnikrishnan, M. S. Usman, M. Vaduganathan, P. R. Valdez, T. J. Vasankari, D. Z. Velazquez, N. Venketasubramanian, G. T. Vu, I. S. Vujcic, Y. Waheed, Y. Wang, F. Wang, J. Wei, R. G. Weintraub, A. H. Weldemariam, R. Westerman, A. S. Winkler,

C. S. Wiysonge, C. D. Wolfe, B. L. Wubishet, G. Xu, A. Yadollahpour, K. Yamagishi, L. L. Yan, S. Yandrapalli, Y. Yano, H. Yatsuya, T. Y. Yeheyis, Y. Yeshaw, C. S. Yilgwan, N. Yonemoto, C. Yu, H. Yusefzadeh, G. Zachariah, S. B. Zaman, M. S. Zaman, M. Zamanian, R. Zand, A. Zandifar, A. Zarghi, M. S. Zastrozhin, A. Zastrozhina, Z.-J. Zhang, Y. Zhang, W. Zhang, C. Zhong, Z. Zou, Y. M. H. Zuniga, C. J. Murray, and V. Fuster. **Global Burden of Cardiovascular Diseases and Risk Factors, 1990–2019**. *Journal of the American College of Cardiology*, **76**(25):2982–3021, dec 2020. doi:10.1016/j.jacc.2020.11.010.

[2] D. S. Celermajer, C. K. Chow, E. Marijon, N. M. Anstey, and K. S. Woo. **Cardiovascular Disease in the Developing World**. *Journal of the American College of Cardiology*, **60**(14):1207–1216, oct 2012. doi:10.1016/j.jacc.2012.03.074.

[3] Q. Counseller and Y. Aboelkassem. **Recent technologies in cardiac imaging**. *Frontiers in Medical Technology*, **4**(January):1–17, jan 2023. doi:10.3389/fmedt.2022.984492.

[4] R. Guo, S. Weingärtner, P. Šiurytė, C. T. Stoeck, M. Füetterer, A. E. Campbell-Washburn, A. Suinesiaputra, M. Jerosch-Herold, and R. Nezafat. **Emerging Techniques in Cardiac Magnetic Resonance Imaging**. *Journal of Magnetic Resonance Imaging*, **55**(4):1043–1059, 2022. doi:10.1002/jmri.27848.

[5] E. Aherne, K. Chow, and J. Carr. **Cardiac T 1 mapping: Techniques and applications**. *Journal of Magnetic Resonance Imaging*, **51**(5):1336–1356, may 2020. doi:10.1002/jmri.26866.

[6] E. B. Schelbert and D. R. Messroghli. **State of the Art: Clinical Applications of Cardiac T1 Mapping.** *Radiology*, **278**(3):658–76, mar 2016. doi:10.1148/radiol.2016141802.

[7] A. Seraphim, K. D. Knott, J. Augusto, A. N. Bhuva, C. Manisty, and J. C. Moon. **Quantitative cardiac MRI**. *Journal of Magnetic Resonance Imaging*, **51**(3):693–711, mar 2020. doi:10.1002/jmri.26789.

[8] A. C. Ogier, A. Bustin, H. Cochet, J. Schwitter, and R. B. van Heeswijk. **The Road Toward Reproducibility of Parametric Mapping of the Heart: A Technical Review**. *Frontiers in Cardiovascular Medicine*, **9**(May):1–15, may 2022. doi:10.3389/fcvm.2022.876475.

[9] V. M. Ferreira, S. K. Piechnik, E. Dall'Armellina, T. D. Karamitsos, J. M. Francis, R. P. Choudhury, M. G. Friedrich, M. D. Robson, and S. Neubauer. **Non-contrast T1-mapping detects acute myocardial edema with high diagnostic accuracy: a comparison to T2-weighted cardiovascular magnetic resonance**. *Journal of Cardiovascular Magnetic Resonance*, **14**(1):42, dec 2012. doi:10.1186/1532-429X-14-42.

[10] S. Dass, J. J. Suttie, S. K. Piechnik, V. M. Ferreira, C. J. Holloway, R. Banerjee, M. Mahmod, L. Cochlin, T. D. Karamitsos, M. D. Robson, H. Watkins, and S. Neubauer. **Myocardial Tissue Characterization Using Magnetic Resonance Noncontrast T1 Mapping in Hypertrophic and Dilated Cardiomyopathy**. *Circulation: Cardiovascular Imaging*, **5**(6):726–733, nov 2012. doi:10.1161/CIRCIMAGING.112.976738.

[11] T. D. Karamitsos, S. K. Piechnik, S. M. Banypersad, M. Fontana, N. B. Ntusi, V. M. Ferreira, C. J. Whelan, S. G. Myerson, M. D. Robson, P. N. Hawkins, S. Neubauer, and J. C. Moon. **Noncontrast T1 Mapping for the Diagnosis of Cardiac Amyloidosis**. *JACC: Cardiovascular Imaging*, **6**(4):488–497, apr 2013. doi:10.1016/j.jcmg.2012.11.013.

[12] M. Hedley and H. Yan. **Motion artifact suppression: A review of post-processing techniques**. *Magnetic Resonance Imaging*, **10**(4):627–635, jan 1992. doi:10.1016/0730-725X(92)90014-Q.

[13] R. Obuchowicz, A. Piórkowski, A. Urbanik, and M. Strzelecki. **Influence of Acquisition Time on MR Image Quality Estimated with Nonparametric Measures Based on Texture Features**. *BioMed Research International*, **2019**:1–10, nov 2019. doi:10.1155/2019/3706581.

[14] P. Kellman and M. S. Hansen. **T1-mapping in the heart: accuracy and precision**. *Journal of Cardiovascular Magnetic Resonance*, **16**(1):2, dec 2014. doi:10.1186/1532-429X-16-2.

[15] D. R. Messroghli, J. C. Moon, V. M. Ferreira, L. Grosse-Wortmann, T. He, P. Kellman, J. Mascherbauer, R. Nezafat, M. Salerno, E. B. Schelbert, A. J. Taylor, R. Thompson, M. Ugander, R. B. van Heeswijk, and M. G. Friedrich. **Clinical recommendations for cardiovascular magnetic resonance mapping of T1, T2, T2* and extracellular volume: A consensus statement by the Society for Cardiovascular Magnetic Resonance (SCMR) endorsed by the European Association for Cardiovascular Imagi**. *Journal of Cardiovascular Magnetic Resonance*, **19**(1):75, dec 2017. doi:10.1186/s12968-017-0389-8.

[16] C. Hu, A. J. Sinusas, S. Huber, S. Thorn, M. R. Stacy, H. Mojibian, and D. C. Peters. **T1-refBlochi: high resolution 3D post-contrast T1 myocardial mapping based on a single 3D late gadolinium enhancement volume, Bloch equations, and a reference T1**. *Journal of Cardiovascular Magnetic Resonance*, **19**(1):63, dec 2017. doi:10.1186/s12968-017-0375-1.

[17] G. Milotta, A. Bustin, O. Jaubert, R. Neji, C. Prieto, and R. M. Botnar. **3D whole-heart isotropic-resolution motion-compensated joint T 1 /T 2 mapping and water/fat imaging**. *Magnetic Resonance in Medicine*, **84**(6):3009–3026, dec 2020. doi:10.1002/mrm.28330.

[18] G. Nordio, T. Schneider, G. Cruz, T. Correia, A. Bustin, C. Prieto, R. M. Botnar, and M. Henningsson. **Whole-heart T 1 mapping using a 2D fat image navigator for respiratory motion compensation**. *Magnetic Resonance in Medicine*, **83**(1):178–187, jan 2020. doi:10.1002/mrm.27919.

[19] A. Phair, G. Cruz, H. Qi, R. M. Botnar, and C. Prieto. **Free-running 3D whole-heart T 1 and T 2 mapping and cine MRI using low-rank reconstruction with non-rigid cardiac motion correction**. *Magnetic Resonance in Medicine*, **89**(1):217–232, jan 2023. doi:10.1002/mrm.29449.

[20] H. Qi, A. Bustin, G. Cruz, O. Jaubert, H. Chen, R. M. Botnar, and C. Prieto. **Free-running simultaneous myocardial T1/T2 mapping and cine imaging with 3D whole-heart coverage and isotropic spatial resolution**. *Magnetic Resonance Imaging*, **63**:159–169, nov 2019. doi:10.1016/j.mri.2019.08.008.

[21] H. Qi, A. Bustin, T. Kuestner, R. Hajhosseiny, G. Cruz, K. Kunze, R. Neji, R. M. Botnar, and C. Prieto. **Respiratory motion-compensated high-resolution 3D whole-heart T1ρ mapping**. *Journal of Cardiovascular Magnetic Resonance*, **22**(1):12, dec 2020. doi:10.1186/s12968-020-0597-5.

[22] H. Qi, O. Jaubert, A. Bustin, G. Cruz, H. Chen, R. Botnar, and C. Prieto. **Free-running 3D whole heart myocardial T 1 mapping with isotropic spatial resolution**. *Magnetic Resonance in Medicine*, **82**(4):1331–1342, oct 2019. doi:10.1002/mrm.27811.

[23] H. Qi, Z. Lv, J. Hu, J. Xu, R. Botnar, C. Prieto, and P. Hu. **Accelerated 3D free-breathing high-resolution myocardial T1ρ mapping at 3 Tesla**. *Magnetic Resonance in Medicine*, **88**(6):2520–2531, 2022. doi:10.1002/mrm.29417.

[24] J. Gordon Betts, P. Desaix, E. W. Johnson, J. E. Johnson, O. Korol, D. Kruse, B. Poe, J. Wise, M. D. Womble, and K. A. Young. *Anatomy and physiology*. OpenStax College, Rice University, Houston, 2022.

[25] P. Bhadoria, K. Bisht, B. Singh, and V. Tiwari. **Cadaveric Study on the Morphology and Morphometry of Heart Papillary Muscles**. *Cureus*, **i**(2):1–13, feb 2022. doi:10.7759/cureus.22722.

[26] L. Axel. **Papillary Muscles Do Not Attach Directly to the Solid Heart Wall**. *Circulation*, **109**(25):3145–3148, jun 2004. doi:10.1161/01.CIR.0000134276.06719.F3.

[27] J. Walpot, D. Juneau, S. Massalha, G. Dwivedi, F. J. Rybicki, B. J. Chow, and J. R. Inácio. **Left Ventricular Mid-Diastolic Wall Thickness: Normal Values for Coronary CT Angiography**. *Radiology: Cardiothoracic Imaging*, **1**(5):e190034, dec 2019. doi:10.1148/ryct.2019190034.

[28] R. M. Lang, M. Bierig, R. B. Devereux, F. A. Flachskampf, E. Foster, P. A. Pellikka, M. H. Picard, M. J. Roman, J. Seward, J. Shanewise, S. Solomon, K. T. Spencer, M. St. John Sutton, and W. Stewart. **Recommendations for chamber quantification**. *European Journal of Echocardiography*, **7**(2):79–108, 2006. doi:10.1016/j.euje.2005.12.014.

[29] M. Varela, R. Morgan, A. Theron, D. Dillon-Murphy, H. Chubb, J. Whitaker, M. Henningsson, P. Aljabar, T. Schaeffter, C. Kolbitsch, and O. V. Aslanidi. **Novel MRI Technique Enables Non-Invasive Measurement of Atrial Wall Thickness**. *IEEE Transactions on Medical Imaging*, **36**(8):1607–1614, aug 2017. doi:10.1109/TMI.2017.2671839.

[30] J. Schulz-Menger, D. A. Bluemke, J. Bremerich, S. D. Flamm, M. A. Fogel, M. G. Friedrich, R. J. Kim, F. von Knobelsdorff-Brenkenhoff, C. M. Kramer, D. J. Pennell, S. Plein, and E. Nagel. **Standardized image interpretation and post-processing in cardiovascular magnetic resonance - 2020 update**. *Journal of Cardiovascular Magnetic Resonance*, **22**(1):19, dec 2020. doi:10.1186/s12968-020-00610-6.

[31] N. Galea, I. Carbone, D. Cannata, G. Cannavale, B. Conti, R. Galea, A. Frustaci, C. Catalano, and M. Francone. **Right ventricular cardiovascular magnetic resonance imaging: normal anatomy and spectrum of pathological findings**. *Insights into Imaging*, **4**(2):213–223, apr 2013. doi:10.1007/s13244-013-0222-3.

[32] R. Asano, T. Ogo, Y. Morita, A. Kotoku, T. Aoki, K. Hirakawa, S. Nakayama, J. Ueda, A. Tsuji, M. T. Waddingham, Y. Ohta, T. Fukuda, K. Ohta-Ogo, H. Ishibashi-Ueda, T. Noguchi, and S. Yasuda. **Prognostic value of right ventricular native T1 mapping in pulmonary arterial hypertension**. *PLOS ONE*, **16**(11):e0260456, nov 2021. doi:10.1371/journal.pone.0260456.

[33] W. J. McKenna, G. Thiene, A. Nava, F. Fontaliran, C. Blomstrom-Lundqvist, G. Fontaine, and F. Camerini. **Diagnosis of arrhythmogenic right ventricular dysplasia/cardiomyopathy. Task Force of the Working Group Myocardial and Pericardial Disease of the European Society of Cardiology and of the Scientific Council on Cardiomyopathies of the International Society**. *Heart*, **71**(3):215–218, mar 1994. doi:10.1136/hrt.71.3.215.

[34] P. Gal and N. F. Marrouche. **Magnetic resonance imaging of atrial fibrosis: redefining atrial fibrillation to a syndrome**. *European Heart Journal*, **38**(1):14–19, jan 2017. doi:10.1093/eurheartj/ehv514.

[35] E. Appelbaum and W. J. Manning. **Left Atrial Fibrosis by Late Gadolinium Enhancement Cardiovascular Magnetic Resonance Predicts Recurrence of Atrial Fibrillation After Pulmonary Vein Isolation**. *Circulation: Arrhythmia and Electrophysiology*, **7**(1):2–4, feb 2014. doi:10.1161/CIRCEP.114.001354.

[36] T. Leiner, J. Bogaert, M. G. Friedrich, R. Mohiaddin, V. Muthurangu, S. Myerson, A. J. Powell, S. V. Raman, and D. J. Pennell. **SCMR Position Paper (2020) on clinical indications for cardiovascular magnetic resonance**. *Journal of Cardiovascular Magnetic Resonance*, **22**(1):76, dec 2020. doi:10.1186/s12968-020-00682-4.

[37] A. Krasnobaev and A. Sozykin. **An Overview of Techniques for Cardiac Left Ventricle Segmentation on Short-Axis MRI**. *ITM Web of Conferences*, **8**:01003, nov 2016. doi:10.1051/itmconf/20160801003.

[38] H. Childs, L. Ma, M. Ma, J. Clarke, M. Cocker, J. Green, O. Strohm, and M. G. Friedrich. **Comparison of long and short axis quantification of left ventricular volume parameters by cardiovascular magnetic resonance, with ex-vivo validation**. *Journal of Cardiovascular Magnetic Resonance*, **13**(1):40, dec 2011. doi:10.1186/1532-429X-13-40.

[39] A. A. Kirkham, M. V. Goonasekera, B. C. Mattiello, J. G. Grenier, M. J. Haykowsky, and R. B. Thompson. **Reliability and reproducibility of cardiac MRI quantification of**

peak exercise function with long-Axis views. *PLoS ONE*, **16**(2 February):1–12, 2021. doi:10.1371/journal.pone.0245912.

[40] T. N. Bloomer, S. Plein, A. Radjenovic, D. M. Higgins, T. R. Jones, J. P. Ridgway, and M. U. Sivananthan. **Cine MRI using steady state free precession in the radial long axis orientation is a fast accurate method for obtaining volumetric data of the left ventricle**. *Journal of Magnetic Resonance Imaging*, **14**(6):685–692, dec 2001. doi:10.1002/jmri.10019.

[41] P. Haaf, P. Garg, D. R. Messroghli, D. A. Broadbent, J. P. Greenwood, and S. Plein. **Cardiac T1 Mapping and Extracellular Volume (ECV) in clinical practice: a comprehensive review**. *Journal of Cardiovascular Magnetic Resonance*, **18**(1):89, jan 2017. doi:10.1186/s12968-016-0308-4.

[42] N. Al-Wakeel-Marquard, F. Seidel, C. Herbst, J. Kühnisch, T. Kuehne, F. Berger, S. Klaassen, and D. R. Messroghli. **Diffuse myocardial fibrosis by T1 mapping is associated with heart failure in pediatric primary dilated cardiomyopathy**. *International Journal of Cardiology*, **333**:219–225, jun 2021. doi:10.1016/j.ijcard.2021.03.023.

[43] P. Garg. **Role of Cardiac T1 Mapping and Extracellular Volume (ECV) in the Assessment of Myocardial Infarction**. *The Anatolian Journal of Cardiology*, **19**(6):404–411, 2018. doi:10.14744/AnatolJCardiol.2018.39586.

[44] D. R. Messroghli, A. Radjenovic, S. Kozerke, D. M. Higgins, M. U. Sivananthan, and J. P. Ridgway. **Modified Look-Locker inversion recovery (MOLLI) for high-resolutionT1 mapping of the heart**. *Magnetic Resonance in Medicine*, **52**(1):141–146, jul 2004. doi:10.1002/mrm.20110.

[45] S. K. Piechnik, V. M. Ferreira, E. Dall'Armellina, L. E. Cochlin, A. Greiser, S. Neubauer, and M. D. Robson. **Shortened Modified Look-Locker Inversion recovery (ShMOLLI) for clinical myocardial T1-mapping at 1.5 and 3 T within a 9 heartbeat breathhold**. *Journal of Cardiovascular Magnetic Resonance*, **12**(1):69, dec 2010. doi:10.1186/1532-429X-12-69.

[46] K. Chow, J. A. Flewitt, J. D. Green, J. J. Pagano, M. G. Friedrich, and R. B. Thompson. **Saturation recovery single-shot acquisition (SASHA) for myocardial T 1 mapping**. *Magnetic Resonance in Medicine*, **71**(6):2082–2095, jun 2014. doi:10.1002/mrm.24878.

[47] S. Weingärtner, M. Akçakaya, T. Basha, K. V. Kissinger, B. Goddu, S. Berg, W. J. Manning, and R. Nezafat. **Combined saturation/inversion recovery sequences for improved evaluation of scar and diffuse fibrosis in patients with arrhythmia or heart rate variability**. *Magnetic Resonance in Medicine*, **71**(3):1024–1034, mar 2014. doi:10.1002/mrm.24761.

[48] H. Y. Carr. **Steady-State Free Precession in Nuclear Magnetic Resonance**. *Physical Review*, **112**(5):1693–1701, dec 1958. doi:10.1103/PhysRev.112.1693.

[49] R. Deichmann and A. Haase. **Quantification of T1 values by SNAPSHOT-FLASH NMR imaging**. *Journal of Magnetic Resonance (1969)*, **96**(3):608–612, feb 1992. doi:10.1016/0022-2364(92)90347-A.

[50] N. D. Gai, C. Stehning, M. Nacif, and D. A. Bluemke. **Modified Look-Locker T 1 evaluation using Bloch simulations: Human and phantom validation**. *Magnetic Resonance in Medicine*, **69**(2):329–336, feb 2013. doi:10.1002/mrm.24251.

[51] M. D. Robson, S. K. Piechnik, E. M. Tunnicliffe, and S. Neubauer. **T 1 measurements in the human myocardium: The effects of magnetization transfer on the SASHA and MOLLI sequences**. *Magnetic Resonance in Medicine*, **70**(3):664–670, sep 2013. doi:10.1002/mrm.24867.

[52] P. Kellman, D. A. Herzka, A. E. Arai, and M. S. Hansen. **Influence of Off-resonance in myocardial T1-mapping using SSFP based MOLLI method**. *Journal of Cardiovascular Magnetic Resonance*, **15**(1):63, dec 2013. doi:10.1186/1532-429X-15-63.

[53] K. M. Kerkering, J. Schulz-Menger, T. Schaeffter, and C. Kolbitsch. **Motion-corrected model-based reconstruction for 2D myocardial T1 mapping**. *Magnetic Resonance in Medicine*, **90**(3):1086–1100, sep 2023. doi:10.1002/mrm.29699.

[54] K. M. Becker, J. Schulz-Menger, T. Schaeffter, and C. Kolbitsch. **Simultaneous high-resolution cardiac T 1 mapping and cine imaging using model-based iterative image reconstruction**. *Magnetic Resonance in Medicine*, **81**(2):1080–1091, feb 2019. doi:10.1002/mrm.27474.

[55] K. M. Becker, E. Blaszczyk, S. Funk, A. Nuesslein, J. Schulz-Menger, T. Schaeffter, and C. Kolbitsch. **Fast myocardial T 1 mapping using cardiac motion correction**. *Magnetic Resonance in Medicine*, **83**(2):438–451, feb 2020. doi:10.1002/mrm.27935.

[56] R. P. Lewis, S. E. Rittogers, W. F. Froester, and H. Boudoulas. **A critical review of the systolic time intervals.** *Circulation*, **56**(2):146–158, aug 1977. doi:10.1161/01.CIR.56.2.146.

[57] J. Ludwig, P. Speier, F. Seifert, T. Schaeffter, and C. Kolbitsch. **Pilot tone–based motion correction for prospective respiratory compensated cardiac cine MRI**. *Magnetic Resonance in Medicine*, **85**(5):2403–2416, may 2021. doi:10.1002/mrm.28580.

[58] G. Nordio, A. Bustin, M. Henningsson, I. Rashid, A. Chiribiri, T. Ismail, F. Odille, C. Prieto, and R. M. Botnar. **3D SASHA myocardial T1 mapping with high accuracy and improved precision**. *Magnetic Resonance Materials in Physics, Biology and Medicine*, **32**(2):281–289, apr 2019. doi:10.1007/s10334-018-0703-y.

[59] E. Plenge, D. H. J. Poot, M. Bernsen, G. Kotek, G. Houston, P. Wielopolski, L. van der Weerd, W. J. Niessen, and E. Meijering. **Super-resolution methods in MRI: Can they improve the trade-off between resolution, signal-to-noise ratio, and acquisition time?** *Magnetic Resonance in Medicine*, **68**(6):1983–1993, dec 2012. doi:10.1002/mrm.24187.

[60] D. W. McRobbie, E. A. Moore, M. J. Graves, and M. R. Prince. *MRI from Picture to Proton*. Cambridge University Press, sep 2006. doi:10.1017/CBO9780511545405.

[61] S. Kim, N. Bose, and H. Valenzuela. **Recursive reconstruction of high resolution image from noisy undersampled multiframes**. *IEEE Transactions on Acoustics, Speech, and Signal Processing*, **38**(6):1013–1027, jun 1990. doi:10.1109/29.56062.

[62] M. Irani and S. Peleg. **Improving resolution by image registration**. *CVGIP: Graphical Models and Image Processing*, **53**(3):231–239, may 1991. doi:10.1016/1049-9652(91)90045-L.

[63] M. Irani and S. Peleg. **Motion Analysis for Image Enhancement: Resolution, Occlusion, and Transparency**. *Journal of Visual Communication and Image Representation*, **4**(4):324–335, dec 1993. doi:10.1006/jvci.1993.1030.

[64] E. Van Reeth, I. W. K. Tham, C. H. Tan, and C. L. Poh. **Super-resolution in magnetic resonance imaging: A review**. *Concepts in Magnetic Resonance Part A*, **40A**(6):306–325, nov 2012. doi:10.1002/cmr.a.21249.

[65] S. Peled and Y. Yeshurun. **Superresolution in MRI: Application to human white matter fiber tract visualization by diffusion tensor imaging**. *Magnetic Resonance in Medicine*, **45**(1):29–35, jan 2001. doi:10.1002/1522-2594(200101)45:1<29::AID-MRM1005>3.0.CO;2-Z.

[66] Q. M. Tieng, G. J. Cowin, D. C. Reutens, G. J. Galloway, and V. Vegh. **MRI resolution enhancement: How useful are shifted images obtained by changing the demodulation frequency?** *Magnetic Resonance in Medicine*, **65**(3):664–672, mar 2011. doi:10.1002/mrm.22653.

[67] K. Scheffler. **Superresolution in MRI?** *Magnetic Resonance in Medicine*, **48**(2):408–408, aug 2002. doi:10.1002/mrm.10203.

[68] H. Greenspan, G. Oz, N. Kiryati, and S. Peled. **MRI inter-slice reconstruction using super-resolution**. *Magnetic Resonance Imaging*, **20**(5):437–446, jun 2002. doi:10.1016/S0730-725X(02)00511-8.

[69] M. Uecker, T. J. Sumpf, and J. Frahm. **Reply to: MRI resolution enhancement: How useful are shifted images obtained by changing the demodulation frequency?** *Magnetic Resonance in Medicine*, **66**(6):1511–1512, dec 2011. doi:10.1002/mrm.22989.

[70] M. L. de Leeuw den Bouter, G. Ippolito, T. P. A. O'Reilly, R. F. Remis, M. B. van Gijzen, and A. G. Webb. **Deep learning-based single image super-resolution for low-field MR brain images**. *Scientific Reports*, **12**(1):6362, apr 2022. doi:10.1038/s41598-022-10298-6.

[71] Z. Wang, J. Chen, and S. C. Hoi. **Deep Learning for Image Super-Resolution: A Survey**. *IEEE Transactions on Pattern Analysis and Machine Intelligence*, **43**(10):3365–3387, 2021. doi:10.1109/TPAMI.2020.2982166.

[72] H. Gudbjartsson and S. Patz. **The rician distribution of noisy mri data**. *Magnetic Resonance in Medicine*, **34**(6):910–914, dec 1995. doi:10.1002/mrm.1910340618.

[73] M. Payne, I. Mali, T. Mueller, M. Cain, R. Segev, and S. H. Bossmann. **Super-resolution reconstruction in ultrahigh-field MRI**. *Biophysical Reports*, **3**(2):100107, jun 2023. doi:10.1016/j.bpr.2023.100107.

[74] A. Ben-Ezra, H. Greenspan, and Y. Rubner. **Regularized super-resolution of brain MRI**. In *2009 IEEE International Symposium on Biomedical Imaging: From Nano to Macro*, number 1, pages 254–257. IEEE, jun 2009. doi:10.1109/ISBI.2009.5193032.

[75] M. Kuklisova-Murgasova, G. Quaghebeur, M. A. Rutherford, J. V. Hajnal, and J. A. Schnabel. **Reconstruction of fetal brain MRI with intensity matching and complete outlier removal**. *Medical Image Analysis*, **16**(8):1550–1564, dec 2012. doi:10.1016/j.media.2012.07.004.

[76] O. Dzyubachyk, Q. Tao, D. H. J. Poot, H. Lamb, K. Zeppenfeld, B. P. F. Lelieveldt, and R. J. van der Geest. **Improved Myocardial Scar Characterization by Super-Resolution Reconstruction in Late Gadolinium Enhanced MRI**. pages 147–154. 2013. doi:10.1007/978-3-642-40760-4_19.

[77] H. Lajous, T. Hilbert, C. W. Roy, S. Tourbier, P. de Dumast, T. Yu, J.-P. Thiran, J.-B. Ledoux, D. Piccini, P. Hagmann, R. Meuli, T. Kober, M. Stuber, R. B. van Heeswijk, and M. Bach Cuadra. **T2 Mapping from Super-Resolution-Reconstructed Clinical Fast Spin Echo Magnetic Resonance Acquisitions**. In *Lecture Notes in Computer Science (including subseries Lecture Notes in Artificial Intelligence and Lecture Notes in Bioinformatics)*, **12262 LNCS**, pages 114–124. 2020. doi:10.1007/978-3-030-59713-9_12.

[78] F. Odille, A. Bustin, B. Chen, P.-A. Vuissoz, and J. Felblinger. **Motion-Corrected, Super-Resolution Reconstruction for High-Resolution 3D Cardiac Cine MRI**. In *Lecture Notes in Computer Science (including subseries Lecture Notes in Artificial Intelligence and Lecture Notes in Bioinformatics)*, **9351**, pages 435–442. 2015. doi:10.1007/978-3-319-24574-4_52.

[79] S. u. Rahman and S. Wesarg. **Combining short-axis and long-axis cardiac MR images by applying a super-resolution reconstruction algorithm**. In B. M. Dawant and D. R. Haynor, editors, *Medical Imaging 2010: Image Processing*, **7623**, page 76230I, mar 2010. doi:10.1117/12.844356.

[80] S. ur Rahman and S. Wesarg. **Upsampling of cardiac MR images: Comparison of averaging and super-resolution for the combination of multiple views**. In *Proceedings of the 10th IEEE International Conference on Information Technology and Applications in Biomedicine*, **10**, pages 1–4. IEEE, nov 2010. doi:10.1109/ITAB.2010.5687693.

[81] J. F. Amerom, D. F. Lloyd, M. Deprez, A. N. Price, S. J. Malik, K. Pushparajah, M. P. Poppel, M. A. Rutherford, R. Razavi, and J. V. Hajnal. **Fetal whole-heart 4D imaging using motion-corrected multi-planar real-time MRI**. *Magnetic Resonance in Medicine*, **82**(3):mrm.27798, may 2019. doi:10.1002/mrm.27798.

[82] S. C. L. Deoni, J. O'Muircheartaigh, E. Ljungberg, M. Huentelman, and S. C. R. Williams. **Simultaneous high-resolution T 2 -weighted imaging and quantitative T 2 mapping at low magnetic field strengths using a multiple TE and multi-orientation acquisition approach**. *Magnetic Resonance in Medicine*, **88**(3):1273–1281, sep 2022. doi:10.1002/mrm.29273.

[83] O. Dzyubachyk, Q. Tao, D. H. Poot, H. J. Lamb, K. Zeppenfeld, B. P. Lelieveldt, and R. J. van der Geest. **Super-resolution reconstruction of late gadolinium-enhanced MRI for improved myocardial scar assessment**. *Journal of Magnetic Resonance Imaging*, **42**(1):160–167, jul 2015. doi:10.1002/jmri.24759.

[84] Q. Beirinckx, G. Ramos-Llordén, B. Jeurissen, D. H. Poot, P. M. Parizel, M. Verhoye, J. Sijbers, and A. J. den Dekker. **Joint Maximum Likelihood Estimation of Motion and T1 Parameters from Magnetic Resonance Images in a Super-resolution Framework: a Simulation Study**. *Fundamenta Informaticae*, **172**(2):105–128, feb 2020. doi:10.3233/FI-2020-1896.

[85] Q. Beirinckx, B. Jeurissen, M. Nicastro, D. H. Poot, M. Verhoye, A. J. D. Dekker, and J. Sijbers. **Model-based super-resolution reconstruction with joint motion estimation for improved quantitative MRI parameter mapping**. *Computerized Medical Imaging and Graphics*, **100**(November 2021):102071, sep 2022. doi:10.1016/j.compmedimag.2022.102071.

[86] A. A. Hefnawy. **An efficient super-resolution approach for obtaining isotropic 3-D imaging using 2-D multi-slice MRI**. *Egyptian Informatics Journal*, **14**(2):117–123, jul 2013. doi:10.1016/j.eij.2013.03.003.

[87] R. Shilling, M. Brummer, and K. Mewes. **Merging Multiple Stacks MRI Into a Single Data Volume**. In *3rd IEEE International Symposium on Biomedical Imaging: Macro to Nano, 2006.*, **2006**, pages 1012–1015. IEEE, 2006. doi:10.1109/ISBI.2006.1625092.

[88] G. Van Steenkiste, D. H. J. Poot, B. Jeurissen, A. J. den Dekker, F. Vanhevel, P. M. Parizel, and J. Sijbers. **Super-resolution T 1 estimation: Quantitative high resolution T 1 mapping from a set of low resolution T 1 -weighted images with different slice orientations**. *Magnetic Resonance in Medicine*, **77**(5):1818–1830, may 2017. doi:10.1002/mrm.26262.

[89] M. Ebner, G. Wang, W. Li, M. Aertsen, P. A. Patel, R. Aughwane, A. Melbourne, T. Doel, S. Dymarkowski, P. De Coppi, A. L. David, J. Deprest, S. Ourselin, and T. Vercauteren. **An automated framework for localization, segmentation and super-resolution reconstruction of fetal brain MRI**. *NeuroImage*, **206**(May 2019):116324, feb 2020. doi:10.1016/j.neuroimage.2019.116324.

[90] A. Gholipour, J. A. Estroff, and S. K. Warfield. **Robust Super-Resolution Volume Reconstruction From Slice Acquisitions: Application to Fetal Brain MRI**. *IEEE Transactions on Medical Imaging*, **29**(10):1739–1758, oct 2010. doi:10.1109/TMI.2010.2051680.

[91] B. Kainz, M. Steinberger, W. Wein, M. Kuklisova-Murgasova, C. Malamateniou, K. Keraudren, T. Torsney-Weir, M. Rutherford, P. Aljabar, J. V. Hajnal, and D. Rueckert. **Fast Volume Reconstruction From Motion Corrupted Stacks of 2D Slices**. *IEEE Transactions on Medical Imaging*, **34**(9):1901–1913, sep 2015. doi:10.1109/TMI.2015.2415453.

[92] A.-L. Le Bars, K. Moulin, D. B. Ennis, J. Felblinger, B. Chen, and F. Odille. **In Vivo Super-Resolution Cardiac Diffusion Tensor MRI: A Feasibility Study**. *Diagnostics*, **12**(4):877, mar 2022. doi:10.3390/diagnostics12040877.

[93] V. Corona, A. Aviles-Rivero, N. Debroux, C. Le Guyader, and C.-B. Schönlieb. **Variational multi-task MRI reconstruction: Joint reconstruction, registration and super-resolution**. *Medical Image Analysis*, **68**(August):101941, feb 2021. doi:10.1016/j.media.2020.101941.

[94] W. Bano, G. F. Piredda, M. Davies, I. Marshall, M. Golbabaee, R. Meuli, T. Kober, J. Thiran, and T. Hilbert. **Model-based super-resolution reconstruction of T 2 maps**. *Magnetic Resonance in Medicine*, **83**(3):906–919, mar 2020. doi:10.1002/mrm.27981.

[95] N. Basty and V. Grau. **Super Resolution of Cardiac Cine MRI Sequences Using Deep Learning**. In *Lecture Notes in Computer Science (including subseries Lecture Notes in Artificial Intelligence and Lecture Notes in Bioinformatics)*, **11040 LNCS**, pages 23–31. Springer International Publishing, 2018. doi:10.1007/978-3-030-00946-5_3.

[96] K. K. Bhatia, A. N. Price, W. Shi, J. V. Hajnal, and D. Rueckert. **Super-resolution reconstruction of cardiac MRI using coupled dictionary learning**. In *2014 IEEE 11th International Symposium on Biomedical Imaging (ISBI)*, pages 947–950. IEEE, apr 2014. doi:10.1109/ISBI.2014.6868028.

[97] W. Shi, J. Caballero, C. Ledig, X. Zhuang, W. Bai, K. Bhatia, A. M. S. M. de Marvao, T. Dawes, D. O'Regan, and D. Rueckert. **Cardiac Image Super-Resolution with Global Correspondence Using Multi-Atlas PatchMatch**. In *Lecture Notes in Computer Science (including subseries Lecture Notes in Artificial Intelligence and Lecture Notes in Bioinformatics)*, **8151**, pages 9–16. 2013. doi:10.1007/978-3-642-40760-4_2.

[98] Y. Xia, N. Ravikumar, J. P. Greenwood, S. Neubauer, S. E. Petersen, and A. F. Frangi. **Super-Resolution of Cardiac MR Cine Imaging using Conditional GANs and Unsupervised Transfer Learning**. *Medical Image Analysis*, **71**:102037, jul 2021. doi:10.1016/j.media.2021.102037.

[99] B. D. de Senneville, C. R. Cardiet, A. J. Trotier, E. J. Ribot, L. Lafitte, L. Facq, and S. Miraux. **Optimizing 4D abdominal MRI: image denoising using an iterative back-projection approach**. *Physics in Medicine & Biology*, **65**(1):015003, jan 2020. doi:10.1088/1361-6560/ab563e.

[100] S. McDonagh, B. Hou, A. Alansary, O. Oktay, K. Kamnitsas, M. Rutherford, J. V. Hajnal, and B. Kainz. **Context-Sensitive Super-Resolution for Fast Fetal Magnetic Resonance Imaging**. In *Lecture Notes in Computer Science (including subseries Lecture Notes in Artificial Intelligence and Lecture Notes in Bioinformatics)*, **10555 LNCS**, pages 116–126. feb 2017. doi:10.1007/978-3-319-67564-0_12.

[101] M. Nicastro, B. Jeurissen, Q. Beirinckx, C. Smekens, D. H. J. Poot, J. Sijbers, and A. J. den Dekker. **To shift or to rotate? Comparison of acquisition strategies for multi-slice super-resolution magnetic resonance imaging**. *Frontiers in Neuroscience*, **16**, nov 2022. doi:10.3389/fnins.2022.1044510.

[102] B. Scherrer, A. Gholipour, and S. K. Warfield. **Super-resolution reconstruction to increase the spatial resolution of diffusion weighted images from orthogonal anisotropic acquisitions**. *Medical Image Analysis*, **16**(7):1465–1476, oct 2012. doi:10.1016/j.media.2012.05.003.

[103] Shuzhou Jiang, Hui Xue, A. Glover, M. Rutherford, and J. Hajnal. **A Novel Approach to Accurate 3D High Resolution and High SNR Fetal Brain Imaging**. In *3rd IEEE International Symposium on Biomedical Imaging: Macro to Nano, 2006.*, **2006**, pages 662–665. IEEE, 2006. doi:10.1109/ISBI.2006.1625003.

[104] K. T. Block, M. Uecker, and J. Frahm. **Undersampled radial MRI with multiple coils. Iterative image reconstruction using a total variation constraint**. *Magnetic Resonance in Medicine*, **57**(6):1086–1098, jun 2007. doi:10.1002/mrm.21236.

[105] D. Rueckert, L. Sonoda, C. Hayes, D. Hill, M. Leach, and D. Hawkes. **Nonrigid registration using free-form deformations: application to breast MR images**. *IEEE Transactions on Medical Imaging*, **18**(8):712–721, 1999. doi:10.1109/42.796284.

[106] W. P. Segars, G. Sturgeon, S. Mendonca, J. Grimes, and B. M. W. Tsui. **4D XCAT phantom for multimodality imaging research**. *Medical Physics*, **37**(9):4902–4915, aug 2010. doi:10.1118/1.3480985.

[107] G. A. Keith, C. T. Rodgers, M. A. Chappell, and M. D. Robson. **A look-locker acquisition scheme for quantitative myocardial perfusion imaging with FAIR arterial spin labeling in humans at 3 tesla**. *Magnetic Resonance in Medicine*, **78**(2):541–549, aug 2017. doi:10.1002/mrm.26388.

[108] G. Captur, P. Gatehouse, K. E. Keenan, F. G. Heslinga, R. Bruehl, M. Prothmann, M. J. Graves, R. J. Eames, C. Torlasco, G. Benedetti, J. Donovan, B. Ittermann, R. Boubertakh, A. Bathgate, C. Royet, W. Pang, R. Nezafat, M. Salerno, P. Kellman, and J. C. Moon. **A medical device-grade T1 and ECV phantom for global T1 mapping quality assurance—the T1 Mapping and ECV Standardization in cardiovascular magnetic resonance (T1MES) program**. *Journal of Cardiovascular Magnetic Resonance*, **18**(1):58, dec 2016. doi:10.1186/s12968-016-0280-z.

[109] J. Jackson, C. Meyer, D. Nishimura, and A. Macovski. **Selection of a convolution function for Fourier inversion using gridding (computerised tomography application)**. *IEEE Transactions on Medical Imaging*, **10**(3):473–478, 1991. doi:10.1109/42.97598.

[110] J. Keiner, S. Kunis, and D. Potts. **Using NFFT 3—A Software Library for Various Nonequispaced Fast Fourier Transforms**. *ACM Transactions on Mathematical Software*, **36**(4):1–30, aug 2009. doi:10.1145/1555386.1555388.

[111] A. Boussuges, J. Finance, G. Chaumet, and F. Brégeon. **Diaphragmatic motion recorded by M-mode ultrasonography: limits of normality**. *ERJ Open Research*, **7**(1):00714–2020, jan 2021. doi:10.1183/23120541.00714-2020.

[112] D. H. J. Poot, V. Van Meir, and J. Sijbers. **General and Efficient Super-Resolution Method for Multi-slice MRI**. In *Lecture Notes in Computer Science (including subseries Lecture Notes in Artificial Intelligence and Lecture Notes in Bioinformatics)*, **6361 LNCS**, pages 615–622. 2010. doi:10.1007/978-3-642-15705-9_75.

[113] D. C. Thomas, A. Oros-Peusquens, D. Poot, and N. J. Shah. **Whole-Brain Water Content Mapping Using Super-Resolution Reconstruction with MRI Acquisition in 3 Orthogonal Orientations**. *Magnetic Resonance in Medicine*, **88**(5):2117–2130, nov 2022. doi:10.1002/mrm.29377.

[114] Shuzhou Jiang, Hui Xue, A. Glover, M. Rutherford, D. Rueckert, and J. Hajnal. **MRI of Moving Subjects Using Multislice Snapshot Images With Volume Reconstruction (SVR): Application to Fetal, Neonatal, and Adult Brain Studies**. *IEEE Transactions on Medical Imaging*, **26**(7):967–980, jul 2007. doi:10.1109/TMI.2007.895456.

[115] R. Shilling, T. Robbie, T. Bailloeul, K. Mewes, R. Mersereau, and M. Brummer. **A Super-Resolution Framework for 3-D High-Resolution and High-Contrast Imaging Using 2-D Multislice MRI**. *IEEE Transactions on Medical Imaging*, **28**(5):633–644, may 2009. doi:10.1109/TMI.2008.2007348.

[116] Y. Wang, J. Yang, W. Yin, and Y. Zhang. **A New Alternating Minimization Algorithm for Total Variation Image Reconstruction**. *SIAM Journal on Imaging Sciences*, **1**(3):248–272, jan 2008. doi:10.1137/080724265.

[117] A. Chambolle. **An Algorithm for Total Variation Minimization and Applications**. *Journal of Mathematical Imaging and Vision*, **20**(1/2):89–97, jan 2004. doi:10.1023/B:JMIV.0000011325.36760.1e.

[118] D. C. Liu and J. Nocedal. **On the limited memory BFGS method for large scale optimization**. *Mathematical Programming*, **45**(1-3):503–528, aug 1989. doi:10.1007/BF01589116.

[119] A. Rund, C. S. Aigner, K. Kunisch, and R. Stollberger. **Simultaneous multislice refocusing via time optimal control**. *Magnetic Resonance in Medicine*, **80**(4):1416–1428, oct 2018. doi:10.1002/mrm.27124.

[120] J. Pauly, P. Le Roux, D. Nishimura, and A. Macovski. **Parameter relations for the Shinnar-Le Roux selective excitation pulse design algorithm (NMR imaging)**. *IEEE Transactions on Medical Imaging*, **10**(1):53–65, mar 1991. doi:10.1109/42.75611.

[121] D. Padfield. **Masked Object Registration in the Fourier Domain**. *IEEE Transactions on Image Processing*, **21**(5):2706–2718, may 2012. doi:10.1109/TIP.2011.2181402.

[122] A. D. Scott, J. Keegan, and D. N. Firmin. **Motion in Cardiovascular MR Imaging**. *Radiology*, **250**(2):331–351, feb 2009. doi:10.1148/radiol.2502071998.

[123] M. D. Cerqueira, N. J. Weissman, V. Dilsizian, A. K. Jacobs, S. Kaul, W. K. Laskey, D. J. Pennell, J. A. Rumberger, T. Ryan, and M. S. Verani. **Standardized Myocardial Segmentation and Nomenclature for Tomographic Imaging of the Heart**. *Circulation*, **105**(4):539–542, jan 2002. doi:10.1161/hc0402.102975.

[124] A. Etienne, R. M. Botnar, A. M. van Muiswinkel, P. Boesiger, W. J. Manning, and M. Stuber. **?Soap-Bubble? visualization and quantitative analysis of 3D coronary magnetic resonance angiograms**. *Magnetic Resonance in Medicine*, **48**(4):658–666, oct 2002. doi:10.1002/mrm.10253.

[125] F. von Knobelsdorff-Brenkenhoff, M. Prothmann, M. A. Dieringer, R. Wassmuth, A. Greiser, C. Schwenke, T. Niendorf, and J. Schulz-Menger. **Myocardial T1 and T2 mapping at 3 T: reference values, influencing factors and implications**. *Journal of Cardiovascular Magnetic Resonance*, **15**(1):53, dec 2013. doi:10.1186/1532-429X-15-53.

[126] L. Huang, R. Neji, M. S. Nazir, J. Whitaker, P. Duong, F. Reid, F. Bosio, A. Chiribiri, R. Razavi, and S. Roujol. **FASt single-breathhold 2D multislice myocardial T 1 mapping (FAST1) at 1.5T for full left ventricular coverage in three breathholds**. *Journal of Magnetic Resonance Imaging*, **51**(2):492–504, feb 2020. doi:10.1002/jmri.26869.

[127] D. C. Bloomgarden, Z. a. Fayad, V. a. Ferrari, B. Chin, M. G. St. John Sutton, and L. Axel. **Global cardiac function using fast breath-hold MRI: Validation of new acquisition and analysis techniques**. *Magnetic Resonance in Medicine*, **37**(5):683–692, may 1997. doi:10.1002/mrm.1910370510.

[128] Y. Wang, K. Moin, S. T. Mathew, O. Akinboboye, and N. Reichek. **Myocardial first-pass perfusion assessment using rotational long-axis MRI**. *Journal of Magnetic Resonance Imaging*, **22**(1):53–58, jul 2005. doi:10.1002/jmri.20351.

[129] M. Tanaka, T. Sakamoto, S. Sugawara, H. Nakajima, Y. Katahira, S. Ohtsuki, and H. Kanai. **Blood flow structure and dynamics, and ejection mechanism in the left ventricle: Analysis using echo-dynamography**. *Journal of Cardiology*, **52**(2):86–101, oct 2008. doi:10.1016/j.jjcc.2008.05.005.

[130] P. Garg, S. Crandon, P. P. Swoboda, G. J. Fent, J. R. J. Foley, P. G. Chew, L. A. E. Brown, S. Vijayan, M. E. C. J. Hassell, R. Nijveldt, M. Bissell, M. S. M. Elbaz, A. Al-Mohammad, J. J. M. Westenberg, J. P. Greenwood, R. J. van der Geest, S. Plein, and E. Dall'Armellina. **Left ventricular blood flow kinetic energy after myocardial infarction - insights from 4D flow cardiovascular magnetic resonance**. *Journal of Cardiovascular Magnetic Resonance*, **20**(1):61, dec 2018. doi:10.1186/s12968-018-0483-6.

[131] R. M. Lang, L. P. Badano, V. Mor-Avi, J. Afilalo, A. Armstrong, L. Ernande, F. A. Flachskampf, E. Foster, S. A. Goldstein, T. Kuznetsova, P. Lancellotti, D. Muraru, M. H. Picard, E. R. Rietzschel, L. Rudski, K. T. Spencer, W. Tsang, and J.-U. Voigt. **Recommendations for Cardiac Chamber Quantification by Echocardiography in Adults: An Update from the American Society of Echocardiography and the European Association of Cardiovascular Imaging**. *Journal of the American Society of Echocardiography*, **28**(1):1–39.e14, jan 2015. doi:10.1016/j.echo.2014.10.003.

[132] P. F. Ferreira, P. D. Gatehouse, R. H. Mohiaddin, and D. N. Firmin. **Cardiovascular magnetic resonance artefacts**. *Journal of Cardiovascular Magnetic Resonance*, **15**(1):41, dec 2013. doi:10.1186/1532-429X-15-41.

[133] S. Pfaffenberger, P. Bartko, A. Graf, E. Pernicka, J. Babayev, E. Lolic, D. Bonderman, H. Baumgartner, G. Maurer, and J. Mascherbauer. **Size Matters! Impact of Age, Sex, Height, and Weight on the Normal Heart Size**. *Circulation: Cardiovascular Imaging*, **6**(6):1073–1079, nov 2013. doi:10.1161/CIRCIMAGING.113.000690.

[134] J. Caballero, A. N. Price, D. Rueckert, and J. V. Hajnal. **Dictionary Learning and Time Sparsity for Dynamic MR Data Reconstruction**. *IEEE Transactions on Medical Imaging*, **33**(4):979–994, apr 2014. doi:10.1109/TMI.2014.2301271.

[135] W. Shi, H. Xu, C. Sun, J. Sun, Y. Li, X. Xu, T. Zheng, Y. Zhang, G. Wang, and D. Wu. **AFFIRM: Affinity Fusion-Based Framework for Iteratively Random Motion Correction of Multi-Slice Fetal Brain MRI**. *IEEE Transactions on Medical Imaging*, **42**(1):209–219, jan 2023. doi:10.1109/TMI.2022.3208277.

[136] K. Berggren, D. Ryd, E. Heiberg, A. H. Aletras, and E. Hedström. **Super-Resolution Cine Image Enhancement for Fetal Cardiac Magnetic Resonance Imaging**. *Journal of Magnetic Resonance Imaging*, **56**(1):223–231, jul 2022. doi:10.1002/jmri.27956.

[137] E. M. Masutani, N. Bahrami, and A. Hsiao. **Deep Learning Single-Frame and Multiframe Super-Resolution for Cardiac MRI**. *Radiology*, **295**(3):552–561, jun 2020. doi:10.1148/radiol.2020192173.

[138] D. Qiu, Y. Cheng, and X. Wang. **Progressive Feedback Residual Attention Network for Cardiac Magnetic Resonance Imaging Super-Resolution**. *IEEE Journal of Biomedical and Health Informatics*, **27**(7):3478–3488, jul 2023. doi:10.1109/JBHI.2023.3272155.

[139] R. R. Upendra, R. Simon, and C. A. Linte. **A Deep Learning Framework for Image Super-Resolution for Late Gadolinium Enhanced Cardiac MRI**. In *2021 Computing in Cardiology (CinC)*, number April, pages 1–4. IEEE, sep 2021. doi:10.23919/CinC53138.2021.9662790.

[140] H. K. Aggarwal, M. P. Mani, and M. Jacob. **MoDL: Model-Based Deep Learning Architecture for Inverse Problems**. *IEEE Transactions on Medical Imaging*, **38**(2):394–405, feb 2019. doi:10.1109/TMI.2018.2865356.

[141] J. I. Hamilton, Y. Jiang, D. Ma, Y. Chen, W. Lo, M. Griswold, and N. Seiberlich. **Simultaneous multislice cardiac magnetic resonance fingerprinting using low rank reconstruction**. *NMR in Biomedicine*, **32**(2):139–148, feb 2019. doi:10.1002/nbm.4041.

[142] C. S. Aigner and S. Schmitter. **Designing B0 robust adiabatic multi-band inversion pulses with high time-bandwidth products and smooth slice selective gradients**. In *Proceedings of the 28th Annual Meeting of ISMRM*, page 3692, 2020.

[143] D. Ma, V. Gulani, N. Seiberlich, K. Liu, J. L. Sunshine, J. L. Duerk, and M. A. Griswold. **Magnetic resonance fingerprinting**. *Nature*, **495**(7440):187–192, 2013. doi:10.1038/nature11971.

[144] A. T. O'Brien, K. E. Gil, J. Varghese, O. P. Simonetti, and K. M. Zareba. **T2 mapping in myocardial disease: a comprehensive review**. *Journal of Cardiovascular Magnetic Resonance*, **24**(1):33, dec 2022. doi:10.1186/s12968-022-00866-0.

[145] A. Bustin, A. Hua, G. Milotta, O. Jaubert, R. Hajhosseiny, T. F. Ismail, R. M. Botnar, and C. Prieto. **High-spatial-resolution 3D whole-heart MRI T2 mapping for assessment of myocarditis**. *Radiology*, **298**(3):578–586, 2021. doi:10.1148/radiol.2021201630.

[146] S. Giri, Y.-C. Chung, A. Merchant, G. Mihai, S. Rajagopalan, S. V. Raman, and O. P. Simonetti. **T2 quantification for improved detection of myocardial edema**. *Journal of Cardiovascular Magnetic Resonance*, **11**(1):56, dec 2009. doi:10.1186/1532-429X-11-56.

[147] R. B. van Heeswijk, D. Piccini, H. Feliciano, R. Hullin, J. Schwitter, and M. Stuber. **Self-navigated isotropic three-dimensional cardiac T 2 mapping**. *Magnetic Resonance in Medicine*, **73**(4):1549–1554, apr 2015. doi:10.1002/mrm.25258.

[148] M. Markl, R. Rustogi, M. Galizia, A. Goyal, J. Collins, A. Usman, B. Jung, D. Foell, and J. Carr. **Myocardial T2-mapping and velocity mapping: Changes in regional left ventricular structure and function after heart transplantation**. *Magnetic Resonance in Medicine*, **70**(2):517–526, aug 2013. doi:10.1002/mrm.24472.

[149] P. Thavendiranathan, M. Walls, S. Giri, D. Verhaert, S. Rajagopalan, S. Moore, O. P. Simonetti, and S. V. Raman. **Improved Detection of Myocardial Involvement in Acute Inflammatory Cardiomyopathies Using T2 Mapping**. *Circulation: Cardiovascular Imaging*, **5**(1):102–110, jan 2012. doi:10.1161/CIRCIMAGING.111.967836.